A View Screen beam profile monitor for the ARIEL e-linac at TRIUMF

by

Douglas Wesley Storey
B.Sc., University of Winnipeg, 2007
B.A.E.M., University of Minnesota, 2009

A Thesis Submitted in Partial Fulfillment of the
Requirements for the Degree of

MASTER OF SCIENCE

in the Department of Physics and Astronomy

University of Victoria

A View Screen beam profile monitor for the ARIEL e-linac at TRIUMF

by

Douglas Wesley Storey
B.Sc., University of Winnipeg, 2007
B.A.E.M., University of Minnesota, 2009

Supervisory Committee

Dr. D. Karlen, Supervisor
(University of Victoria)

Dr. R. Keeler, Departmental Member
(University of Victoria)

Supervisory Committee

Dr. D. Karlen, Supervisor
(University of Victoria)

Dr. R. Keeler, Departmental Member
(University of Victoria)

ABSTRACT

A megawatt class electron linear accelerator (e-linac) will be constructed at TRIUMF as part of the new ARIEL facility which will produce rare ion beams for the study of nuclear structure and astrophysics, and material science. The 50 MeV, 10 mA, continuous wave e-linac will drive gamma ray induced fissioning of a Uranium target for the production of neutron rich beam species. View Screens located at a number of places along the e-linac beam-line will acquire two dimensional images of the transverse electron beam profiles, providing measurements of the size, position, and shape of the incident e-linac beam.

The design of the View Screens will be presented, based on design studies and simulations performed to evaluate the performance of the View Screens under various operating conditions. These studies include GEANT simulations of the energy loss and scattering of the electron beam as it passes through the scintillation and Optical Transition Radiation beam targets, the subsequent thermal response of the targets, and a ray tracing optics simulation to optimize the configuration of the imaging optics. Bench test have been performed on the resulting optics design to evaluate the imaging characteristics, verifying fulfillment of the design requirements.

Construction of a prototype View Screen device is currently underway, with beam tests scheduled for Fall 2011. A total of 14 View Screens will be constructed and installed along the e-linac beam-line.

Contents

Supervisory Committee **ii**

Abstract **iii**

Table of Contents **iv**

List of Tables **vi**

List of Figures **vii**

Acknowledgements **ix**

Dedication **x**

1 Introduction **1**
- 1.1 ARIEL and the TRIUMF Electron Linac 1
- 1.2 Electron Beam Diagnostics 8
- 1.3 Requirements of the View Screens 13
- 1.4 Focus of This Work 15

2 View Screen Beam Targets **16**
- 2.1 Scintillation Targets 16
- 2.2 Optical Transition Radiation 19

3 Design of the View Screens **24**
- 3.1 Elements of the View Screen 26
  - 3.1.1 Targets 26
  - 3.1.2 Target Holder and Actuator 28
  - 3.1.3 Imaging Optics 31
  - 3.1.4 Optics Layout 37

3.1.5 Calibration Light Source 37
3.1.6 Support Structure and Shielding 39

4 Image Correction and Calibration **42**
4.1 Radiation Damage Calibration 42
4.2 Geometric Calibration 43
4.3 Thermal Correction 44
4.4 Light Collection Efficiency Calibration 45
4.5 Summary of the Image Processing Procedures 49

5 Simulation Studies **51**
5.1 GEANT Simulations of the Beam Targets 51
5.2 Thermal Simulations of the Beam Targets 57
5.3 Simulation of the Imaging Optics 65
5.4 Modes of Operation 68

6 Optics Bench Tests **71**
6.1 Test Bench Setup 71
6.2 Optics Resolution 73
6.3 Chromox Scintillation Tests 77

7 Conclusions **80**

Bibliography **82**

A Additional Information **86**
A.1 GEANT Simulations of Additional Candidate Materials 86
A.2 Thermal Simulations of Additional Candidate Materials 89

List of Tables

Table 1.1 Design parameters of the e-linac 4
Table 1.2 Summary of the nominal beam sizes and corresponding requirements on the View Screens 13

Table 2.1 OTR foil material properties 23

Table 3.1 The types of optical glass within the achromatic lenses 34
Table 3.2 AVT Manta G-046 camera specifications 35
Table 3.3 Positioning of the lenses and camera 37

Table 5.1 Energy losses per electron through various beam targets 54
Table 5.2 Maximum currents for 2 W of total energy losses 57
Table 5.3 The thermal properties of YAG:Ce and LYSO:Ce at 300 K . . . 60

List of Figures

Figure 1.1 Schematic diagram of the photo-fission process 2
Figure 1.2 The isotope production distribution for photo-fission and proton beam target stations 3
Figure 1.3 Schematic diagram of the e-linac 6
Figure 1.4 Schematic diagram of the EHBT and target stations 7

Figure 2.1 Broadening of beam profile through 45° YAG:Ce screen 18
Figure 2.2 Backward and Forward OTR emission from a foil 20
Figure 2.3 Geometric variables of the OTR emission distribution 21
Figure 2.4 OTR emission of 10 MeV electrons on Pyrolytic Graphite . . . 22

Figure 3.1 The View Screen device mounted on the ELBT diagnostics cross 25
Figure 3.2 Calibration target layouts 28
Figure 3.3 The EMBT / EHBT target holder 29
Figure 3.4 The layout of the imaging optics 32
Figure 3.5 Schleimflug angle 38
Figure 3.6 Mounting of the ELBT camera box 40

Figure 4.1 The temperature dependence of the light yield of YAG:Ce . . . 45
Figure 4.2 The light collection efficiency for scintillation targets 47
Figure 4.3 The light collection efficiency for OTR targets 47
Figure 4.4 The errors incurred with the target mounting angle offset . . . 48
Figure 4.5 Steps of the image post processing procedures 50

Figure 5.1 Total energy loss through a YAG:Ce screen 53
Figure 5.2 Energy loss distribution through beam targets 55
Figure 5.3 Scattering distribution through beam targets 56
Figure 5.4 The thermal properties of Pyroid as a function of temperature . 60
Figure 5.5 Thermal response to a pulsed beam structure 62
Figure 5.6 Maximum ELBT target temperatures 63

Figure 5.7 Maximum EMBT/EHBT target temperatures 64
Figure 5.8 The setup of the optics ray-tracing simulation geometry 66
Figure 5.9 Cross section of the simulated and measured PSFs 67
Figure 5.10 Quantum efficiency of the Manta G-046 CCD sensor 69
Figure 5.11 Operating ranges of OTR and YAG:Ce beam targets 70

Figure 6.1 The optical bench test setup 71
Figure 6.2 Resolution test target 72
Figure 6.3 The PSF measured with ELBT optics 74
Figure 6.4 The PSF measured with EMBT/EHBT optics 74
Figure 6.5 Contrast Transfer Function 75
Figure 6.6 Effect of mounting the camera at an angle 76
Figure 6.7 Chromox scintillation decay 78
Figure 6.8 UV laser beam profile on a Chromox screen 79

Figure A.1 Energy loss distribution through beam targets 87
Figure A.2 Scattering distribution through beam targets 88
Figure A.3 Maximum ELBT target temperatures for 200 μm YAG:Ce . . . 89
Figure A.4 Maximum ELBT target temperatures 91
Figure A.5 Maximum EMBT/EHBT scintillation target temperatures . . . 92
Figure A.6 Maximum EMBT/EHBT OTR target temperatures 93

ACKNOWLEDGEMENTS

I would like to thank my supervisor Dr. Dean Karlen for his guidance and support throughout the research and writing process. I am also grateful to Paul Birney, with whom I have spent numerous hours working in the lab, and to the rest of the University of Victoria's e-linac research group.

I would like to acknowledge NSERC and the University of Victoria's Department of Physics and Astronomy for allowing me to persue this endeavor, and TRIUMF for the amazing opportunity to work in the exciting field of Accelerator Physics.

And finally, thank you to my family and to Carly Sable for all of their support and encouragement over the years. I couldn't have done it without you!

DEDICATION

For my wonderful girlfriend, Carly

Chapter 1

Introduction

1.1 ARIEL and the TRIUMF Electron Linac

As part of TRIUMF's Five Year Plan, 2010-2015 [1], a new facility will be constructed to produce short lived isotopes for physics and medicine research. ARIEL, the Advanced Rare IsotopE Laboratory, will expand on TRIUMF's ISAC facility which currently produces Rare Ion Beams (RIBs), primarily for the study of nuclear structure and nuclear astrophysics.

ARIEL will build on TRIUMF's current program by increasing the number of simultaneous RIBs from its current capability of delivering beam to a single user at a time, to up to three users simultaneously. The total number of hours of delivered beam per year will be increased through the use of a new beam target station capable of higher production rates, and through the use of two different beam sources on independent schedules – a new beam-line from the TRIUMF 500 MeV proton cyclotron and a new 0.5 MW electron linear accelerator (e-linac).

The ARIEL program has been broken into several main projects: the 50 MeV, 0.5 MW e-linac to act as photo-fission driver, a new target hall and target stations, a new proton beam line from the 500 MeV cyclotron to the target station, and the RIB front end, including ionizer, mass separators, and eventually the addition of new RIB accelerators.

The design and construction of the high average current, continuous wave (CW) e-linac for driving gamma ray induced fissioning, or photo-fissioning, of a Uranium-238 target is the centerpiece of the ARIEL project. The e-linac will make use of TRIUMF's valuable existing infrastructure including a shielded hall with services for installation of the e-linac (previously the Proton Hall) and the world class RIB experimental stations in the ISAC facility. The program will also expand on TRIUMF's in house superconducting RF expertise.

The design of the e-linac's accelerating modules will make use of the 1.3 GHz superconducting radio-frequency (SCRF) technology developed for the TESLA, XFEL, and the International Linear Collider (ILC) projects and will benefit from the extensive research performed for these projects [2]. Furthermore, development in this area will prepare Canada and TRIUMF's local commercial partner PAVAC for upcoming SCRF projects world wide such as the ILC or CERN-SPL [3, 4].

An e-linac driven photo-fission source will make available new neutron rich beam species which will allow the ARIEL facility to open new areas of research and collaboration to TRIUMF's experimental program including material science through β-NMR studies and the production and study of medical isotopes. The e-linac is being designed to allow for a future reconfiguration of the e-linac for a linac based photon light source, a so called fourth generation light source, such as a Compton scatter source, Free Electron Laser, or Coherent Synchrotron Radiation.

The process of photo-fissioning of Uranium-238 was proposed in 1999 by W. T. Diamond as a alternative approach to producing rare isotope beams [5]. In this process, a high power electron beam is used to produce high energy Bremsstrahlung photons, which in turn induce the fission of Uranium-238 in a Uranium Carbide target. This process can can be optimized to yield high amounts of neutron-rich nuclei that can be ionized and accelerated to produce a RIB. A schematic diagram of the production of a RIB through the process of photo-fission is shown in Figure 1.1.

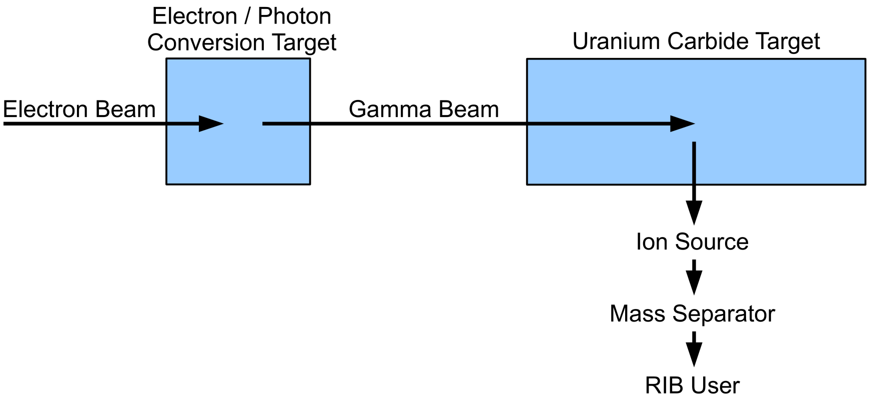

Figure 1.1: A schematic diagram showing the steps in the production of RIBs through the process of e-linac driven photo-fission.

Figure 1.2 shows the distribution of isotopes produced through the processes of e-linac driven photo-fission and proton irradiation of a Uranium target for the production of RIBs [6]. The products of photo-fission primarily lie within a small group of neutron rich nuclei while proton irradiation leads to the production of a much larger range of nuclei – both proton and neutron rich. Although photo-fission results in a smaller range of nuclei than a proton driver, it produces relatively high amounts of a few beam species with fewer isobaric contaminates, allowing for the production of cleaner beams. This also leads to lower activation within the target station and therefore easier remote handling.

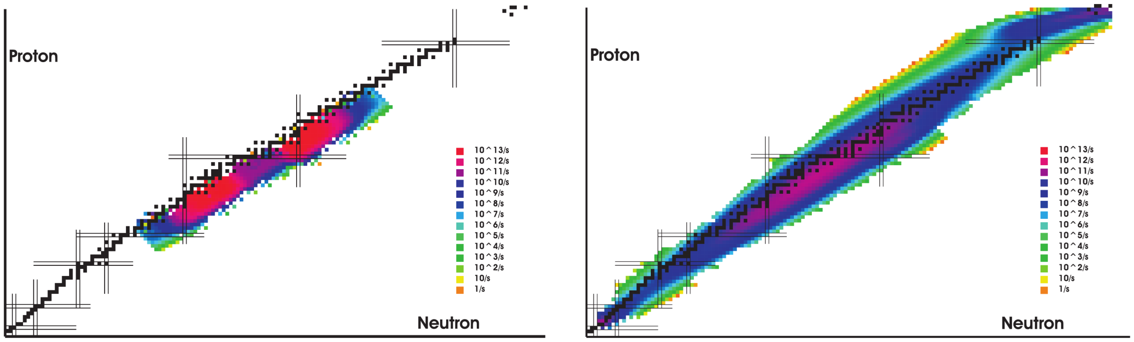

(a) 50 MeV, 10mA e-linac driven photo-fission of Uranium-238

(b) 500 MeV, 10 μA proton irradiation of Uranium-238

Figure 1.2: The isotope production distributions for e-linac and proton driven target stations [6].

A 50 MeV, 10 mA electron beam impinging upon a Tungsten converter target is expected to produce up to 5×10^{13} fissions per second in a Uranium-238 target. The photo-fission target will be complemented by a new 500 MeV proton beam-line from the cyclotron providing production of other isotopes of interest. Development of a both photo-fission and proton driven target stations for the ARIEL facility makes use of the advantages of both sources for RIBs.

The key specifications of the e-linac are summarized in Table 1.1. To optimize fission rates, an e-linac beam energy of 50 MeV, a maximum current of 10 mA, and Continous Wave operation have been selected. The rate of photo-fission increases with energy up to about 50 MeV, after which significant gains in production rate would require large increases in beam energy. Therefore, to reach the goal of 10^{13} fissions per second, a high beam current of 10 mA is required, rather than increasing the beam energy further.

Continuous Wave (CW) accelerators accelerate particles within each RF wave within the accelerating modules, a duty factor of 100%, rather than in brief pulses of high instantaneous current. Although CW operation introduces design challenges associated with significantly higher heat loads in the RF components, it is required to limit thermal shocking within the Uranium Carbide targets [7]. Additionally, CW operation limits periodic beam-load detuning and transient effects of a pulsed beam.

Final Beam Energy	50 MeV
Beam Current	10 mA
Beam Power at Target Station	500 kW
Bunch Charge	16 pC
Bunch Repetition Rate	650 MHz
Accelerating Frequency	1.3 GHz
Duty Factor	100% (CW)

Table 1.1: Design parameters of the e-linac.

Electrons for the e-linac are emitted from a 300 keV thermionic electron gun operating at 650 MHz. Electrons are bunched soon after the gun within a normal conducting buncher cavity, resulting in bunches containing 16 pC of charge, or approximately 10^8 electrons. Bunching of the beam into short bunches of electrons is required to insure efficient acceleration within the subsequent RF cavities. Lowering of the average beam intensity may be achieved either through decreasing the amount of charge contained within each bunch, or by decreasing the beam duty factor while maintaining the bunch peak current.

The electrons undergo acceleration in the injector cryogenic module, or Electron INJector (EINJ), which provides 5 to 10 MeV of acceleration to up to 10 mA of beam current. The beam-line from the 300 keV electron gun to the EINJ is called the Electron Low energy Beam Transport (ELBT). The major components in the ELBT beam-line are the buncher cavity, solenoid magnets for beam focusing, and a suite of beam diagnostics devices.

The Medium energy Beam Transport line (EMBT) carries the electrons from the injector to the first of two Electron Accelerating Cryogenic modules (EACA and EACB) for acceleration up to 50 MeV. Each accelerating module contains two nine-cell SCRF cavities which are one meter in length and provide up to 10 MeV of acceleration.

After acceleration through the accelerating modules, a high energy transport line, the EHBT, carries the electrons from the main linac to the target station. The transport line is composed of steering and focusing magnets as well as additional diagnostics devices. Beam dumps are included along the beam-line to dispose of electron beams during commissioning and diagnostics runs. A schematic layout of the entire e-linac is shown in Figures 1.3 and 1.4. The future proton line from the 500 MeV cyclotron is also shown on the top corner of Figure 1.3 and will share the beam tunnel to the target stations and front end, which is shown in Figure 1.4.

The division of the e-linac into separate injector and main linac sections allows for possible reconfiguration of the e-linac to either an Energy Recovery Linac (ERL) at 80 MeV and 20 mA, or a Recirculating Linear Accelerator (RLA) with beam intensity of 160 MeV and 2 mA [8]. This could be achieved through the retrofitting of several components of the e-linac and the construction of return arcs immediately following the final accelerating module to make a ring, as shown in Figure 1.3.

A reconfigured e-linac could provide ~ 100 MeV electrons for a Compton scatter source, based on the scattering of photons from a pulsed table-top laser off of the relativistic electron beam to produce hard x-rays for research, industrial, or medical applications. Alternatively, the e-linac could be used to produce infrared radiation as a Free Electron Laser or Coherent Synchrotron Source. Infrared radiation may be used for research in the physical sciences, biology, and medicine [8].

Due to the converging goals of TRIUMF's ARIEL project and India's Variable Energy Cyclotron Center (VECC) to each build electron accelerators to drive photo-fission for neutron-rich RIB production, a collaboration has been formed to design, build, and test the 5-10 MeV super conducting electron injector. While TRIUMF plans to follow the injector line with two accelerating cryomodules taking the beam energy to 50 MeV, VECC is currently planning to use a single accelerating cryomodule to accelerate to a 30 MeV, 100 kW beam to achieve in-target fission rates of $\sim 10^{13}$ fissions per second [9].

Two electron injector units will be constructed with injector beam tests completing at TRIUMF in 2012, after which one injector will be shipped to VECC. An electron gun, buncher, and low energy beam line will be constructed separately in India for the VECC program.

The schedule for the ARIEL facility was first laid out in TRIUMF's Five Year Plan 2010-2015 [1] with funding for the project secured in June 2010. Upon completion of injector tests in 2012, the first accelerating cryomodule will be installed and tested allowing for 25 MeV 4 mA beams at 100 kW by 2015. As of 2017, with both EACA and EACB installed, the power level will reach 400 kW with a 40 MeV beam at 10 mA. [6].

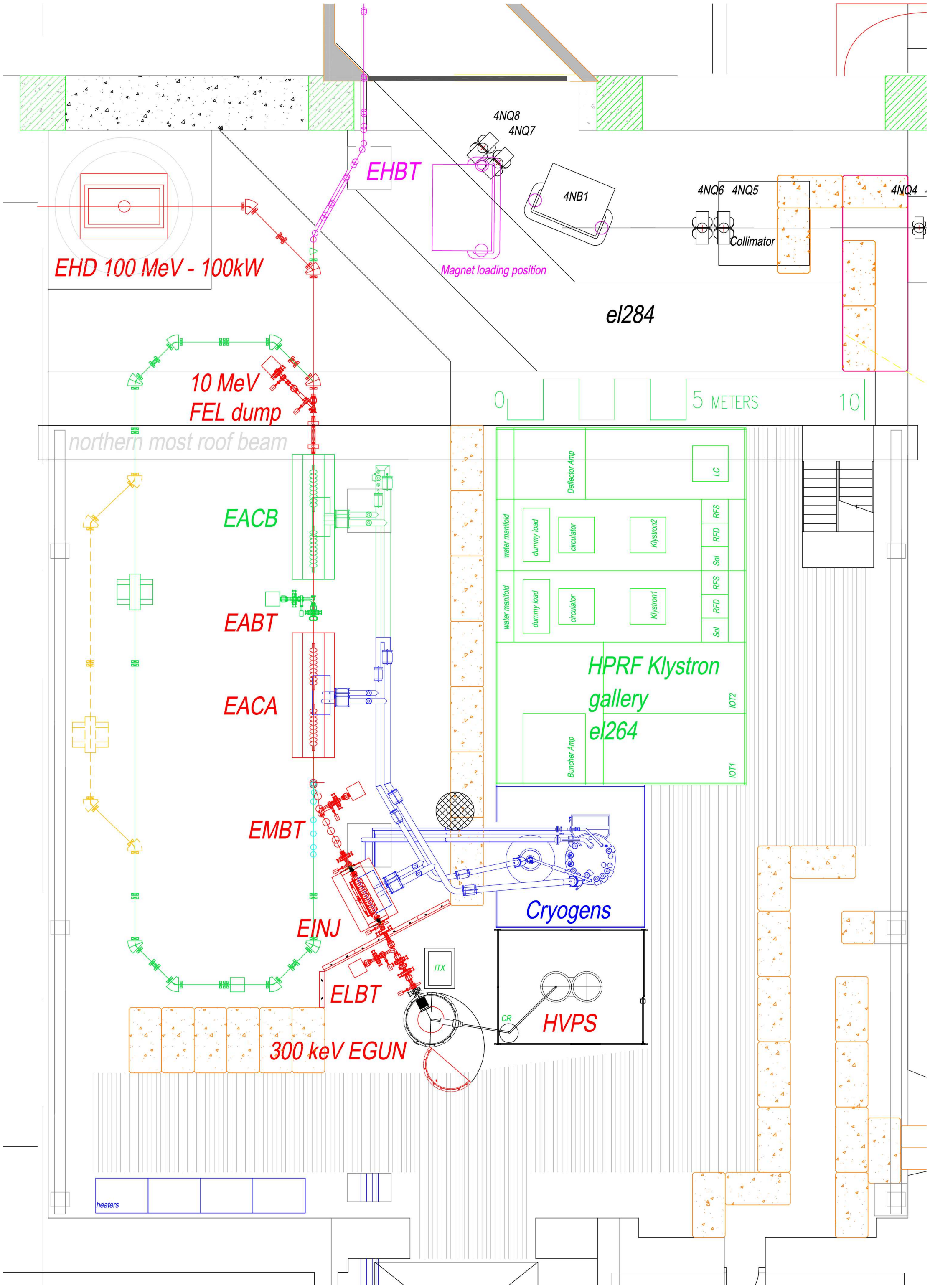

Figure 1.3: Schematic diagram of the layout of the e-linac from electron gun to the beginning of the high energy transport tunnel.

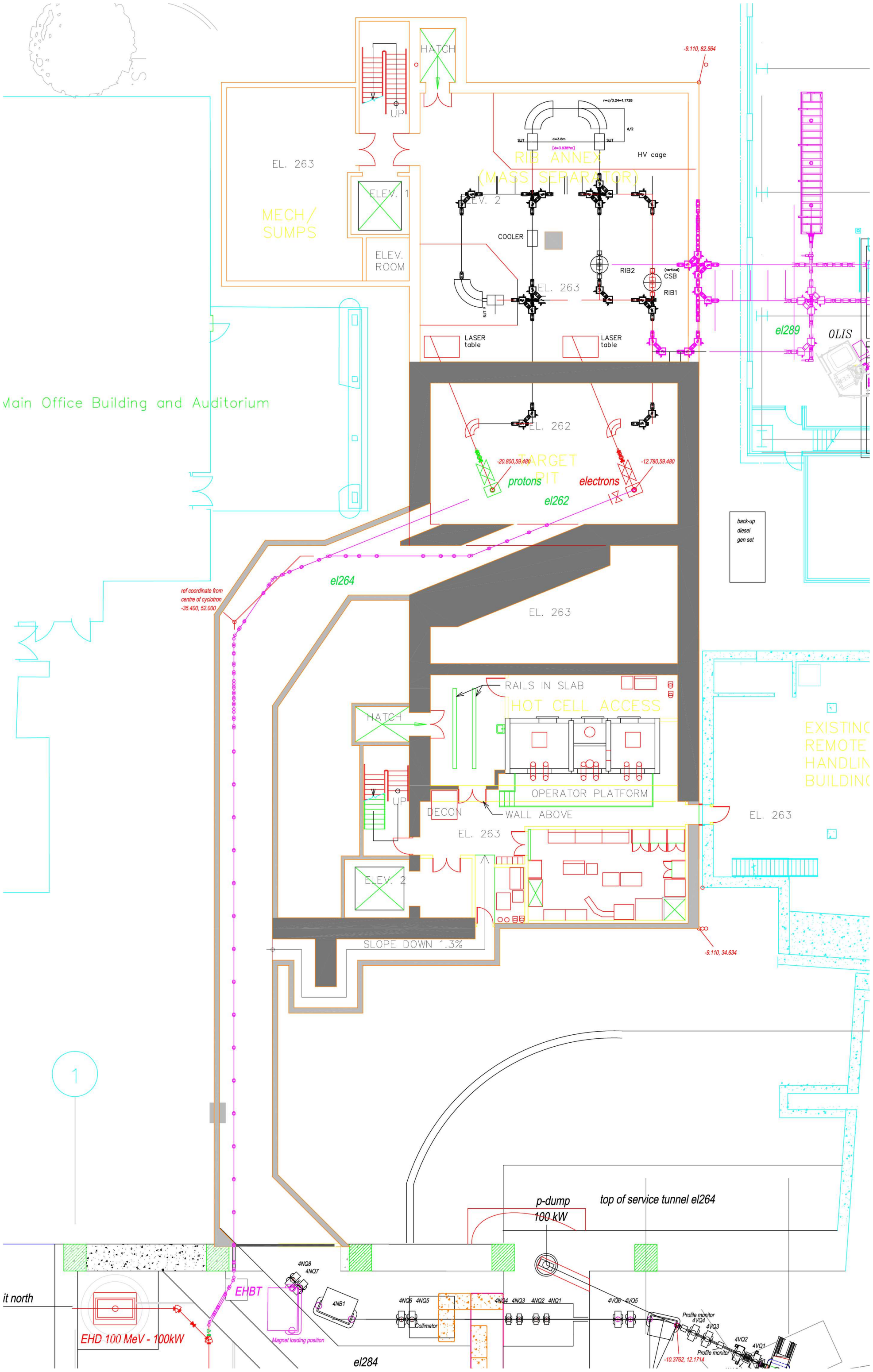

Figure 1.4: Schematic diagram of the layout of the e-linac from the high energy transport tunnel to the target stations.

1.2 Electron Beam Diagnostics

Beam diagnostics are an essential part of the e-linac design. Measurement of the beam properties are required both in the initial beam setup phase as well as during normal operation of the e-linac. The key properties of interest and techniques for their measurement are briefly introduced in the following sections.

Beam Position

Beam position monitoring is required to ensure the beam is being threaded through the e-linac without colliding into walls or beam-line elements and to minimize losses along the length of the e-linac. Non-intercepting methods for beam position monitoring are often used for Machine Protection Systems (MPS) and feedback control. The position of the beam within the beam pipe will be measured in a number of locations throughout the entire length of the e-linac including along the high energy transport line to the target stations.

The primary method for non-intercepting monitoring of beam position is through the Beam Position Monitors (BPMs). These devices measure the center of the charge flowing through the beam-line through the use of four pickup electrodes evenly spaced around the circumference of the beam-pipe. A passing bunch charge induces a voltage in the electrodes and by comparing the signal intensity from electrodes on opposing sides of the beam-pipe, the transverse position can be determined.

The electrodes may be either button type, or strip-lines. Button electrodes have low impedance and work best with short, high intensity bunches. Strip-line electrodes are more sensitive than buttons, but are mechanically more complex. In addition to beam position, strip-lines also provide directionality information which can useful in rings with counter rotating beams [10].

Intercepting methods may also be used for beam position measurements, but usually require the use of reduced beam currents and can be quite destructive to the beam. View Screen beam profile monitors provide the two-dimensional transverse beam profile, from which the beam position can be determined. Faraday Cups may also provide positional information when used in combination with a water cooled slit scanner.

Transmitted Beam Current

The beam current can be measured with intercepting devices such as a Faraday Cup, or non-intercepting devices such as a DC Current Transformer (DCCT).

Faraday cups are intercepting devices which when inserted into the beam-line capture all of the electrons striking it. This causes an increase in charge on the Faraday Cup and the resulting current is measured to determine the impinging beam current. In order to accurately measure the beam current, all of the electrons must stop within the device with minimal backscattering or knocking out of secondary electrons. Faraday Cups work best at low beam energy as the distance required to stop an electron increases with energy. The Faraday Cup must also be able to dissipate the beam energy deposited into the device which will cause the material to heat up.

A DCCT is a non-intercepting device that allows current measurement up to the full 10 mA beam current of the e-linac. A toroidal magnetic core surrounds the beam and couples to the magnetic field of the passing beam. The field produces a voltage in a wire coil surrounding the magnetic core which is proportional to the beam current with high linearity and accuracy.

In order to reach the ultimate precision, stray magnetic fields and temperature variations must be limited to a very low level. An insulating ceramic break in the beam pipe is generally used to force any extraneous currents around the outside of the core. To calibrate the system, the response to a precision current passed through a wire placed parallel to the beam, through the core of the DCCT, may be measured.

The use of two DCCTs at different points along the e-linac would provide a differential current measurement, signaling beam losses along the beam-line. The signal intensity from the BPM's may also be used to determine the beam current, although they require periodic calibration with either a DCCT or Faraday cup to provide an absolute current measurement.

Transverse Beam Profile

The transverse beam profile, or the shape of the beam in the plane transverse to the beam direction, is a very useful diagnostics measurement. Beam profiles are generally determined using intercepting methods, either through a View Screen which provides a two dimensional image of the beam intensity versus position, or wire scanners which give one dimensional projections of the profile across the scanning direction.

The beam profiles give information about the shape, size, and position of the beam.

View Screens, or Beam Profile Monitors as they are often called, are commonly used devices that provide images of the transverse profile of the beam as it passes through a conversion screen. The conversion screen emits light in the visible regime at the points at which the beam passes, whose intensity is ideally linear with particle intensity. Screens may emit light either through luminescent processes or Optical Transition Radiation. The emitted light can then be collected through focusing optics and imaged with a camera for analysis.

With wire scanners, a thin wire is moved across the beam creating a secondary particle shower which is proportional to the intensity of particles striking the wire. The electrons or photons in the shower are observed with scintillators placed downstream of the wire, providing the intensity of the portion of the beam intercepted by the wire.

The main advantage of wire scanners are that they can be used at higher beam currents than other intercepting beam profile monitoring devices. Since the wire can be moved across the width of the beam very quickly, the energy deposited in the wire, and thus the temperature rise, can be limited to safe levels. Wire scanners are also very resistant to radiation damage and contribute to much lower beam losses than devices that intercept the entire beam. The disadvantage is that they provide the profile in only one transverse dimension.

Beam Halo

Through several processes, such as phase space mismatch, space charge effects within bunches, and higher order modes present in the accelerating cavities and magnetic elements, a small fraction of particles are forced outwards forming a diffuse halo of particles surrounding the core of the beam [10]. Significant amounts of beam power may be present in beam halos which can be lost on the walls of beam pipes and accelerator cavities.

Measurement and minimization of the beam halo are crucial to decrease beam losses, protect the e-linac from damage, and to avoid activation of the accelerator components. The beam halo can be minimized through careful tuning of the elements of the e-linac.

A large dynamic range is required in diagnostics instruments to allow for the measurement of both beam halo and core properties, as the halo may be much less intense than the rest of the beam. Wire scanners are generally able to view the diffuse beam halo, although they provide only projections of the two dimensional profile. Additionally, while View Screens generally do not have the dynamic range to capture both the beam core and halo in a single image, by allowing the beam core to saturate the image, the beam halo may become visible in overexposed images.

Emittance

The beam emittance refers to the phase space occupied by the beam in six dimensional position and momentum space. A beam in which the particles have a small spatial separation and nearly all the same momentum is said to have a low emittance.

The emittance is generally projected into the three orthogonal phase dimensions, $\{x, p_x\}$, $\{y, p_y\}$, and $\{z, p_z\}$. For a transverse dimension u, the conjugate momentum p_u may be replaced by the divergence angle, $u' \simeq p_u/p$, where p is the total momentum of the beam. Given a normalized transverse phase space distribution, $\rho(u, u')$, then the moments of the distribution can be calculated as

$$\sigma_u^2 = \int (u - \langle u \rangle)^2 \rho(u, u') du du' \tag{1.1}$$

$$\sigma_{u'}^2 = \int (u' - \langle u' \rangle)^2 \rho(u, u') du du' \tag{1.2}$$

$$\sigma_{uu'} = \int (u - \langle u \rangle)(u' - \langle u' \rangle) \rho(u, u') du du' \tag{1.3}$$

The quantities σ_u and $\sigma_{u'}$ are the RMS widths, and $\sigma_{uu'}$ is the correlation. The RMS beam emittance is then defined as

$$\epsilon_{rms,u} = \sqrt{\sigma_u^2 \sigma_{u'}^2 - \sigma_{uu'}^2} \tag{1.4}$$

Another definition of the emittance is the 95% emittance, $\epsilon_{95\%}$. This is the phase-space area which contains 95% of the beam particles. The normalized emittance,

$$\epsilon_n = \beta \gamma \epsilon \tag{1.5}$$

where ϵ is the emittance and β and γ are the usual relativistic quantities, is an adiabatic invariant, remaining constant under acceleration. Focusing also does not change the total emittance of the beam, but rather swaps between position and momentum.

At low energy, before acceleration through the EINJ, an Allison type emittance scanner may be used to measure the beam emittance [11]. In this device, the beam first passes through an entrance slit, stopping all but a small portion of the beam. The resulting beamlets pass between two deflection plates with a voltage difference applied between them before coming to an exit slit. Depending on the angle at which the particles pass through the slit, a different voltage is required to deflect them such that they will pass through the exit slit and into a Faraday Cup.

The entire device scans across the beam, selecting beamlets at each position in one dimension. At each position, the voltage between the deflection plates is varied and the corresponding intensity reaching the Faraday Cup measured, providing a distribution of the beam particles' transverse position and momentum. The device gives the emittance in one transverse dimension and either a second device, or rotating the device by 90° about the beam-line, is required to provide the emittance in the perpendicular dimension. As this is a beam intercepting device, it is restricted to low beam energies and beam power.

At high energy, the *quadrapole scan* or *three monitor* methods are typically used to determine the beam emittance [12]. In the former, the strength of a quadrapole focusing magnet is varied with the beam size measured with a downstream profile monitor, either a wire scanner or View Screen. Through knowledge of the beam transport matrix, which describes how the beam properties propagate along the beam-line, the emittance can be extracted.

Similarly, in the three monitor method, three (or more) profile monitors spaced along the beam-line are used to measure the beam size at a number of locations. Again, by using the beam transport matrix, the beam emittance may be extracted. This method requires that the beam be not significantly affected by the profile measurement.

Beam Momentum and Energy Spread

The cavity phasing of the accelerating cryomodules compared to the RF phase of the beam may be optimized by maximizing the energy gain of the beam through the accelerating elements. If the electron bunches arrive within the accelerating cavities with the correct phase with respect to the RF accelerating voltage, the electrons will receive the optimal accelerating force and experience a slight bunching effect. If however the bunch phasing is incorrect or the bunches too long, not all the particles within a bunch will be accelerated by the correct accelerating voltage, leading to a spread in energy of the electrons within the bunch.

The momentum is measured within analyzing stations equipped with a dipole bending magnet, BPM's, and View Screens. The bend radius of the charged particle beam through the dipole magnetic field is dependent on particle energy – higher energy particles have more momentum and their path is deflected less through the magnetic field than lower energy particles within the same field. Measurement of the beam position with the BPMs determines the average bending angle of the beam and hence the average beam momentum. The extent of spatial spreading of the beam after passing through the dipole bend indicates the spread in energy. A View Screen located after the bend can be used to measure the distribution of particles.

1.3 Requirements of the View Screens

Successful operation of the e-linac requires accurate measurements of the beam properties. The View Screens have been designed to meet a series of requirements, ranging from operational or environmental specifications to requirements on the acquired beam properties, as specified in [13].

The nominal beam size in the different areas of the beam-line are shown in Table 1.2. The size of the beams may change by up to a factor of 5 times larger and down to 10 times smaller than the nominal sizes during the tuning of the e-linac [14]. The beam transport pipes in all sections of the e-linac are 50 mm in diameter and to ensure that the mounting structure of the target holder will not intercept the beam or its halo, the beam targets for the View Screens have been specified to also be 50 mm in diameter.

Area	Nominal Beam Size, σ	Screen Size	Field of View	Imaging Resolution
ELBT	3 mm	50 mm	50 mm	150 μm
EMBT	2 mm	50 mm	25 mm	100 μm
EHBT	1 mm	50 mm	25 mm	50 μm

Table 1.2: Summary of the nominal beam sizes expected in the different areas of the e-linac and the corresponding requirements on the View Screens.

In the ELBT, where beam sizes are the largest, the field of view of the camera will cover the entire area of the beam targets. The nominal beam sizes in the higher energy sections of the e-linac are smaller, so even though the target size is specified as the same size in all areas of the e-linac, the field of view is smaller in the EMBT and EHBT sections, covering only 25 mm at the center of the beam targets.

The requirement on imaging resolution comes from the need to resolve sub-structure within the beam profile down to a scale of $\sim$5% of the nominal beam size. The key factors affecting the imaging resolution are the pixel resolution and the ability of the imaging optics to focus the light emitted from the beam targets.

The location of the centroid of the beam must be determined relative to the other elements of the beam-line to an absolute uncertainty of $200\,\mu$m and a relative uncertainty of $25\,\mu$m. The uncertainty in the measurement of the beam size depends on the transverse size of the beam and should be 10% of the nominal beam size, $100\,\mu$m, $200\,\mu$m, or $300\,\mu$m in the ELBT, EMBT, and EHBT respectively. This places strict requirements on geometric calibration as well as requiring the use of correction factors to be applied to remove temperature and light collection effects in the acquired images.

As the View Screens are intercepting devices, they will contribute to energy losses in the passing beam. These losses must be kept below 2 W per device by limiting the current or duty factor of the beam when the beam targets are inserted into the beam. At low beam energy, less than a few MeV, the beam targets are completely intercepting and destructive. The entire beam is stopped within the target, with few electrons scattered out, mostly in the backwards direction. At higher energies, the beam will pass right through the target, losing some energy and undergoing multiple scattering.

Upon exiting the target, the beam must be able to be safely directed towards a beam dump to be safely disposed. The momentum aperture is the maximum deviation from the design momentum that an electron may have such that the focusing and steering elements along the beam-line can contain the particle. The relative momentum aperture of the e-linac is 2%.

Any elements of the View Screens that will be inserted into the beam-line have to be vacuum compatible from 10^{-9} Torr near the electron gun to 10^{-7} Torr in the EHBT. Materials that outgas are not permitted within the vacuum. The beam-line is held under high vacuum to minimize interactions of the beam with residual air molecules that would result in energy losses of the beam and unnecessary radiation.

Due to radiation produced by the e-linac, beam dumps, and target stations, the

View Screens are required to withstand up to 10 mSv per hour of radiation, predominantly X–rays, γ–rays, and neutrons. The camera and lenses are especially susceptible to radiation damage and will be replaced as required, but should last for at least one year to minimize downtime and replacement costs.

Control of the View Screens will be provided through the EPICS software from within the e-linac Control Room. Images will be acquired at rates of up to 10 Hz with the ability to synchronize image acquisition the arrival of beam pulses.

A total of 14 View Screens are required along the length of the e-linac. Four will be located along the ELBT line, and the remaining ten distributed throughout the EMBT and EHBT beam-lines.

1.4 Focus of This Work

Design studies have been performed to evaluate the performance of the View Screens under various operating conditions. This thesis describes the resulting design of the View Screens based on the requirements presented in the previous section.

Background information is provided in Chapter 2 about the luminescent and Optical Transition Radiation processes that take place within the beam targets to produce the visible light required for imaging the beam profiles. Design details of the beam targets and holder, imaging optics, and the structural elements are given in Chapter 3 and the image calibration and correction procedures that will be applied to the images as they are acquired is described in Chapter 4.

The simulations performed in the design studies are described in Chapter 5. These include a GEANT simulation of the interaction of the beam with the beam targets, a Finite Element Analysis of the the subsequent thermal response of the targets, and a ray tracing simulation used to optimize the configuration of the imaging optics. The results of bench tests of the imaging system and Chromox beam targets are discussed in Chapter 6. Further information regarding GEANT and thermal studies for additional candidate beam target materials is provided in the Appendices.

A prototype version of the ELBT View Screen will be completed and tested by August 2011 for installation into the ELBT beam-line for initial beam tests with the electron gun. The next two devices will be required the following month, incorporating modifications as required.

Chapter 2

View Screen Beam Targets

The basic elements of the beam profile monitor are the beam targets, which emit visible light as beam particles pass through them, and an imaging system to acquire images of the emitted light, resulting in a two dimensional image of the beam intensity as a function of position. The intensity of the light emitted by the beam targets must be linearly proportional to the beam particle density in order to accurately represent the transverse profile of the beam.

There are two main types of beam targets that are used in beam profile monitors. Targets that scintillate as beam particles pass through them are called scintillation targets. These are generally used for low current measurements as they can produce a relatively high amount of light. For use at higher beam currents, Optical Transition Radiation (OTR) targets can be used. These emit transition radiation in the optical spectrum at the interface between vacuum and target material and the response is generally very linear with respect to particle density. The properties of these two targets types as well as some commonly used target materials will be discussed in this chapter.

2.1 Scintillation Targets

Scintillation targets, or screens as they are sometimes called, are beam targets that emit scintillation light when excited by the passage of beam particles. The light is emitted close to the point where the beam particle passed though the screen, resulting in a pattern of light on the screen corresponding to the density profile of the beam.

There are many types of scintillating materials that are used for View Screen beam targets. A few commonly used materials are Chromox, YAG:Ce, and LYSO:Ce. Chromox is the trade name for a chromium enhanced aluminum ceramic manufactured by Morgan Technical Ceramics with a composition of 99.5% Al_2O_3 (alumina) and 0.5% Cr_2O_3. There are other manufacturers that supply materials similar to this that are also commonly referred to as Chromox.

Chromox is a ceramic material composed of many small grains, 10 - 15 μm or larger in size. Chromox is mostly opaque, so most of the scintillation light is emitted from the surface, although some light disperses through the bulk of the material, resulting in a lower limit to the achievable imaging resolution. For a 0.5 mm Chromox screen at 45°, this resolution limit has been reported as approximately 300 μm [15].

The emission spectrum of Chromox is peaked at around 700 nm [16] resulting in a reddish coloured scintillation light. The decay time of the scintillation is given in the range of several milliseconds [17], making it a relatively slow scintillation screen. This property limits the usefulness of Chromox for the e-linac View Screens as the ARIEL electron beam is expected to have important time varying characteristics at the scale of tens of μs which would be washed out with a long scintillation decay time.

YAG:Ce is a cerium doped yttrium aluminum garnet, $Y_3Al_5O_{12}$. The amount of cerium dopant included varies but is typically on the order of 0.2%. YAG:Ce screens are prepared in one of two ways, either as a thin layer of powder deposited on a substrate, or in single-crystalline form. YAG:Ce is a very fast scintillator, with a decay time of approximately 70 ns, and the emission spectrum is peaked at a wavelength of 550 nm [18]

In crystalline form, YAG:Ce is transparent and scintillation photons are visible from points throughout the thickness of the screen. Therefore if the screen is oriented at an angle with respect to the camera, as is common procedure with View Screens, a broadening of the beam size would be apparent due to the viewing angle as shown in Figure 2.1.

In some applications an intensity dependent beam enlargement of the imaged beam size have been reported for YAG:Ce screens with high brilliance electron beams, when compared to other diagnostics equipment, such as wire scanners and OTR screens. This phenomenon has generally been observed for beams with charge densities of $\Sigma > 0.01\,\mathrm{pC}/\mu\mathrm{m}^2$ [19, 20, 21].

The maximal charge density for a Gaussian beam distribution can be calculated by integrating the maximum current density, J_{max}, over the timescale of the scintillation emission, $\tau = 100\,\mathrm{ns}$:

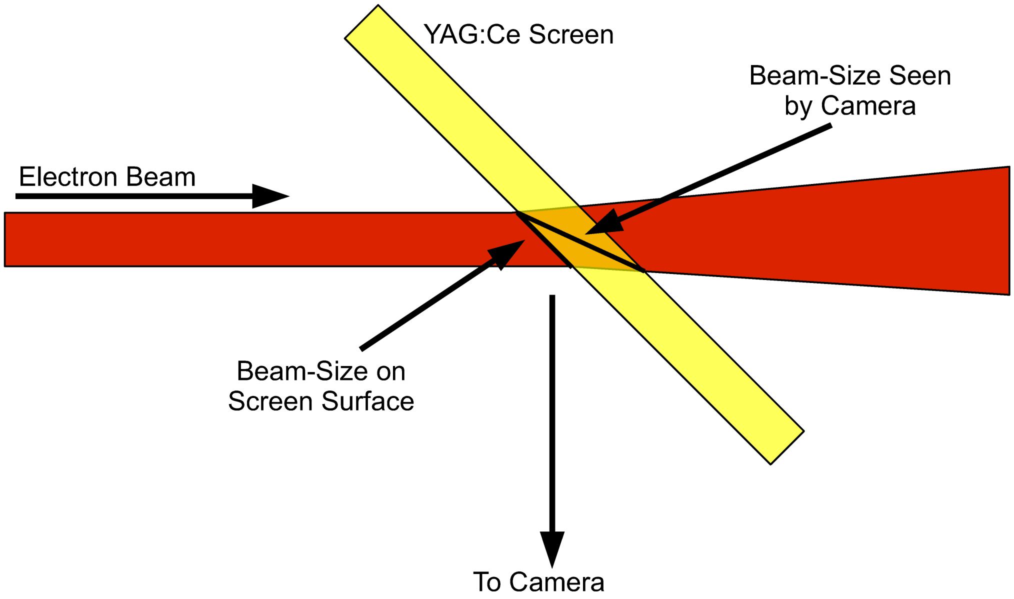

Figure 2.1: Artificial broadening of the beam profile image caused by a transparent YAG:Ce screen mounted at 45°.

$$\Sigma_{max} = \int_0^\tau J_{max}(t)dt = \frac{I}{2\pi\sigma^2}\tau, \quad \tau = 100\text{ns} \tag{2.1}$$

Where I is the beam current, and σ the width of the electron beam.

For the ARIEL e-linac, the maximum charge density for a 1 mm electron beam at 1 μA is then $\Sigma_{max} = 1.6 \times 10^{-8}\,\text{pC}/\mu\text{m}^2$. This is much less than $0.01\,\text{pC}/\mu\text{m}^2$ and therefore this resolution limit for YAG:Ce screens should not be reached under normal operating conditions.

LYSO:Ce is another fast scintillator with slightly higher light output than YAG:Ce. LYSO:Ce is a crystal with chemical formula $\text{Lu}_{2(1-x)}\text{Y}_{2x}\text{SiO}_5$ doped with Cerium, where x refers to the atomic fraction of Yttrium compared to Lutetium. Yttrium has little effect on the scintillation properties of the material, but is included to differentiate the material from the patent protected LSO:Ce [22]. Typical Yttrium fractions are around 10%.

The time constant for LYSO:Ce scintillation is 40 ns and the emission spectrum is peaked at 400 nm [22]. LYSO:Ce has a slightly higher light yield than YAG:Ce, but is also more dense and therefore contributes to higher beam losses and heating.

The optical properties of scintillating materials such as the light yield are affected by the temperature of the beam target. The light yield decreases with temperature as a result of thermal quenching of the luminescent centers and thermally induced ionization of excited electrons, in which the electrons escape to the conduction band, rather than emitting scintillation photons [23].

This temperature dependence causes a non-linearity in light yield for beam currents high enough to significantly alter the temperature of the beam target. For a Gaussian shaped beam, the target temperature will be the highest near the center of the beam, decreasing the amount of light emitted per beam particle. This causes the width of beam to appear wider as viewed by the View Screen.

A correction may be applied to attempt to correct for the decrease in light yield with temperature, but would be heavily dependent on the temperature distribution of the beam targets which cannot be measured directly. Instead, a correction would have to be based on simulations of energy deposition and thermal response, leaving room for accumulated errors to reduce the effectiveness of such a calibration. This is discussed in greater detail in Section 4.3.

The light yield of YAG:Ce decreases with temperature by approximately 0.1% per °C up to $\sim$ 200°C as shown in Figure 4.1. The quenching temperature of YAG:Ce luminescence is around 430°C [24]. LYSO:Ce exhibits an approximately 0.2% per °C decrease in light yield up to $\sim$ 100°C and increases to a 0.4% per °C decrease by 175°C [23].

2.2 Optical Transition Radiation

When a charged particle crosses the the boundary between two materials with different relative permittivities, electromagnetic radiation called transition radiation is emitted. This radiation has a broad spectrum, covering the entire visible regime, hence the name Optical Transition Radiation (OTR).

The phenomenon was theoretically predicted by Frank and Ginsburg in 1946 [25] and was demonstrated for the first time in 1959 by Goldsmith and Jelly, using intense low energy proton beams striking metal surfaces [26]. OTR was first applied to beam diagnostics in 1975 by Wartski *et al.* with an electron beam on aluminum, silver, and gold plates [27]. OTR beam profile monitors are now in use at most electron and proton accelerators to perform beam profile measurements.

As a charged particle approaches the boundary between two media, the moving fields of the charged particle induce a time varying polarization at the interface. The radiated fields from this polarization combine coherently to form the emission of transition radiation [28, 29]. The process is a surface phenomenon with the radiation being emitted within the first 100 Å of the surface [30].

When a charged particle crosses a thin foil in a vacuum, it crosses two boundaries. As it passes the first boundary from vacuum to foil material, optical transition radiation is emitted in the direction of specular reflection and is referred to as the *backward radiation*. As the charged particle exits the other side of the foil, crossing from foil material to vacuum, the *forward radiation* is emitted in the direction of the exiting particle's velocity. The optical transition radiation is peaked at an angle, θ_{peak}, as measured from either the reflection axis for backward radiation or the particle's velocity for forward radiation, as shown in Figure 2.2.

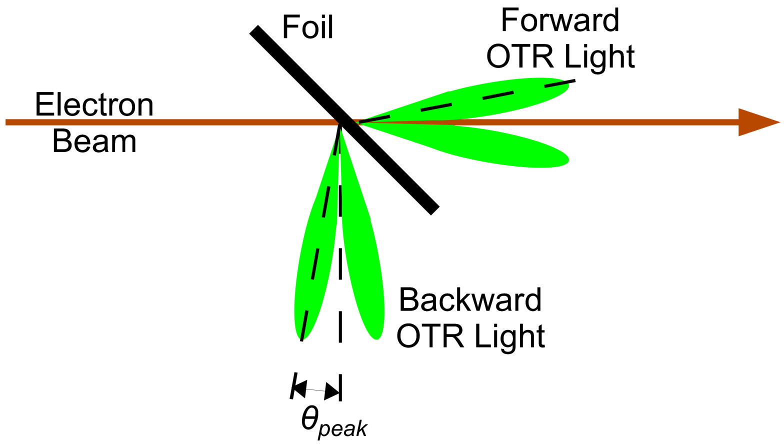

Figure 2.2: The Optical Transition Radiation emitted as an electron beam passes through a beam diagnostics foil

The OTR emission distribution is dependent on the energy of the charged particle, the relative permittivity of the two materials, ϵ_1 and ϵ_2, and the orientation of the surface boundary, ψ, defined as the angle between the incoming velocity vector and the normal to the surface interface.

For low energy electrons, $E < 50\,\text{MeV}$, the OTR emission distribution has been derived from Maxwell's Equations [31]. The expression obtained here is for the backward radiation from electrons crossing the boundary between two semi-infinite planes. It is possible to apply this result to a foil with finite dimensions provided that the conductivity is sufficiently high and because the emission takes place primarily within the first 100 Å of material, which is much less than the thickness of the foils.

Defining $\boldsymbol{\kappa}$ as the wave vector of the emitted radiation, then the two angles that describe the direction of the emission are θ, the angle between the normal to the surface, $\hat{\mathbf{n}}$, and $\boldsymbol{\kappa}$, and ϕ, the angle between the projections of the velocity vector and the wave vector $\boldsymbol{\kappa}$ on the interface. A summary of these variables is illustrated in Figure 2.3.

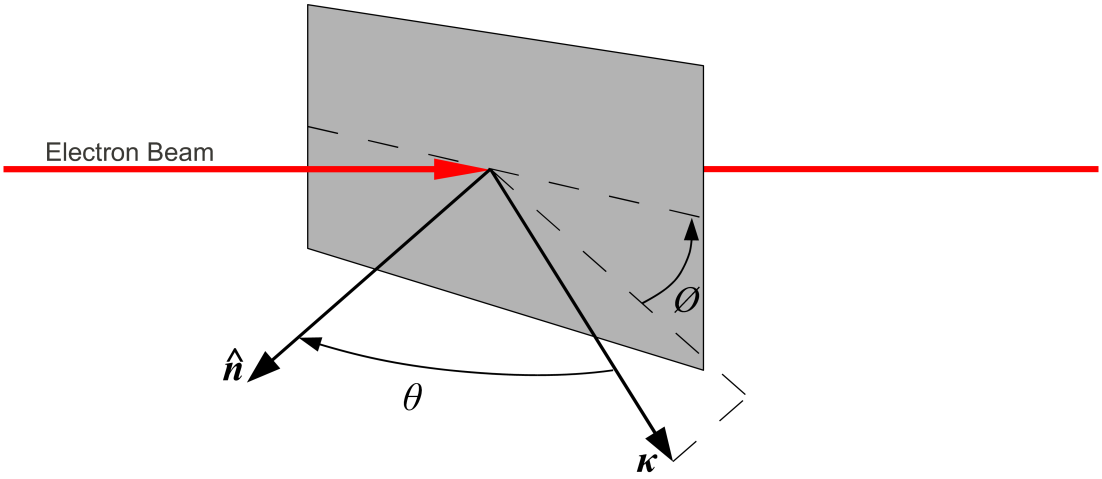

Figure 2.3: Geometric variables of the OTR emission distribution.

The expression for the backward OTR emission distribution is then given in terms of the horizontal and vertical polarization components:

$$\begin{aligned}
&\frac{d^2 I_{\parallel}}{d\Omega d\omega} = \\
&\quad \frac{e^2\sqrt{\epsilon_1}}{\pi^2 c}\frac{1}{4\pi\epsilon_0}\frac{\beta^2\cos^2\psi\cos^2\theta|\epsilon_2-\epsilon_1|^2}{[(1-\sqrt{\epsilon_1}\beta\sin\theta\cos\phi\sin\psi)^2-\epsilon_1\beta^2\cos^2\theta\cos^2\psi]^2}\frac{1}{\sin^2\theta} \\
&\quad \left|\frac{\sin^2\theta(1-\sqrt{\epsilon_1}\beta\sin\theta\cos\phi\sin\psi+\sqrt{\epsilon_2-\epsilon_1\sin^2\theta}\beta\cos\psi-\epsilon_1\beta^2\cos^2\psi)\ -\ \ldots}{[1-\sqrt{\epsilon_1}\beta\sin\theta\cos\phi\sin\psi+\sqrt{\epsilon_2-\epsilon_1\sin^2\theta}\beta\cos\psi][\sqrt{\epsilon_2\epsilon_1-\epsilon_1^2\sin^2\theta}+\epsilon_2\cos\theta]}\right. \\
&\quad \left.\frac{\sqrt{\epsilon_1}\beta\sin\theta\cos\phi\sin\psi\sqrt{\epsilon_2-\epsilon_1\sin^2\theta}\beta\cos\psi}{}\right|^2
\end{aligned} \tag{2.2}$$

$$
\begin{aligned}
&\frac{d^2 I_\perp}{d\Omega d\omega} = \\
&\quad \frac{e^2\sqrt{\epsilon_1}}{\pi^2 c}\frac{1}{4\pi\epsilon_0}\frac{\beta^6\cos^4\psi\sin^2\psi\sin^2\phi\cos\theta^2|\epsilon_2-\epsilon_1|^2}{[(1-\sqrt{\epsilon_1}\beta\sin\theta\cos\phi\sin\psi)^2-\epsilon_1\beta^2\cos^2\theta\cos^2\psi]^2} \\
&\quad \frac{1}{\left|(1-\sqrt{\epsilon_1}\beta\sin\theta\cos\phi\sin\psi+\sqrt{\epsilon_2-\epsilon_1\sin^2\theta}\beta\cos\psi)(\sqrt{\epsilon_2-\epsilon_1\sin^2\theta}+\cos\theta)\right|^2}
\end{aligned}
\tag{2.3}
$$

The backward OTR emission distribution for 10 MeV electrons crossing from vacuum, $\epsilon_1 = 1$, to pyrolytic graphite, $\epsilon_2 = 13.5$, at an angle of 45° is shown in Figure 2.4, where both the distance from the emission point and the surface color indicate the intensity of the emitted radiation. The electron beam is indicated by the vertical red line and the blue line represents the direction of the reflection axis.

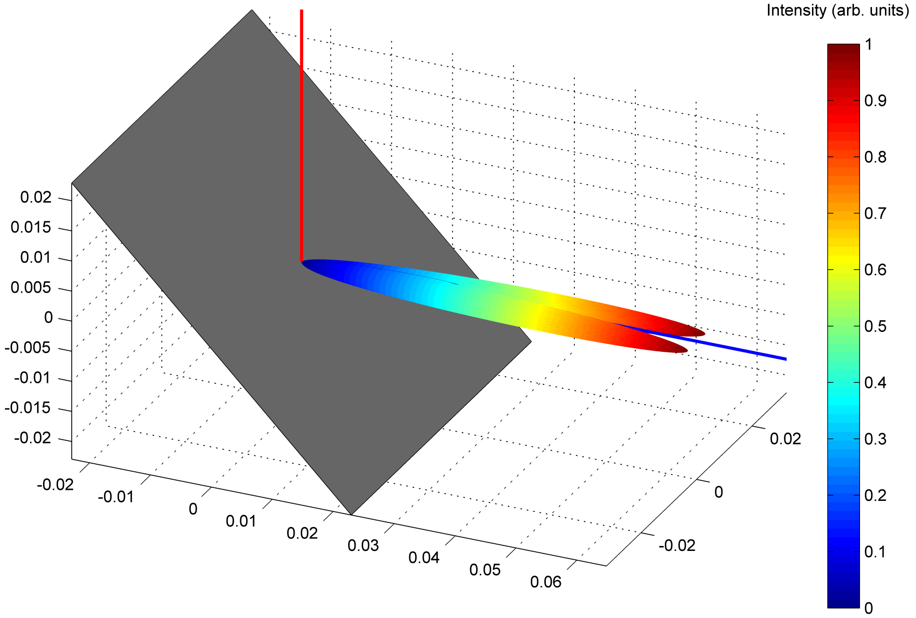

Figure 2.4: OTR emission distribution for 10 MeV electrons on Pyrolytic Graphite.

The emission of OTR light from Pyrolytic Graphite is peaked in two lobes, on either side of the reflection axis at $\phi = \pm\pi/2$. For highly reflective materials, the two lobes join together, forming a cone of emission about the reflection axis. The direction of maximal emission is located at an angle θ_{peak} from the reflection axis. This angle is related to the Lorentz factor, γ by $\theta_{peak} \simeq 1/\gamma$. At 10 MeV θ_{peak} is approximately 2.8°, while at 50 MeV the radiation is peaked at $\sim 0.6°$.

The OTR emission distribution depends strongly on the properties of the foil material, mainly the relative permitivity. For the backward radiation, the intensity of the emitted OTR light can be shown, through the expressions (2.2) and (2.3) with $\beta \sim 1$ and $\epsilon_1 \sim 1$, to be approximately proportional to the *reflectivity* of the material

$$I \propto \left| \frac{\sqrt{\epsilon_2} - 1}{\sqrt{\epsilon_2} + 1} \right|^2 \tag{2.4}$$

Other important properties of the foil material are the melting temperature and thermal conductivity, which are important when determining the maximum current the foils can withstand without damage, and the atomic number of the element, which reflects the degree of energy loss and scattering of the beam as it passes through the foil. These properties are summarized in Table 2.1 for some common OTR profile monitor foil materials, aluminum, titanium, and pyrolytic graphite [32, 33, 34].

Aluminum has the highest OTR light output of the three materials presented, however it's low melting temperature make it an unsuitable choice for the high average current of the e-linac. Titanium has a much higher melting point than Aluminum and a fairly high light output, but has a high atomic number and therefore contributes to significantly higher beam losses than either Aluminum or Pyrolytic Graphite. Although Pyrolytic Graphite has a low reflectivity, its high melting temperature and thermal conductivity make it robust for use at relatively high beam currents, and with it's low atomic number causes less interference to the passing electron beam.

	Aluminum	Titanium	Pyrolytic Graphite
Atomic Number, Z	13	22	6
Relative Permittivity, ϵ_R	-42+12i	-7+7i	13.5
Reflectivity	$\sim 90\%$	$\sim 65\%$	$\sim 35\%$
Melting Temperature	660°	1670°	$> 2500°$
Thermal Conductivity, at 300 K	230 W/m·K	220 W/m·K	345 W/m·K

Table 2.1: Material properties of the candidate OTR foil materials.

Chapter 3

Design of the View Screens

The main components of a View Screen system are the OTR and scintillation beam targets, imaging optics, and the image acquisition system. Additionally, there are the mechanical elements such as the beam target holder, actuator, and housing to contain the imaging optics. Figure 3.1 shows the the main elements of the View Screen design.

The entire structure is mounted onto a beam diagnostics box which holds many of the diagnostic devices such as the wire scanners and Faraday Cups. Also mounted on this box are the turbo and ion pumps for maintaining high vacuum and the RF shield used to electromagnetically shield the electron beam from the retracted diagnostics devices when they are not in use. The beam targets are moved in and out of the beam by an actuator located on the top port of the diagnostics box. In normal production runs the targets are moved out of the beam and are inserted only when imaging is to take place.

The targets are oriented such that they can be viewed by the imaging system, located to the left of the diagnostics box in the figure. Light emitted from the targets passes through a viewport window on the diagnostics box and down a light-tight passage into the camera box. The optical elements and camera are placed inside this enclosure to provide a dark environment for imaging and to protect the radiation sensitive elements behind lead shielding.

For illumination to be used in calibration procedures, light sources are installed either on the port opposite the camera, to provide *back-light*, or on the side of the diagnostics box as a *front-light*, to illuminate the front face of the targets. The back-light is the preferred option for the light source as it also provides a means for characterizing radiation damage, but is not always available due to space restaints.

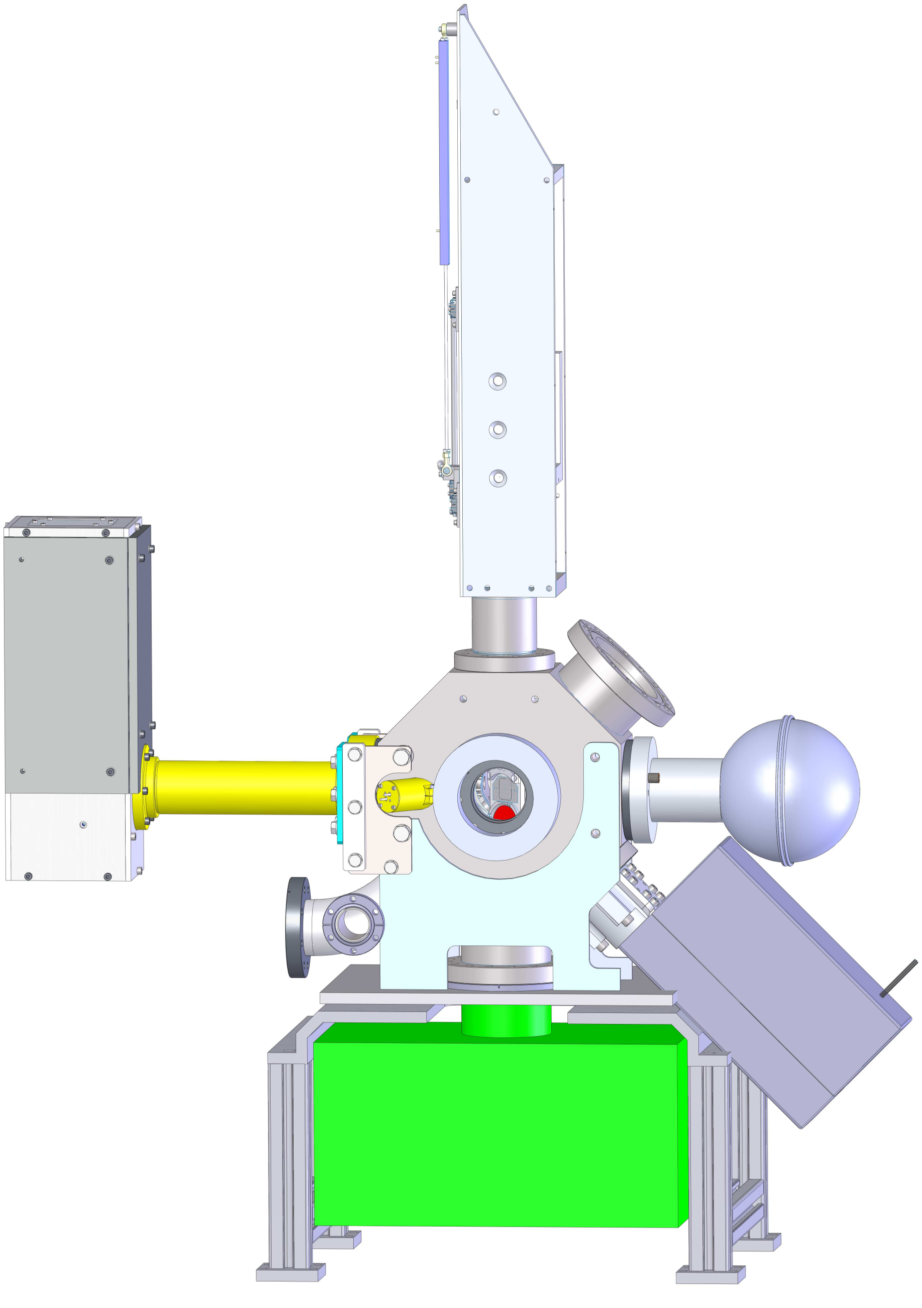

Figure 3.1: The View Screen mounted on the ELBT diagnostics cross. The camera box containing the imaging optics and camera is located to the left of the diagnostics cross, the actuator on the top port, and the back-light on the port opposite the camera box. Also shown in this image is the wire scanner, located on the bottom–right diagnostics port.

3.1 Elements of the View Screen

3.1.1 Targets

Two types of beam targets will be used for the View Screens to provide usage over a wide range of beam currents. Scintillation targets will be used for low currents as these have a higher light output than OTR targets, but must be thicker and will contribute to higher beam losses and scattering. OTR targets can be used at beam energies of 10 to 50 MeV. Additionally, a calibration target will also be installed on each device, to perform geometric calibration and distortion correction.

The beam targets will be circular with a diameter of 50 mm, approximately the same size as the beam transport tube. This is to ensure that the electrons pass through the beam targets, rather than striking the target holder, causing increased beam losses.

The scintillation targets will be single crystal YAG:Ce screens. Scintillation screens will be mounted on View Screens in all areas of the beam-line to provide coverage from a few nA of beam current, up to several μA. The targets will be mounted at 45° to the beam to be in the same plane as the OTR and calibration targets.

In the EMBT and EHBT beam-lines, the scintillation screens will be 0.2 mm in thickness. At 10-50 MeV, the electrons will lose only a small fraction of energy while traversing the screens, and will pass right through. The screens are thin to minimize energy losses and scattering as well as to decrease the optical effect of light emitted through the thickness of the screens. Since the energy deposited within the screens increases approximately proportionally with screen thickness, the thickness will have little effect on the maximum temperatures of the screens as the volume to be heated increases at the same rate.

At 300 keV, electrons will be stopped within the first 100 to 200 μm, with most of the scintillation light emitted close to the location of energy deposition. Therefore, in the ELBT the screens will be 0.5 mm in thickness as the extra material will decrease the rise in temperature and should not affect the imaging resolution to a great extent. If the resolution does suffer in initial beam tests, the screens may be replaced with thinner screens, down to 0.2 mm, if required.

The OTR beam targets will be constructed from 10 μm pyrolytic graphite foil. Pyrolytic graphite has a high thermal conductivity, allowing for the rapid dissipation of energy deposited by passing electrons, and a high melting temperature as to avoid damage to the foil. The OTR targets will be mounted at 45° to the beam such that the reflection axis, and therefore the peak of the emitted backwards radiation, will be oriented at 90° to the beam, and directed out the viewport window and towards the optical imaging components.

The OTR targets will only be included in the diagnostics stations with beam energies of 10-50 MeV. Below this energy, the intensity of the OTR radiation is too low and the emission distribution too spread out to provide adequate levels of light to perform imaging of the beam profile. The field of view will cover only the central 25 mm of the 50 mm diameter OTR foils.

The calibration target is an aluminum sheet with holes located on a grid pattern. This target will only be used when the beam is off as it would damage the target and create unacceptable beam losses. The pattern on the target will be illuminated by either the front or back light. By imaging this target, the image coordinates can be calibrated to the measured locations of the corresponding target markings.

In addition to the grid pattern, there will be an extra hole on the calibration targets located at a non-grid location that can be used to confirm the orientation of the target image. This off-grid hole is positioned such that it cannot be misinterpreted through any rotations or mirror transformations that may occur in the image acquisition or post-processing. Figure 3.2 shows the layout of the calibration target holes and their locations with the target center as the origin.

In the ELBT, the calibration target will be the same size and shape as the beam targets, 50 mm in diameter, to cover the entire field of view. The holes will be 0.8 mm in diameter and spaced 7 mm apart. In the EMBT and EHBT, the field of view covers approximately a 25 mm by 25 mm area of the beam targets, and the calibration target need only cover this reduced area. The holes will be slightly smaller at 0.5 mm in diameter and spaced at 5 mm apart.

As the calibration target will also be mounted at 45°, the thickness of the material will partially block the hole on one side. This will cause a shift in the location of the center of the hole by a distance of $t/2\sqrt{2}$, where t is the thickness of the material. Without adjusting the positions of the target markings by this correction factor, the reconstructed beam position would be biased in one direction.

Also located on the calibration target is a survey marker scribed onto the aluminum surface. Before installation onto the target holder, the locations of each of the target markings will be measured in reference to this survey marker. Upon installation

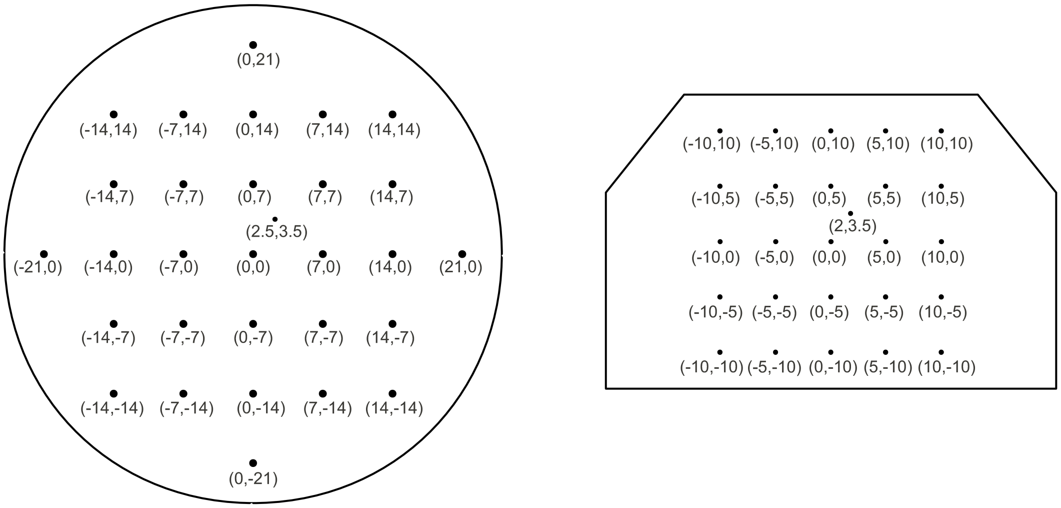

(a) ELBT calibration target pattern, covering the entire 50 mm field of view.

(b) EMBT / EHBT calibration target pattern, covering the reduced 25 mm field of view.

Figure 3.2: The layout and locations of the calibration markings on the calibration target.

of the target holder onto the actuator assembly, the survey marker on the calibration target will be measured in reference to another survey marker on the outside of the actuator housing. This marker's position will be determined after installation onto the diagnostics box, providing a means of translating positions determined by the View Screen to a coordinate system referenced to the rest of the beam-line.

3.1.2 Target Holder and Actuator

The targets are mounted onto a target holder which is attached to the target actuator. The actuator moves the entire assembly in and out to insert the various targets into place in the beam-line, and retracts the holder out of the beamline when not in use.

The targets are all mounted on the holder in the same orientation, at 45° to the beam axis, such that when in place, each target will be in focus across the entire field of view of the imaging acquisition system. This is also required so that the geometric calibration is consistent among targets.

In the ELBT section of the beam-line, there is only need for the scintillation and calibration targets as the beam energy is too low to use OTR. The calibration target here is the same size as the scintillation target as the field of view in this section covers the entire 50 mm target. At beam energies of 10 MeV and greater, all three targets, OTR, scintillation, and calibration, will be mounted on the holder, although the calibration target here is somewhat smaller here.

Since the image calibration need only be performed periodically, the calibration target will be located at the top of the target holder to reduce the travel distance of the actuator to extend the lifetime of the mechanical components of the actuator. In locations that include an OTR target, it will be located in the middle position to place it closer to the top of the holder to improve thermal conduction. Figure 3.3 shows the target holder for the EMBT and EHBT View Screens with the three targets: calibration, OTR and scintillation.

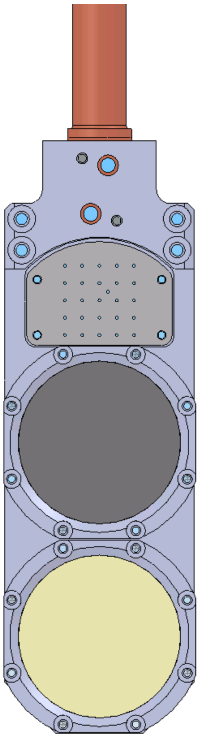

Figure 3.3: The EMBT / EHBT target holder. The OTR target is mounted in the middle position and the YAG:Ce scintillation target on the bottom.

The beam targets will each have a clearance hole through the target holder in the direction of the beam axis to allow the beam to pass through without hitting the holder. Because the targets are mounted at 45°, the clearance hole is elliptical in shape relative to the beam direction with dimensions 34 mm by 48 mm. The calibration target also has a clearance hole which is oriented 90° to the beam to be parallel to the optics axis to allow light from the back-light to shine through the target markings.

In addition to holding the targets in place, the target holder must also dissipate the heat deposited in the targets from the electron beam. Since the beam profile monitors may only contribute up to 2 W of total beam losses of the electron beam, the amount of thermal energy energy gained by the beam targets will always be less than this. Therefore, the target holder will be required to dissipate no greater than 2 W of thermal power. This is to be achieved through passive cooling through the copper actuator rod to which the target holder attaches to. If the thermal load is increased, a water cooling option is available by pumping cold water through the hollow copper rod to increase thermal conduction.

Since the targets will be in vacuum, heat dissipation through convection is non-existent and radiative thermal cooling is minimal. Good thermal contact between the targets and holder is therefore imperative as thermal conduction down the target holder is the only significant means of removing heat in the targets.

The YAG:Ce scintillation target is a rigid free-standing disc. The target will be held in place on the target holder by a retaining ring, fastened over the edge of the disc, and held by 8 fasteners. By tightening the ring in a large number of places, a higher degree of thermal contact is ensured. To increase contact points with the holder, the mounting ring may be machined with a *wavy* bottom surface to force contact in between fastener locations.

The Pyrolytic Graphite is a thin foil and requires tensioning to maintain a smooth, wrinkle-free surface. The method of mounting will be optimized when a sample piece of pyrolytic graphite is acquired, but will involve sandwiching the edge of the foil between two surfaces. A matching ridge and groove machined into the surface of the mounting rings would assist in grabbing and tensioning the foil, provided the material can withstand being bent without fracturing. This technique would also ensure good thermal contact around the entire edge of the target.

Since no beam will pass through the calibration target, no special mounting is required. The calibration target is simply a flat sheet of aluminum and can therefore be attached with fasteners along the edge of the target.

The actuator will move the target holder at a rate of ~50 mm/s and will take approximately 3 to 4 s to completely insert or retract. The actuator has been designed so that the stepper motor may be removed to allow the target holder to be retracted by hand in case of failure without breaking the vacuum inside the beam-line.

The requirement on the absolute uncertainty of the beam center position measured with the beam profile monitor is 0.2 mm. This requires that the positioning accuracy of the actuator when inserting the calibration target into the beam-line to be less than this. For this reason, the actuator includes a linear potentiometer to provide positional feedback with a resolution of < 0.1 mm and limit switches at the beginning and end of the travel.

3.1.3 Imaging Optics

The light emitted by the beam targets is collected and focused onto a CCD sensor for image capture through the optical imaging elements located within the camera box, as shown in Figure 3.4. The light emitted from the beam targets passes through the view port window of the diagnostics cross (not shown), through the light tube shown in yellow in the figure, and into the camera box. Inside the camera box, the light is reflected off a mirror, through an iris, and is focused by the lenses onto the camera's CCD sensor.

In the ELBT, where space is limited, the camera box is mounted such that the light is reflected upwards, to avoid conflict with the turbo-pump mounted on the port below the camera box. In the EMBT and EHBT, the camera box will be mounted in the downwards orientation so that the heavy radiation shielding will be located lower to the ground. There is less competition for space after the ELBT beam-line as there are fewer diagnostics devices required and more space in which to mount them in.

The nominal RMS beam-size in the ELBT is 3 mm and the required field of view is 50 mm wide such that the entire beam target is in view. In the EMBT and EHBT the size of the beam is smaller and even though the size of the targets is the same as the ELBT, the field of view need only cover 25 mm at the center of the target. The two different field of views require different optics configurations to provide the correct magnification of the image.

Since the targets are mounted at 45° to the beam-line, the circular beam targets appear elliptical in shape when viewed from the location of the camera. The size of the camera's CCD sensor, as discussed in the next section, is 6.4 mm × 4.8 mm. To fit the entire image of the 50 mm target onto the camera's CCD will require demagnification by a factor of $M_{50} = 0.128$. In the EMBT and EHBT, the field of view is half the size, 25 mm, and requires a less demanding demagnification of $M_{25} = 0.256$.

Lenses are used to collect as much of the light emitted from the beam targets

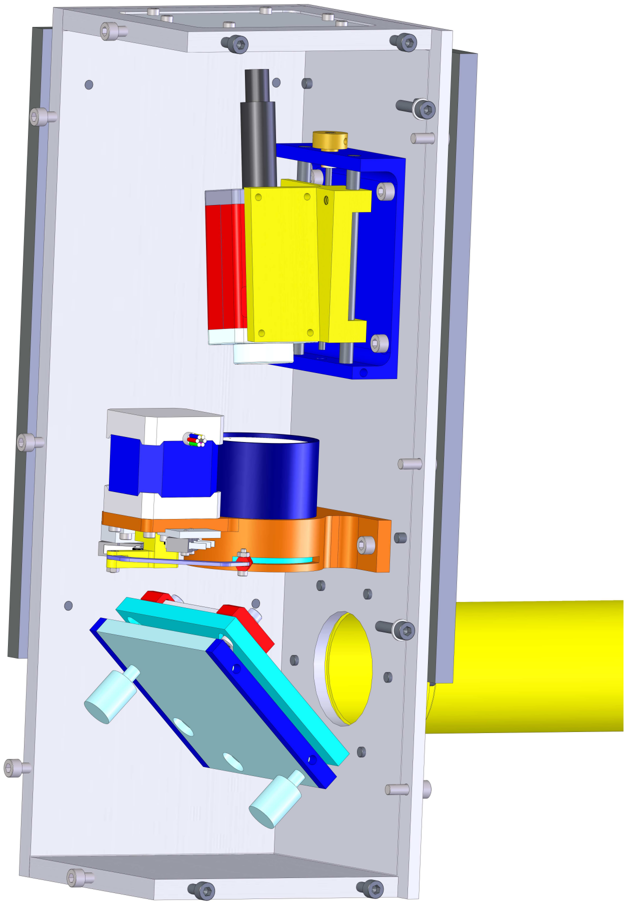

Figure 3.4: The layout of the imaging optics within the camera box.

as possible and focus it onto the CCD sensor of the camera. For this reason, it is advantageous for the lenses to have a large diameter and to be as close to the beam targets as possible to collect the most light. However, the sensitivity of the glass lenses to radiation and the selection of commercially available lenses must also be taken into account when selecting an optical design.

Taking these considerations into account, a ray tracing simulation, as described in detail in Section 5.3, was used to determine the optimal optics configuration, defining the locations of the optical elements and focal lengths of the lenses.

The following is a brief description of the main elements of the imaging optics system.

Mirror

A mirror, mounted at 45° to the optics axis, is used to reflect the visible light emitted from the beam targets out of the direct line-of-sight of the beam-line. This is done so that the radiation sensitive optical elements, the lenses and camera, can be protected from the damaging radiation emanating from the beam-line behind lead and polyethylene shielding. The mirror is a first surface polished aluminum mirror on a glass substrate. The glass substrate will darken over time from radiation exposure, however this will not affect the performance of the mirror as the radiation hard aluminum is mounted on the front facing surface.

The mirror is mounted on a two-axis adjustable mirror mount attached to the camera box. The mount has two adjustment knobs to adjust the mirror angle in two dimensions for optical alignment to center the image on the CCD sensor.

Lenses

The light is focused through two achromatic doublet lenses. These are lenses constructed of two layers of different types of optical glass which have been designed to minimize on-axis spherical and chromatic aberrations. Spherical aberrations are the errors in focusing caused by lenses being constructed with spherical surfaces, rather than the ideal parabolic shape. Lenses are made this way to reduce manufacturing costs, although it decreases the performance of the lenses. Chromatic aberrations are due to the dependence of the index of refraction on the wavelength of light, causing light of different colours to be focused to different locations. By pairing two surfaces of different materials together, this color separation is minimized, and light across the visible regime is focused in approximately the same way.

Within the different lenses employed in this design, there are several different types of optical glass, each containing slightly different components. The glass types are given a number and letter designation based on their chemical makeup as listed in Table 3.1. The lenses also have an anti-reflection MgF_2 coating. Some of these materials, such as N-BK7 due to it's boron content, will darken over time with radiation exposure making it important for the lenses to be shielded behind lead and polyethylene to extend this lifetime.

The lenses are 50 mm in diameter, although the use of an iris will limit the illuminated area as will be discussed shortly. The pair of lenses are held in place within a holding tube by threaded retaining rings which are tightened up against the lenses.

	Lens	Composition	
ELBT	300 mm FL	N-BaK4	Barium Crown glass
		N-SF10	Dense Flint Glass
	75 mm FL	N-BaF10	Barium Flint glass
		N-SF10	Dense Flint glass
EMBT / EHBT	500 mm FL	N-BK7	Borosilicate (Crown) glass
		N-SF5	Dense Flint glass
	150 mm FL	N-BaK4	Barium Crown glass
		N-SF10	Dense Flint Glass

Table 3.1: The types of optical glass within the achromatic lenses used in the imaging optics.

In the ELBT optics, a 300 mm focal length and 75 mm focal length lens are used, and in the EMBT and EHBT, 500 mm and 150 mm focal length lenses are used to provide the proper focusing and image magnification. The placement of these lenses is discussed in Section 3.1.4.

Iris

Before entering the lenses, the light must first pass through an iris. The iris is used to control the area through which the light passes to minimize spherical aberrations, and the amount of light collected and to control image intensity. When wide open, the iris aperture has a maximum diameter of 41 mm and can close down to a 1.2 mm diameter, however it is not expected that such a small iris diameter would ever be required.

With the iris wide open, a large amount of light would be collected, resulting in a brighter image. However, using a large fraction of the lenses increases spherical aberrations in the focused image, decreasing the imaging resolution. Since the lenses are spherical lenses, instead of the ideal parabolic shape, the farther from the center of the lens that the light hits, the larger the focusing error. As will be discussed in Section 6.2, this is most significant in the ELBT optics configuration as it requires the most extreme focusing.

When the iris diameter is closed down, the imaging resolution is increased at the expense of collecting less light. The amount of light allowed to pass through the iris decreases approximately with the square of the iris diameter. By decreasing the iris diameter by half, the image intensity is decreased to approximately one fourth. The image intensity may also be adjusted through the exposure time of the camera.

The iris is mounted directly in front of the lenses and is attached to the lens holder as shown in Figure 3.4. The iris diameter is controlled remotely with the stepper motor.

Camera

A CCD camera, the Allied Vision Technologies (AVT) Manta model G-046B, is used to acquire the images, the specifications of which are listed in Table 3.2 [35, 36]. The advantages of CCD cameras are that they are generally much more sensitive than other imaging technologies such as Charge Insertion Device (CID) cameras, and are relatively cheap. Camera cost is an important consideration as there will be approximately 14 View Screens required, some with cameras that will require periodic replacement. CCD cameras are also generally simpler to use and to readout images as they do not require Frame Grabber hardware and can communicate directly with a computer through Ethernet or FireWire connections. Unfortunately, CCD sensors are more sensitive to radiation damage, and require local radiation shielding to extend camera life.

Feature	Specification
CCD sensor	Sony ICX 415
Resolution	780 × 580 pixels
Pixel Size	8.3 × 8.3 μm
CCD Size	6.4 × 4.8 mm (1/2” sensor format)
Full Well Capacity	15 000 electrons
Exposure Time	26 μs - 60 s
Maximum Frame Rate	60 Hz
Trigger	External or Software
Camera Interface	Gigabit Ethernet (GigE Vision)
Maximum Power Input	3.6 W

Table 3.2: AVT Manta, G-046 camera specifications.

The camera is capable of receiving image acquisition triggers either through software commands or through external triggers. External triggering allows for synchronization of image acquisition with the beam pulses. This can be very useful in low duty factor imaging or to avoid imaging the transient response of a beam pulse. The external trigger input accepts TTL logic signals, and can be accessed from either of two input pins located on the camera 12-pin Input/Output connector.

Output signals from the camera may be used to indicate performance of different processes within the camera [35]. These signals may provide useful information in diagnosing faulty cameras and can also be accessed through the camera's Input/Output connector.

The CCD cameras are expected to undergo degradation over time as radiation effects cause damage to the camera's CCD sensor and electronics. Damages are incurred through either ionizing or non-ionizing processes. Ionization damage occurs from the creation of electron-hole pairs along the particles track through the material. The process is generally very fast and the main consequence of the ionizing radiation is changes the bias voltage of the CCD sensor and an increase in dark noise.

The non-ionizing processes most importantly cause displacement damages to the semiconductor lattice. Neutrons passing though the CCD may collide with atoms in the lattice, knocking them from their positions and causing vacancies and interstitial defects. These displacement damages are generally quite unstable and can move throughout the lattice, leading to either the recovery of the defects or the formation of more stable ones [37].

The main effect of radiation damage is expected to cause changes in the gain of the individual pixels and increase dark currents in the sensor. This will decrease the well capacity and the signal to noise ratio of the camera. The cameras are meant to be an expendable item, to be replaced when degradation of image quality demands it, but should last for at least one year of usage.

Although the effects are somewhat dependent on the camera design, previous studies have shown that after approximately 10 to 20 Gy of irradiation, the level of damage in CCD cameras make them unsuitable for use [37, 38], however, this will depend of the characteristics of the specific camera. Under the expected radiation levels, the cameras should be able to operate for longer than one year before reaching this level of exposure, and even longer in the ELBT where the radiation is minimal.

Focusing of the cameras is to be done manually during their installation. After all the elements are fixed in place and the mirror orientation adjusted to center the image onto the camera's CCD sensor, the camera can then be focused. With the calibration target in place and the camera connected to a computer within view of the person performing the focusing, the focusing knob is rotated, moving the camera back and forth, until the size of the calibration target markings are clearest and smallest across the entire field of view. The camera is then locked into this position with a set screw to hold the camera rigidly in place.

3.1.4 Optics Layout

The different field of view and image resolutions required in the ELBT and EMBT/EHBT are achieved through different optics configurations. This involves the use of different focal length lenses and different spacings between the lenses and camera. The selection and positioning of the lenses was optimized through the use of a ray tracing simulation, Section 5.3, to maximize both light collection and resolution.

The positioning of the optical elements are defined by three distances, d_1 refers to the separation between the center of the beam target and the first surface of the first lens that the light reaches. d_2 is the spacing between the front face of the first lens to the front face of the second lens, and d_3 is distance from the front face of the second lens to the center of the camera's CCD sensor. These values are given in Table 3.3 along with the lens focal lengths (FL) for both optics layouts.

	First Lens	Second Lens	d_1, mm	d_2, mm	d_3, mm
ELBT	300 mm FL	75 mm FL	534	20	78
EMBT / EHBT	500 mm FL	150 mm FL	558	16	152

Table 3.3: Spacing of the lenses and camera in the two optics configurations.

In order for the image to be in focus across the entire field of view, the camera is mounted at an angle to offset the 45° angle of the beam targets, which results in one side of the targets being located closer to the imaging optics than the opposite side. Light emitted from points closer to the lenses will be focused at shorter distances than light emitted from points which are further from the lenses. The image plane is therefore rotated with respect to the imaging optics, at an angle referred to as the *Scheimflug angle*, Figure 3.5. For the ELBT optics, this angle is 7.0° as measured from the vertical orientation, and in the EMBT and EHBT View Screens, 14.5°.

3.1.5 Calibration Light Source

Illumination for the calibration targets will be provided from a light source located either in front of or behind the targets. Back illumination would involve light emitted

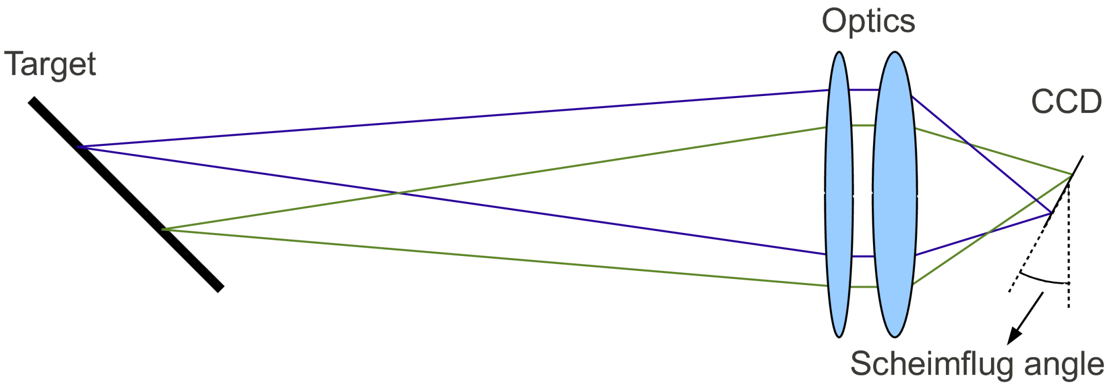

Figure 3.5: The plane of focus is rotated by an angle, the Scheimflug angle, when imaging an object in a plane rotated with respect to the imaging optics.

from a port in the diagnostics cross directly opposite the camera. The light would shine through the holes in the calibration target to be imaged by the imaging optics. By retracting the target holder completely, the light source would become visible to the camera, provided a method for diagnosing radiation damaged pixels, discussed further in Section 4.1.

A front light design would shine light from in front of the target holder, onto the front face of the calibration target. Light would reflect off the calibration target to be imaged by the imaging optics. The calibration markings would be visible as dark spots on the image where the light was not reflected at the locations of the holes on the calibration target.

Illumination of the entire field of view from a front facing light source is difficult due to geometrical constraints. In the current design, light will directly shine on only a portion of the calibration target. Illumination of the rest of the target relies on reflections of light from surfaces within the diagnostics cross. This may lead to an issue of image contrast, where areas lit with direct illumination will be too bright to image at the same times as the dimmer surroundings, requiring the use of multiple images to calibrate the entire field of view.

An alternative solution is to modify the light source to include a small reflective surface that the light source would impinge upon. In this design, any light illuminating the calibration target surface would be reflected light, such that calibration markings across the entire field of view would be visible with a single image.

In the ELBT, where space in the diagnostics cross is limited due to the large number of diagnostics devices required, the port opposite the camera will not always be available for use as a back light. In these cases, the front light will be used. Radiation damage is expected to be low here, reducing the need for a back-light. The mounting locations of the front and back-lights in the ELBT diagnostics cross are shown in Figure 3.1. At higher energies, there is less competition for ports in the diagnostics cross and the back-light solution should always be available.

3.1.6 Support Structure and Shielding

The camera box shields the camera from outside light and keeps the optical surfaces free of dust. The camera, lenses, and mirror are fastened to the inside of the box, providing the fixed alignment and spacing of the elements as described in the previous sections. The lens holder and camera are mounted onto the front inside face of the box with the central vertical optics axis located 50 mm from the wall.

The light enters the camera box through the light tube which bridges the gap between the box and the view-port in the diagnostics cross. The light tube has an inside diameter 52.5 mm such that it will not interfere with the light that will enter the imaging optics and is constructed out of black anodized aluminum to minimize internal reflections along the tube. The light tube is also constructed such that it blocks out any outside light from interfering with imaging.

Power and data connections for the camera and iris control are fed into the camera box through bulkhead feedthrough connectors located on the top of the box. An ethernet port on the outside of the box provides access to the camera data. Four BNC connections are available for the camera trigger inputs and diagnostics outputs. Power for the camera and for the iris control are fed into the box through a single multi-pin circular connector. There are several empty pins available on this connector for future unforeseen usage.

In the ELBT beam-line, the diagnostics box is mounted on a support frame which rolls on a rails to assist with beam-line assembly and alignment. The View Screen camera box is mounted directly to the diagnostics box so that it moves along with it, eliminating the need to refocus the camera if the diagnostics box is moved.

Due to the lower levels of radiation in the ELBT, little shielding is required to protect the camera and lenses. Approximately 16 kg of lead will be mounted around the faces of camera box. The light weight of the camera box allows the box to be supported solely by the light tube, as shown in Figure 3.6.

The camera box and light tube will be removed during the bake-out procedure to

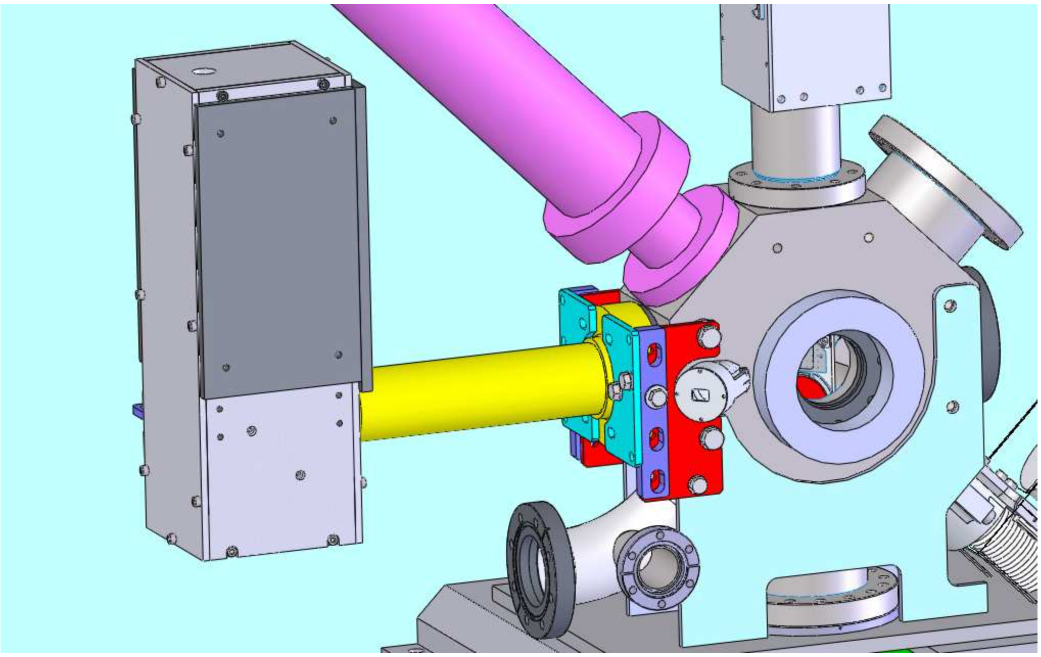

Figure 3.6: The ELBT camera box supported entirely by the light tube. An adapter plate on the diagnostics box viewport allows for the removal and reinstallation of the camera box to the same position and alignment.

avoid damage. This is the process where the entire beam-line, while under vacuum, is heated to a temperature of ∼ 200°C to remove any moisture brought in by the air. The accelerator beam-line must be baked-out whenever it has been brought up from vacuum. The light tube mounts over the view-port window with an adjustable adapter plate that allows for alignment of the box. There is an additional set of screws and dowel pins that allow the camera box to be removed during bake-out without affecting the mounting position and camera focus when re-installed.

In the EMBT and EHBT, space is not so constrained and the beam-line will not be undergoing frequent repositioning. This allows the View Screen to be mounted directly to the floor, providing the support required to hold up the weight of the several centimeters of lead and polyethylene shielding required.

The outside faces of the camera boxes are lined with lead and polyethylene panels to protect the lenses and camera from the damaging radiation emitted from the beam-line and beam dumps. This radiation is primarily in the form of bremsstrahlung photons (X– and γ–rays) emitted when the beam is accelerated, and from scattering of the beam off residual atoms in the beam-line, targets, and the beam dumps. The most damaging radiation for the cameras will be the neutrons generated in the latter processes [37].

The most extreme radiation environment expected near the e-linac beam-line is 10 mSv/hr, however the radiation will be much lower than this in the low energy sections of the the beam line and far away from beam dumps and target stations. To convert from the unit *sievert*, which is generally used to describe the amount of radiation absorbed in biological tissues, to the *gray*, which describes the amount absorbed by a material, a weighting factor, W, is used based on the properties of the radiation, such as the type and energy.

$$1\,\mathrm{Gy} = (1\,\mathrm{Sv})\,/W \tag{3.1}$$

The radiation emitted from the beam-line will be mainly photons and electrons ($W = 1$) and neutrons ($W = 5$ to 20, depending on energy). Therefore, taking an approximate value of $W = 5$ for the sake of estimating the radiation damage of the camera, 10 mSv/hr translates to 2 mGy/hr. At this rate, it would take approximately 5000 hours, or 200 days, of continuous irradiation without any shielding to reach 10 Gy. Placing the camera behind several centimeters of polyethylene and lead will extend this lifetime even further.

Polyethylene is an efficient neutron absorber, while the lead is used to stop photons and electrons. The lead shielding is placed behind the polyethylene as to reduce any additional radiation caused by the neutrons striking the polyethylene. Additional shielding may be incorporated as required based on localized radiation measurements.

Chapter 4

Image Correction and Calibration

Upon acquisition, images must go through a series of image calibration and correction procedures. The purpose of these procedures are to:

- Perform a pixel-by-pixel intensity calibration to correct for pixel to pixel variability and changes due to radiation damage,
- Convert image coordinates to positional coordinates in the plane transverse to the beam,
- Correct for geometric distortions in the images due to the 45° orientation of the beam targets and other optical effects,
- For scintillation targets operating under high beam currents, adjust the pixel intensity to account for temperature dependent light yield, and
- Adjust pixel intensity to account for the position dependency of the optics to collect light emitted from different locations on the beam targets.

4.1 Radiation Damage Calibration

The main effect of the radiation damage on the cameras is to decrease the gain and signal to noise ratio of individual pixels. By acquiring images of a known light distribution, the damage can be characterized and partially corrected for.

The light distribution to be imaged comes from the back-light used to illuminate the calibration target. With the target holder completely retracted and the back-light on, the camera will see an unobstructed view of the light distribution of the back-light. In the EMBT and EHBT, the light will cover the entire 25 mm field of view of the camera. In the ELBT, the geometry of the diagnostics cross is such that the back-light can only cover approximately 40 mm of the 50 mm field of view in the vertical image axis. Therefore in the ELBT, an assessment of the radiation damage is only possible on part of the camera's CCD. However, the radiation damage here is expected to be minimal and the light will cover the portion of the field of view that will most often contain the beam.

In order to diagnose radiation damaged pixels, images are acquired of the light source, which can then be compared to a reference image acquired when the camera was installed, before it has been affected by the radiation. The light source was designed to be as uniform as possible but still exhibits a difference in intensity of several percent across the field of view.

Images should be taken at several light intensities to fully characterize pixel damage. Pixels with large deviations from the reference images can be adjusted in future images to correct for pixel damage. Analyzing a series of images acquired at the same intensity will provide a measure of the signal to noise ratio for individual pixels.

4.2 Geometric Calibration

A geometric calibration performs two functions. Firstly, it translates image coordinates into their corresponding positional coordinates in transverse beam space, and secondly, it corrects geometric distortions.

As acquired from the camera, raw images will have a slight geometric distortion across the field of view. Since the targets are placed at a 45° angle to the beam-line, one edge of the target will be closer to the lenses and camera then the other. The camera is mounted on an angle so that the entire image is in focus, however this still causes a slight difference in the magnification in one side of the image compared to the other. The effect of this is that the image will appear slightly more compressed on one side.

By acquiring an image of the calibration target, lit either from the front or the back, the locations of the target markings can be used to convert the image to positional coordinates. With a front-light shining on the target, the holes will show up as dark spots on a light image, and with back-lighting, the opposite case; bright holes on a dark background. In either situation, an algorithm will be employed to map the coordinates of the centroids of calibration markings.

The transformation from image coordinates to positional coordinates is performed through a transformation map generated using the method of polynomial warping [39]. The set of calibration pixel coordinates, known in both the raw camera images and in real space, acquired by imaging the calibration target is used to create polynomial functions which calculate the transformation from positional coordinates to image coordinates.

The pixel coordinates in the raw camera images, $\{u_x, u_y\}$, corresponding to any point in positional space, $\{x, y\}$, can be calculated through the power series expansions:

$$u_x = \sum_{i,j=0}^{N} K_{ij}^{(1)} x^i y^j \tag{4.1}$$

$$u_y = \sum_{i,j=0}^{N} K_{ij}^{(2)} x^i y^j \tag{4.2}$$

where the coefficients $K_{ij}^{(1)}$ and $K_{ij}^{(2)}$ can be determined through the Least Squares minimization of the sum of the squared differences between the known coordinates in the raw camera images, $\{u_{x_k}, u_{y_k}\}$, and the coordinates calculated through Equations 4.1 and 4.2 using their corresponding coordinates in positional space, $\{x_k, y_k\}$. The index k runs from 1 to m, where m is the number of markings on the calibration targets. The number of unknown coefficients to be determined in this manner is $(N + 1)^2$, where N is the order of the power series expansion.

For each coordinate in position space, $\{x, y\}$, Equations 4.1 and 4.2 are used to calculate the corresponding image coordinates, $\{u_x, u_y\}$. The resulting transformation map is composed of the list of image coordinates corresponding to each position in beam space across the field of view. As the images are acquired by the camera, this transformation map is used to convert the images into undistorted images in beam space coordinates. Since the calculated image coordinates will be non-integer valued, the gray-scale value of the transformed pixel is determined through the bilinear interpolation of the gray-scale values of the four surrounding pixels.

4.3 Thermal Correction

The decrease in light yield of the scintillation targets with temperature may be partially corrected for by applying an appropriate correction map. Through the use of simulations to model the deposition of energy within the scintillating targets and the resulting temperature rise, a theoretical correction map may be determined to adjust the intensity appropriately. These simulations are described in more detail in the following chapter.

The accuracy of such a correction factor depends strongly on the relevancy of the corresponding simulation studies and the temperature dependence of the light yield of YAG:Ce, as reported in [24]. The full temperature dependence of the light yield of YAG:Ce is shown in Figure 4.1.

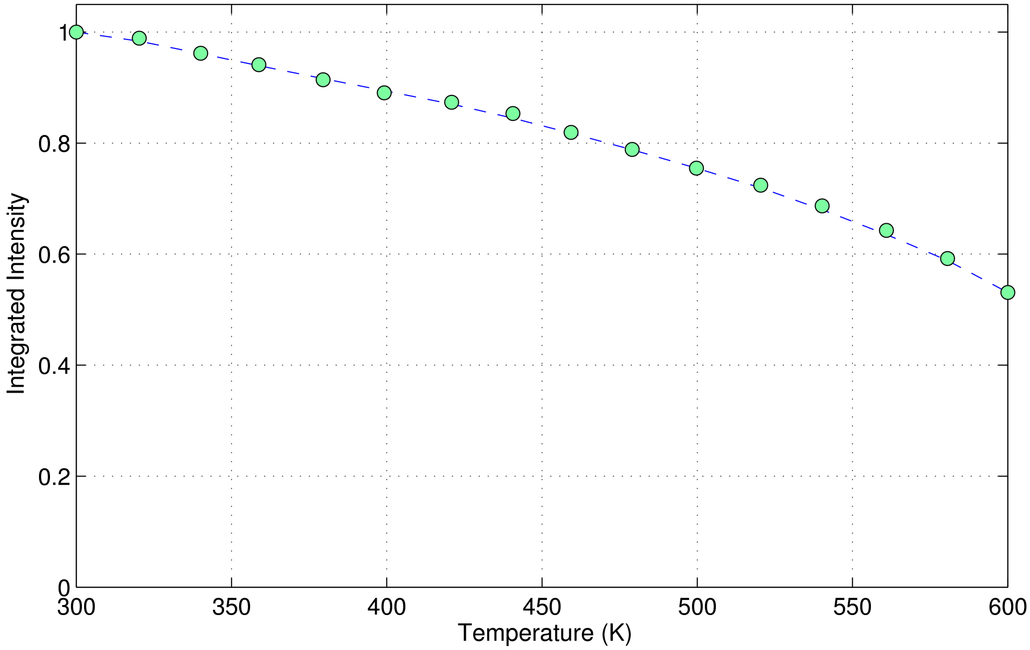

Figure 4.1: The temperature dependence of the total light output of YAG:Ce, doped with 0.33% Ce^{3+} and excited by light at a wavelength of 480 nm.

It is desirable to keep the applied correction factor minimal by operating under the lowest beam currents possible. At beam currents under 5 μA, the 0.5 mm thick ELBT YAG:Ce targets will stay below 100°C for nominal beam sizes, requiring less than a 10% correction factor on the hottest areas of the target.

4.4 Light Collection Efficiency Calibration

The amount of light collected by the imaging optics, referred to here as the light collection efficiency, differs for light emitted from different locations across the beam targets, causing some areas of the targets to appear artificially brighter than others.

This effect is present for both the isotropic emission distribution of the scintillation screens, where light is emitted in all directions uniformly, and the emission of OTR light, although the effect is much more apparent for OTR emission.

The optics system covers a slightly larger solid angle for points on the closer edge of the target than for the farther points. For isotropic emission, this results in a maximum difference of ∼12% or ∼6% in the light collection efficiency across the field of view in the ELBT optics and EMBT/EHBT optics respectively, as shown in Figure 4.2. Without calibrating the image to correct for this difference, would cause a $24\,\mu$m bias in beam center location for a nominal beam size in the ELBT, and a $10\,\mu$m bias error in the EMBT/EHBT for a 2 mm beam.

A correction map is created for the light collection efficiency for the isotropic emission distribution by calculating the solid angle subtended by the iris aperture as a function of target position and iris diameter.

The light emitted from the OTR beam targets is emitted with an angular distribution described by Equations 2.2 and 2.3, and shown in Figure 2.4. The light is directed in two lobes on either side of the reflection axis of the beam target and depending on the location of the the emission of light from the OTR target, varying amounts of light will be collected by the optics.

A correction map can be calculated from the theoretical OTR emission distribution to correct for the differing light collection efficiencies across the OTR target. The collection efficiency is shown for 10 MeV OTR light across the foil in the x and y directions in Figure 4.3. For 30 and 50 MeV OTR emission, the maximal light collection is achieved at the center of the target, as the light is more sharply peaked towards the reflection axis.

When imaging the OTR light distribution, it is most desirable to operate with the optics aperture as wide as possible to decrease the dependency on the applied correction factor. From Figure 4.3, for 10 MeV OTR emission with the iris opened to 41 mm, there is an approximately 25% difference in intensity of the light collected from the center of the foil to light from the edge of the field of view. With the iris closed to 30 mm, this difference increases to approximately 75%.

Applying a correction map also requires a tight angular tolerance on the mounting angle of the beam targets. If the angle used to generate the correction map is not the same as the angle the OTR target is actually mounted at, an error will be introduced, biasing the image to one side or the other.

The error on the computed beam center with the beam target mounting angle

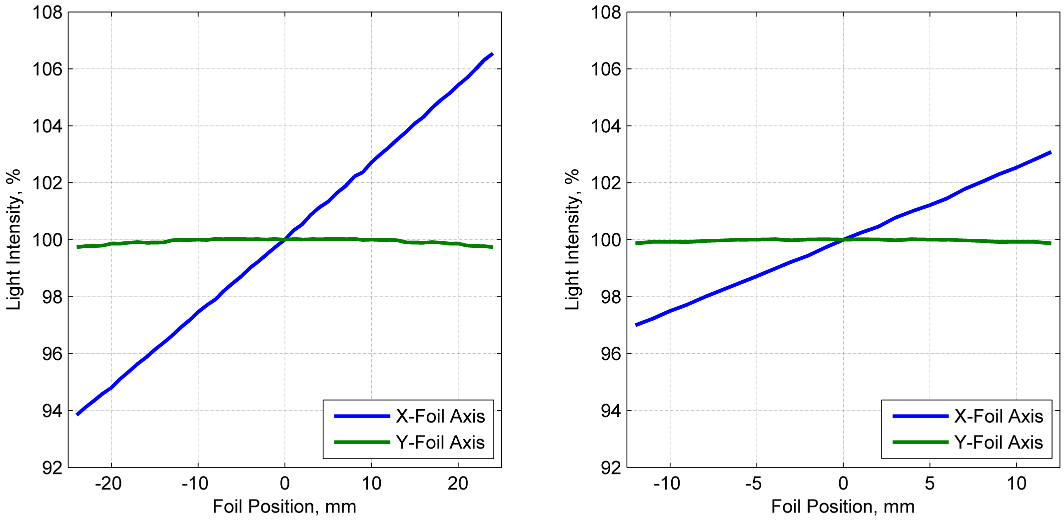

(a) ELBT optics (b) EHBT optics

Figure 4.2: The light collection efficiency for points across the scintillation beam targets in the x and y axes.

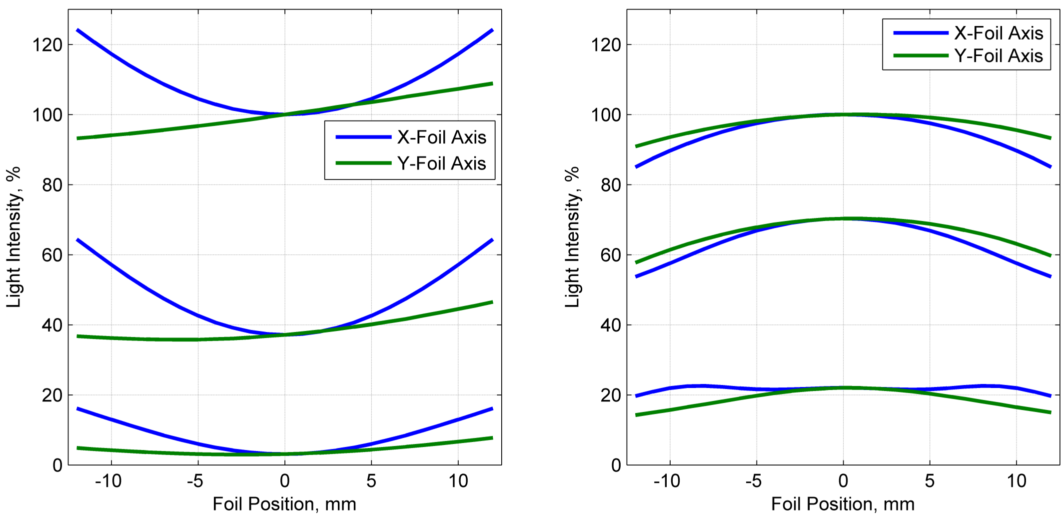

(a) 10 MeV OTR (b) 50 MeV OTR

Figure 4.3: The light collection efficiency for points across the OTR beam target in the x and y axes, with a 41 mm iris aperture (top), 30 mm iris (middle), and 15 mm iris (bottom).

varied from 44.7° to 46° is shown in Figure 4.4 for 10 MeV and 50 MeV OTR distributions and a 2 mm Gaussian beam. With the iris aperture at 41 mm, the tolerance on mounting angle is quite loose, with the error on the reconstructed beam position approaching the 0.2 mm requirement on absolute uncertainty at approximately 0.7° offset for 50 MeV OTR and much later at 10 MeV. With a small iris diameter the tolerance is much tighter, with the error in the beam center location reaching 0.2 mm with only a 0.1° offset for 10 MeV OTR, or 0.2° at 50 MeV. This effect is stronger for wider beams that cover a larger area of the foils.

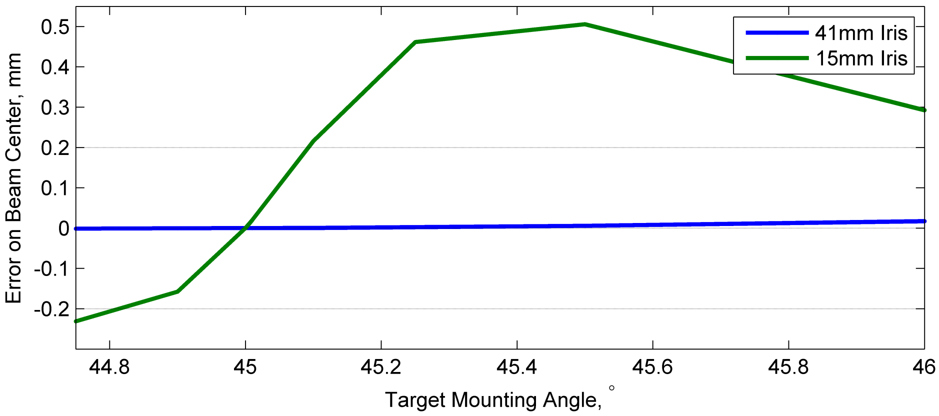

(a) 10 MeV OTR

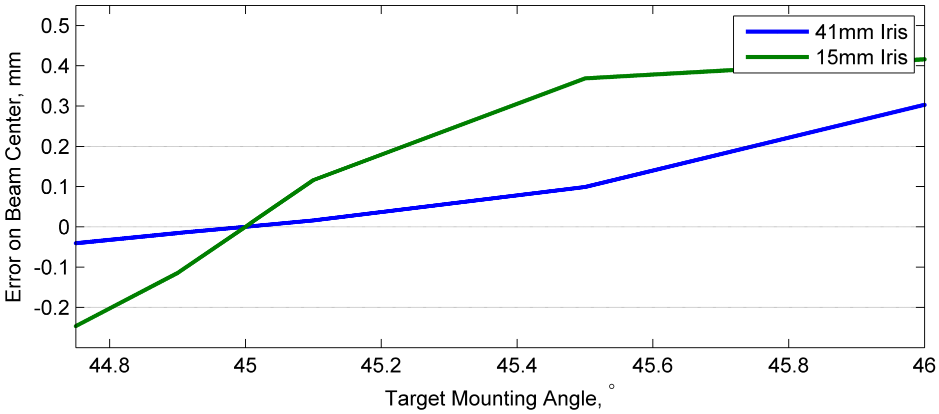

(b) 50 MeV OTR

Figure 4.4: The errors incurred from the OTR light collection calibration with the mounting angle offset from 45° for a 2 mm Gaussian beam.

The theoretical OTR emission distribution depends strongly on the properties of the foil material, such as the relative permittivity. Since the correction maps are calculated based on the theoretical distribution, it is beneficial to verify the accuracy of the calculated correction factor. Providing that the beam spot characteristics are sufficiently stable, the profile can be imaged with varying iris diameters, comparing the resulting images to simulated images produced from the theoretical OTR distribution. Provided that the parameters of the theoretical OTR distribution are correct, the measured beam properties should be reproducible with any iris diameter.

Alternatively, by changing the location of the camera such that it focuses at infinity rather than the target surface, then if the beam-size is sufficiently small, the camera will image the OTR point spread function, providing a more detailed image of the angular emission distribution rather than the spatial distribution of electrons [40]. The use of linear polarizing filters would separate the vertical and horizontal polarization components leading to further verification of Equations 2.2 and 2.3. This is a more extreme approach that would require reconfiguration of the imaging optics.

4.5 Summary of the Image Processing Procedures

Upon acquisition, the images go through the series of post processing routines. If damage to the camera requires it, the radiation damage correction map is first applied to the the image. After this, the image goes through an algorithm to perform both the geometric and light intensity corrections for temperature dependence and light collection efficiency. The image would then proceed to be analysed for beam properties, such as beam width and center, and displayed to the Control Room console.

The steps of this calibration are shown in Figure 4.5 for an image simulated with the optics ray tracing simulation for a 4 mm Gaussian beam distribution of 10 MeV electrons on the pyrolytic graphite target with an iris of 5 mm aperture. This example image is shown under extremely exaggerated conditions to show clearly the effect of the calibration procedures. Under normal conditions, the iris would never be used with such a small diameter and the calibration would have an almost unnoticeable effect to the naked eye.

The first image shows the raw image as it would be acquired from the CCD of the distorted beam profile. The second image is after the geometric calibration, converting from image coordinates to beam coordinates. The final image shows the undistorted beam profile, after applying light intensity calibrations, restoring the 4 mm Gaussian profile.

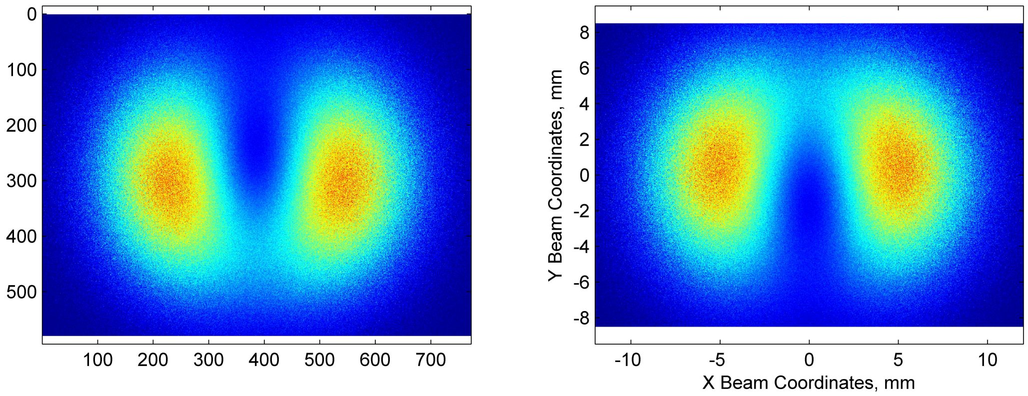

(a) Raw CCD image

(b) Geometry Corrected

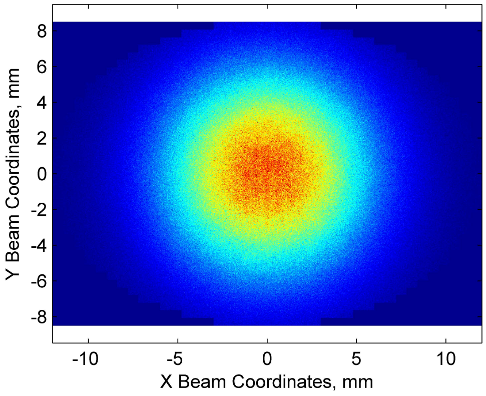

(c) Light intensity corrected

Figure 4.5: The steps of the image post processing procedures to implement the calibration and correction procedures for a simulated image of a 10 MeV, 4 mm Gaussian beam with an OTR beam target and 5 mm iris diameter.

Chapter 5

Simulation Studies

Simulation studies provide a means for characterizing a large number of different design configurations that would not otherwise be possible to test. Studies have been performed to select the optimal beam target materials for scintillation and OTR targets through energy loss and scattering considerations and the subsequent thermal response. The imaging optics have been designed through the selection of lenses and placement of optical elements that optimize both the imaging resolution and light collection.

Simulations provide the operational range of the different beam targets and the visibility of the beam profiles with the View Screen under different conditions. Additionally, simulation studies are required to produce thermal correction maps and to test image processing procedures before the final system is constructed and installed.

This chapter provides a description of the simulation studies performed and the results obtained through them.

5.1 GEANT Simulations of the Beam Targets

A GEANT4 simulation was written to study the energy losses occurring for electrons passing through various scintillation and OTR beam targets. The simulation work focused on the energy losses by the beam electrons, the energy deposited within the targets, and the scattering distribution of the emerging beam.

Studies were performed on several different potential beam targets; Chromox, YAG:Ce, or LYSO:Ce scintillating targets, and Pyrolytic Graphite or Titanium OTR targets, mounted at 45° to the beam axis. The beam was assumed to be composed of electrons with zero energy and angular spread. Electron beam energies of 300 keV, 10 MeV, 30 MeV, and 50 MeV were included in this study.

As electrons pass through the beam targets, they lose energy through ionization and excitation of the media, and the emission of bremsstrahlung photons. A portion of this energy loss is deposited in the target with the rest leaving the target carried by scattered electrons, and bremsstrahlung photons. The energy deposited in the targets contributes to heating and in the scintillation targets, the emission of scintillation photons, although this represents a small fraction of the total energy deposited.

The electrons undergo multiple scatters while traversing the beam targets and exit scattered at an angle with respect to the beam axis. The particle flux, as a function of scattering angle, approximately follows a Gaussian distribution with a large number of particles scattered at low scattering angles.

The results presented here were determined using 10^5 events in each scenario studied. Each event comprised of a single beam electron passing through the beam target material, along with any subsequent electrons or photons scattered or produced in the process.

Results

The average total energy loss per electron by the primary electrons as they traverse the beam targets in the GEANT4 simulation closely follows a Landau distribution, as shown in Figure 5.1. The Landau distribution is generally used to describe the energy losses of charged particles traversing a thin layer of material [41], such as a beam target. The energy spread of the electron beam after the foil can be characterized by the width of the Landau distribution, σ, which has been determined to be equal to approximately one quarter the FWHM.

For electrons at 300 keV, only the scintillation screen is required as the energy is too low to employ the OTR technique. At this energy, almost the entire electron beam is stopped completely by the screens, with a small fraction of the electrons being deflected backwards. Most of the electrons are stopped within the first 100 μm of the beam target and almost no electrons make it through a 200 μm target. The average energy deposited within a 0.5 mm YAG:Ce target is approximately 237 keV per electron at 300 keV, with the remaining energy carried away by the back-scattered electrons. Other materials will also result in similar energy deposition since most of the electrons are stopped quickly at this energy.

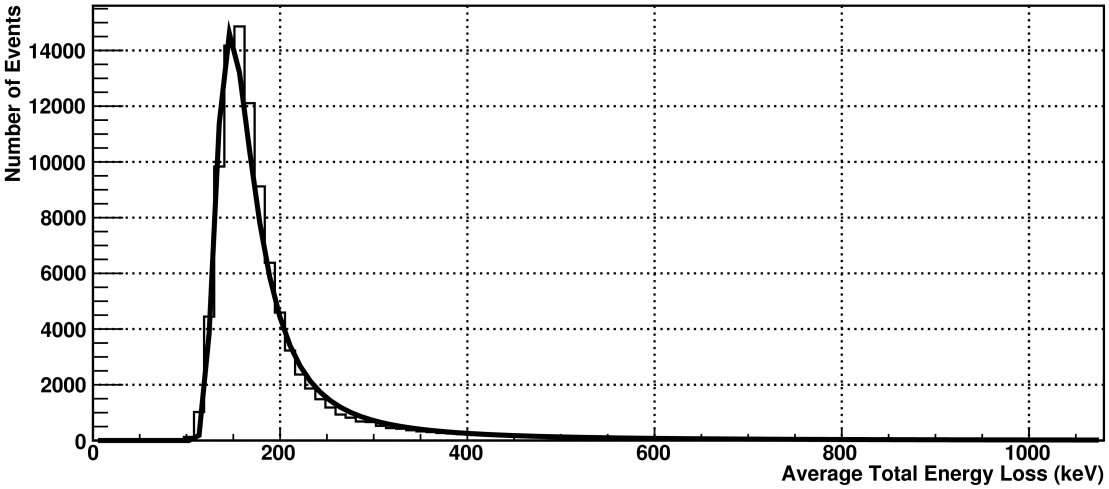

Figure 5.1: The distribution of total energy loss per electron for 10 MeV electrons after traversing a 0.2 mm YAG:Ce screen, fit with a Landau distribution.

At the higher beam energies, 10, 30 and 50 MeV, the electrons have enough energy to pass through the entire thickness of the beam targets. At these energies, either the scintillation target or the OTR target may be used. The total energy loss, energy deposited, and energy exiting the target as photons, all given as an average per beam electron, and the energy spread are listed in Table 5.1.

As the electron beam is highly relativistic at these energies, the ionization energy losses, and therefore the energy deposited in the beam targets, is approximately the same for a given beam target across the range of beam energies. Therefore the thermal heating of the beam targets is fairly independent of beam energy. The energy loss through bremsstrahlung photons does however depend strongly on the beam energy resulting in different total energy losses at different beam energies.

The distribution of the average total energy loss per electron is shown as the fraction of electrons with average total energy loss greater than a given energy, as shown in Figure 5.2. This shows the fraction of electrons that fall outside of a given longitudinal acceptance after passing through the beam targets.

The angular distribution of the emerging electron beam can also be represented in a similar way, as the fraction of electrons scattered outside of a given scattering angle, as shown in Figure 5.3. This provides a measure of the number of electrons that cannot be captured by the quadrapole focusing magnets of the e-linac and collide with the downstream beam pipe wall.

		0.2 mm YAG:Ce	0.2 mm LYSO:Ce	10 μm Graphite	5 μm Titanium
300 keV					
Average energy deposited	(keV)	236.5	191.0	- - -	- - -
10 MeV					
Total average energy lost	(keV)	262.7	473.8	6.14	6.55
Average energy deposited	(keV)	188.9	273.7	5.04	4.50
Energy exiting as photons	(keV)	58.7	189.1	0.37	1.34
Energy spread, σ	(keV)	13.7	23.1	0.44	0.40
30 MeV					
Total average energy lost	(keV)	402.5	835.1	8.17	9.72
Average energy deposited	(keV)	189.5	266.1	5.03	4.55
Energy exiting as photons	(keV)	187.7	543.5	1.87	4.18
Energy spread, σ	(keV)	13.5	19.6	0.44	0.41
50 MeV					
Total average energy lost	(keV)	552.1	1279	8.68	13.6
Average energy deposited	(keV)	190.1	267.0	4.96	4.50
Energy exiting as photons	(keV)	334.7	978.4	2.51	8.33
Energy spread, σ	(keV)	13.5	19.1	0.44	0.40

Table 5.1: Summary of the average energy losses per electron through 0.2 mm YAG:Ce and LYSO:Ce scintillation screens, 10 μm Pyrolytic Graphite, and 5 μm Titanium OTR foils.

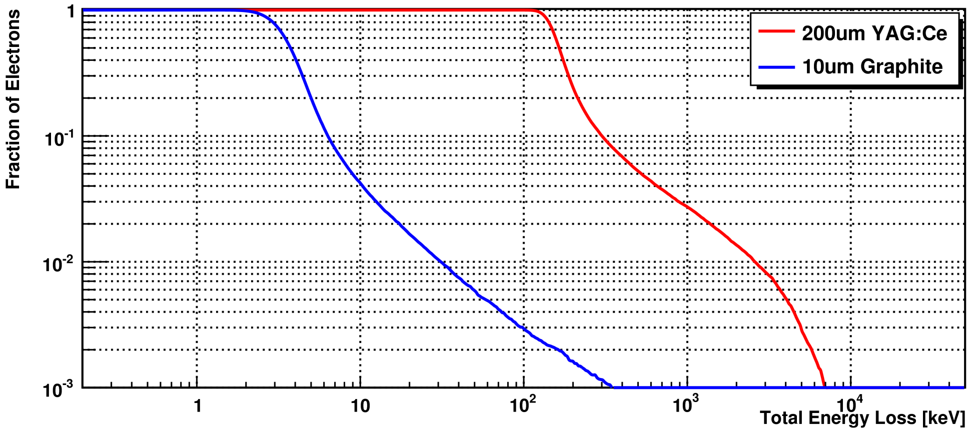

(a) 10 MeV electron beam energy

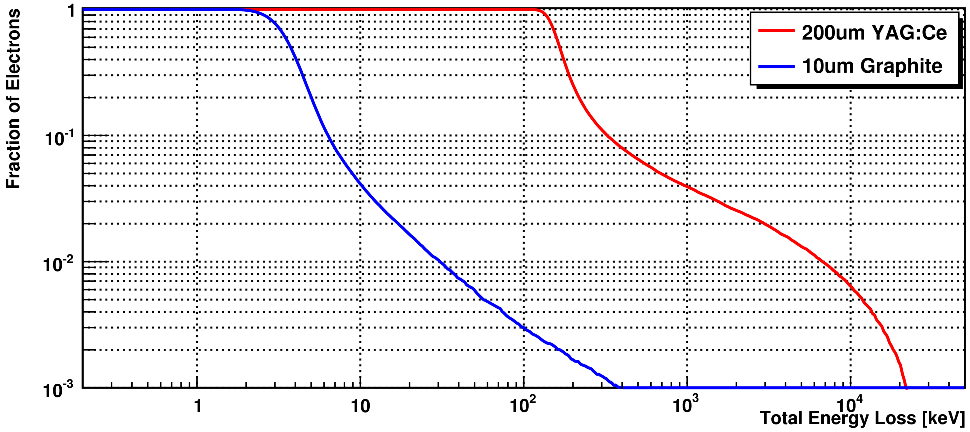

(b) 30 MeV electron beam energy

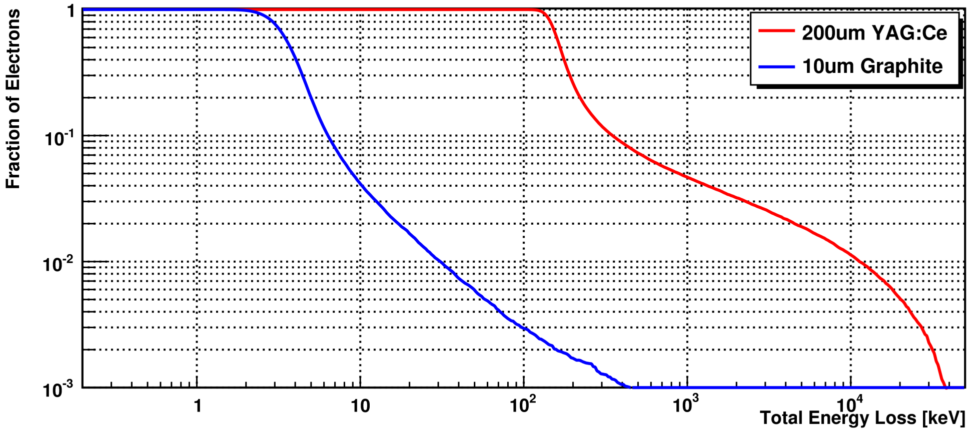

(c) 50 MeV electron beam energy

Figure 5.2: The fraction of electrons with average total energy loss per electron greater than a given energy for YAG:Ce scintillation screens and Pyrolytic Graphite OTR foils.

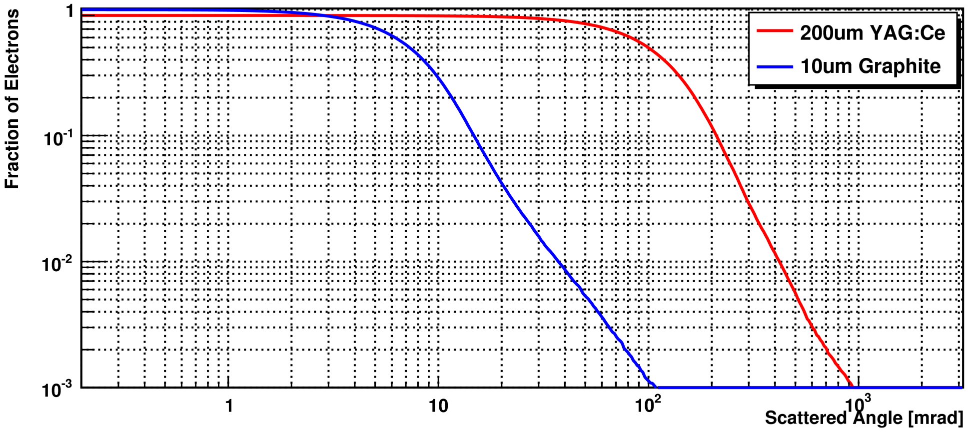

(a) 10 MeV electron beam energy

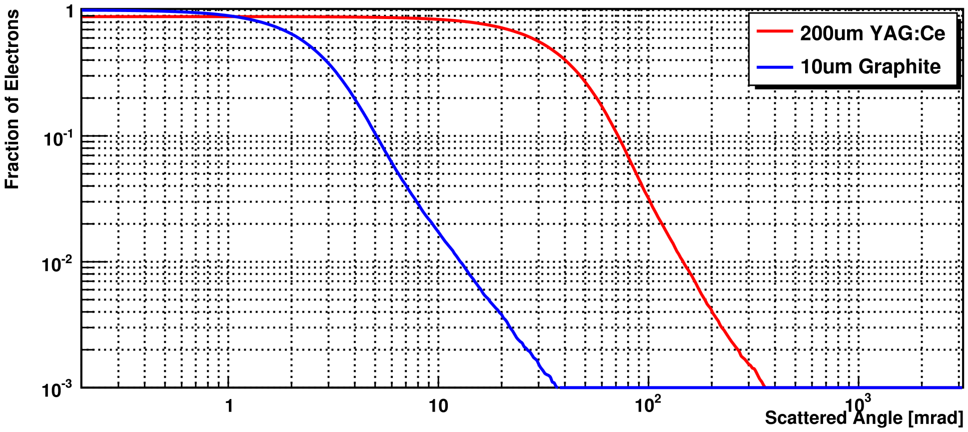

(b) 30 MeV electron beam energy

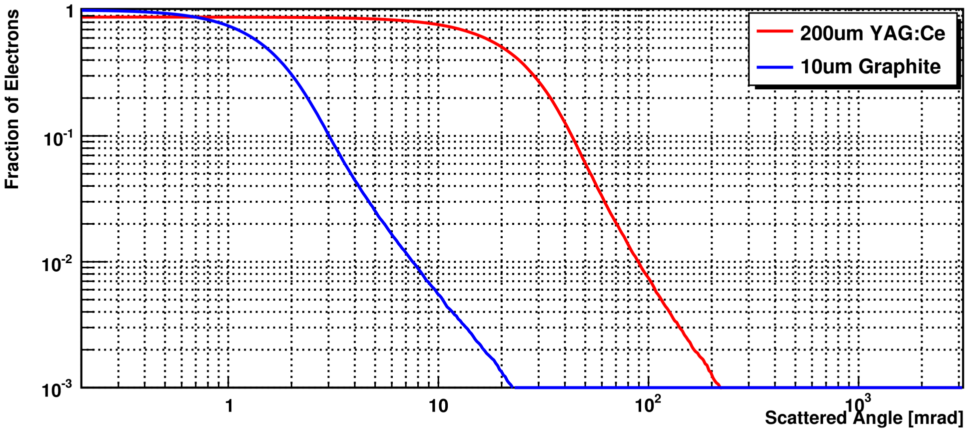

(c) 50 MeV electron beam energy

Figure 5.3: The fraction of electrons scattered outside a given scattering angle for YAG:Ce scintillation screens and Pyrolytic Graphite OTR foils.

Further plots of the distributions of energy loss and scattering angle for LYSO:Ce and Chromox scintillation screens and Titanium OTR foils are included in Appendix A.1

In order to keep the total beam losses less than 2 W through each device, the beam profile monitors are limited to a maximum operating current set by the total energy loss experienced per electron as they traverse a beam target. The total beam losses can be determined by multiplying the average total energy loss per electron, by the number of electrons passing through the foil per second. Table 5.2 summarizes the maximum operating currents for the different beam targets at each profile monitor station.

	0.5 mm YAG:Ce	0.5 mm LYSO:Ce	0.2 mm YAG:Ce	0.2 mm LYSO:Ce	10 μm Graphite	5 μm Titanium
300 keV	6.5 μA	6.5 μA	6.5 μA	6.5 μA	- - -	- - -
10 MeV	- - -	- - -	7.5 μA	4.0 μA	320 μA	300 μA
30 MeV	- - -	- - -	5.0 μA	2.0 μA	240 μA	200 μA
50 MeV	- - -	- - -	3.5 μA	1.5 μA	230 μA	140 μA

Table 5.2: The maximum beam currents to keep the total losses below 2 W for the candidate beam targets.

5.2 Thermal Simulations of the Beam Targets

The effects of target heating were modeled in a COMSOL simulation. COMSOL is a Finite Element Analysis (FEA) tool used to provide numerical simulations of physical processes. The Heat Transfer Module provides tools for analyzing heat transfer through the processes of conduction, convection, and radiation.

In FEA, a spatially complex system is divided up into a number of discrete volume elements that can be more readily analyzed. The process to be studied, in this case the thermal heating of the beam targets, can be expressed through a governing differential equation and a series of boundary conditions. The complete system may be complicated, but through the process of discretization, the system can be divided into many smaller elements, each governed by their own simplified differential equation. The distribution of elements across a structure is called a *mesh* and the individual mesh elements are linked to neighbouring elements through matching boundary conditions.

This process simplifies a system with complicated geometry and loading to a set of interconnected algebraic problems that are individually simple to solve. The complexity of a problem is thus reduced to a question of organization and computing power.

The key to a successful FEA is the implementation of realistic boundary conditions and to ensure the mesh is fine enough to provide a stable and accurate solution. The properties of a system are calculated at the location of each mesh element. A small error in one element can be compounded over the large number of elements across a system, resulting in a meaningless solution. The size of the mesh elements must be chosen in such a way to balance computation power with the stability of the solution. For the following study, this was achieved by decreasing the mesh size for a fixed parameter set until the solution no longer depended on the characteristics of the mesh.

The beam targets are heated as a result of the energy deposited within the targets by the passage of the electron beam. As previously discussed, this interaction was studied through a GEANT4 simulation which provided the average energy deposited by electrons of different energies within the target materials. These values can be found in Table 5.1.

For 300 keV electrons, only the scintillation target can be employed, whereas at higher energies both OTR and scintillation targets may be used. Since the ionization energy loss depends weakly on the particle energy at relativistic beam energies, the average energy deposited within a particular target is approximately constant for a 10 to 50 MeV beam current, requiring only a single thermal simulation to represent beam energies from 10 to 50 MeV.

Several materials were included in this study YAG:Ce, LYSO:Ce and Chromox scintillation screens, and Pyrolytic Graphite and Titanium OTR foils. Above 300 keV, the temperature distribution does not depend strongly on the target thickness. However in the low energy regime where the electron beam is stopped almost entirely by the target, decreasing the target thickness would result in less material, but the same amount of energy deposition leading to higher target temperatures.

Both YAG:Ce and LYSO:Ce have melting temperatures close to 2000°C, although the maximum operating temperature is much lower than this. The light output of these materials decrease with temperature as shown in Figure 4.1, limiting the beam currents they may be operated under.

For the OTR targets, Pyrolytic Graphite is stable up to 2500°C and Titanium has a melting temperature of 1670°C. However at these temperatures, the intensity of blackbody radiation becomes comparable to or greater than the emission of OTR. The relative permittivity also has some temperature dependence.

Thermal Model Assumptions

The thermal response of a volume element of material to an increase in energy of ΔQ depends on the heat capacity of the material, C_p, and the mass of the material δm:

$$\Delta T = \frac{\Delta Q}{\delta m C_p} \tag{5.1}$$

Energy is deposited in the beam targets by the electron beam and therefore follows the same transverse spatial distribution. Thermal energy then spreads across the targets through the process of thermal conduction. The rate of energy flow, $\dot{Q}$, between two points separated by a distance x, with temperatures differing by ΔT, and through a cross sectional area, A, is proportional to k, the thermal conductivity.

$$\dot{Q} = kA\frac{\Delta T}{\Delta x} \tag{5.2}$$

In general the thermal properties of a material are dependent on temperature. For example, while Pyrolytic Graphite has a high thermal conductivity of approximately 345 W/m K at room temperature, at temperatures greater than 2000 K this drops to almost 100 W/m K. Such a large change in material properties must be taken into account while attempting to analyze the thermal response across such a temperature range. If temperature dependent properties are unavailable, then across relatively smaller temperature changes, such as the scintillation beam targets are limited to, the thermal properties may be assumed constant with little loss of accuracy.

The thermal conductivity and heat capacity of Pyroid, a form of Pyrolytic Graphite, is shown for temperatures between 300 K and 2000 K in Figure 5.4. The thermal conductivity is greater in the plane parallel to the target surface than for the perpendicular axis. The density is approximately constant over this range at 2220 kg/m^3 [33].

The temperature dependent properties of YAG:Ce were taken to be equivalent to those of undoped YAG, whose temperature dependent properties are available

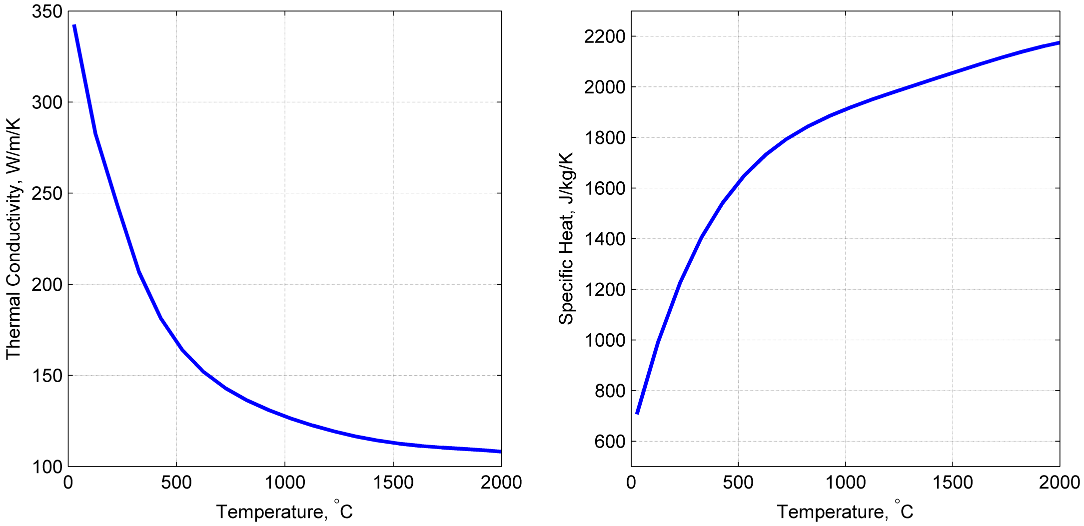

(a) Thermal conductivity across the surface of the target

(b) Heat Capacity

Figure 5.4: The thermal properties of Pyroid as a function of temperature.

within the COMSOL materials library. The thermal properties of LYSO:Ce were only available for a temperature of 300 K [42]. These properties, and the properties of undoped YAG at 300 K are summarized in Table 5.3.

		YAG:Ce	LYSO:Ce
Thermal Conductivity	(W/m K)	10.8	3.6
Heat Capacity	(J/kg K)	590	310
Density	(kg/m^3)	4550	7390

Table 5.3: The thermal properties of YAG:Ce and LYSO:Ce at 300 K.

The following assumptions were applied in the construction of the COMSOL FEA thermal model.

1. The initial temperature of the beam targets and holder is 300 K.
2. The edges of the beam targets are held at a constant temperature of 300 K. This is based on two more fundamental assumptions, mainly that there exists good thermal contact between target and target holder around the edge of the targets to allow for the heat to flow freely between them in a vacuum environment, and

that the target holder is capable of dissipating up to 2 W of thermal energy without a significant rise in temperature.

3. The only mode of thermal transport modeled is the thermal conduction within the beam target itself. As the targets are located in vacuum there will be no medium to provide convective cooling, and even at the maximum operating temperatures, energy losses through radiation are minimal relative to conductive cooling. This emphasizes the importance of achieving an effective thermal contact between target and target holder.

4. The energy deposited within the beam targets is uniform over time. This of course is not truly the case as the electron beam will contain a pulsed time structure which is most apparent when operating at a low duty factor. The results acquired by assuming a uniform time structure correspond to the time averaged temperature distribution of a pulsed beam.

5. The mesh size was decreased until the simulation provided a stable solution and the size of the mesh elements were much less than the width of the beam such that the properties across a single mesh could be assumed approximately constant.

Time Structure Response

To illustrate the effect of the time structure of the electron beam, a single simulation was performed in which the structure was allowed to change with time. In this study, a relativistic 10 mA electron beam operating in 10 μs pulses at 100 Hz corresponds to a duty factor of 0.1% and a time averaged current of 10 μA. The beam was assumed to be circular with a Gaussian distribution and a width of $\sigma = 0.335$ mm.

Under these conditions, the first beam pulse on a 10 μm Pyrolytic Graphite foil would cause an immediate temperature rise of 28.9 K at the location of the beam center, resulting in a maximum foil temperature of 328.9 K. Over the next 0.01 s before the next beam pulse arrives, through thermal conduction, the temperature of the foil would drop to ~301.2 K. After the next pulse, the temperature rises by ~28.9 K again, to 329.9 K, and again, in the next 10 ms, cools to ~301.8 K.

This heating and cooling cycle repeats as is shown in Figure 5.5. Within less than 3 seconds, the temperature distribution reaches a dynamic equilibrium state with the maximum foil temperature oscillating between ~335 K immediately after a beam pulse and cooling to ~307 K between pulses. The time averaged maximum temperature of the foil after reaching this equilibrium state is approximately 310 K.

Using a pulsed beam structure for all of the thermal simulations is not possible as it requires a prohibitively higher computation time. By assuming the energy deposited into the beam targets is uniform over time with the appropriate time average beam current, the calculated temperature distribution is approximately equal to the time average of the pulsed beam temperature distribution. This is shown as the blue line on the plots in Figure 5.5. For the remaining thermal studies, the energy deposition is assumed uniform in time and it must be understood that the peak temperature of the beam targets will actually oscillate above and below the values calculated. The true peak temperature depends both on the pulse length and bunch charge.

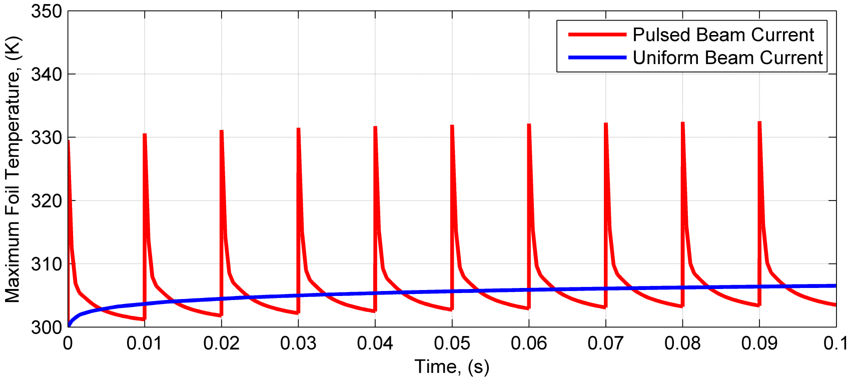

(a) Thermal response for the first 100 ms of beam.

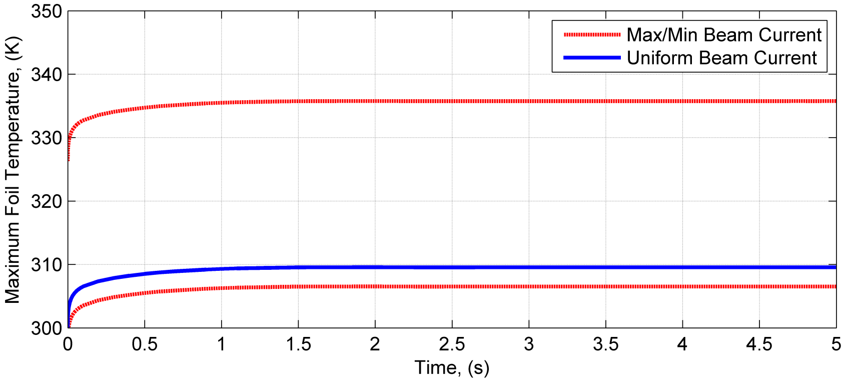

(b) Thermal response for the first 5 s of beam. The red lines represent the extremes of the thermal response to the pulsed beam structure, with the temperature oscillating between them.

Figure 5.5: The maximum temperature of a Pyrolytic Graphite foil in a 0.1% duty factor electron beam, showing the thermal response to both the pulsed beam structure and the time averaged beam current.

Results

LYSO:Ce has a very low thermal conductivity, only ∼3 W/m K, compared to YAG:Ce. Heat flows more slowly through a LYSO:Ce target and therefore the temperature builds up higher than in a YAG:Ce target. In the ELBT, a 0.5 mm YAG:Ce screen would reach a temperature of 100°C at a beam current of 5 μA for a nominal beam size. A LYSO:Ce screen screen would reach this same temperature much quicker, at a beam current of only 2 μA.

The peak time-averaged temperature that a YAG:Ce screen will reach as a function of beam current and beam size in the ELBT is shown in Figure 5.6. For nominal beams sizes, the maximum temperature reached by the YAG:Ce screen is ∼130°C. Smaller beam sizes heat the screen to higher temperatures, leading to a higher loss in light output due to the temperature dependant light yeild.

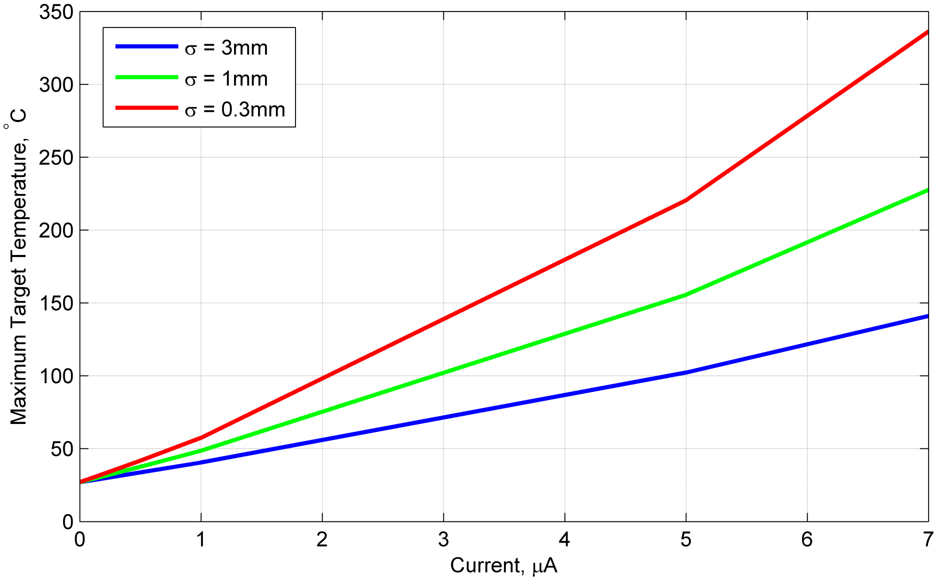

Figure 5.6: Maximum target temperatures for a 300 keV, 3 mm beam on a 0.5 mm YAG:Ce target.

The peak temperatures for the scintillation and OTR beam targets in the EMBT and EHBT are shown in Figure 5.7. The YAG:Ce screens reach their thermal quenching temperature at beam currents of 6 to 8 μA for nominally sized beams. The light output will be significanty decreased before this point, limiting the usage of the scintillation targets to up to only a few μA's for the EMBT and EHBT View Screens.

The Pyrolytic Graphite target reaches a peak temperature of 650 °C at it's highest

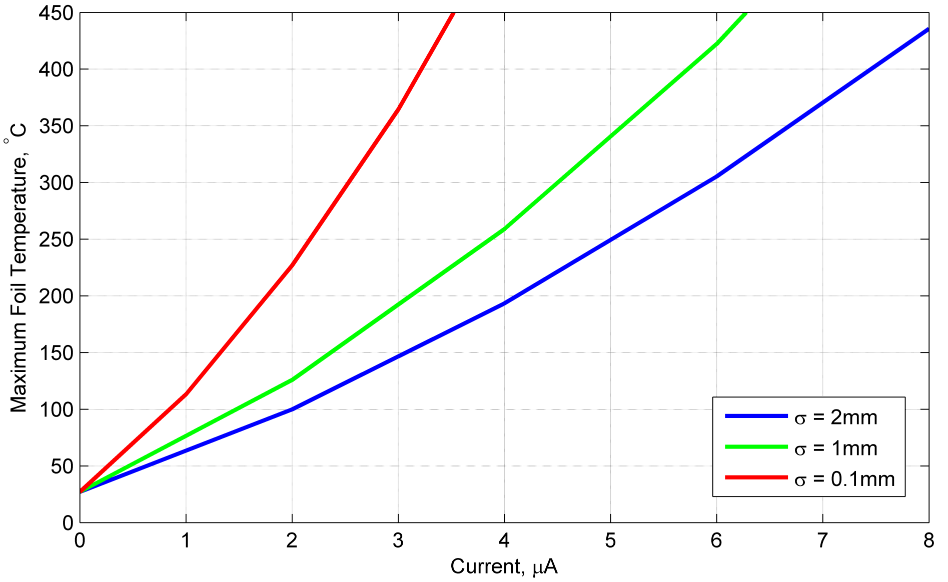

(a) 0.2 mm YAG:Ce scintillation target

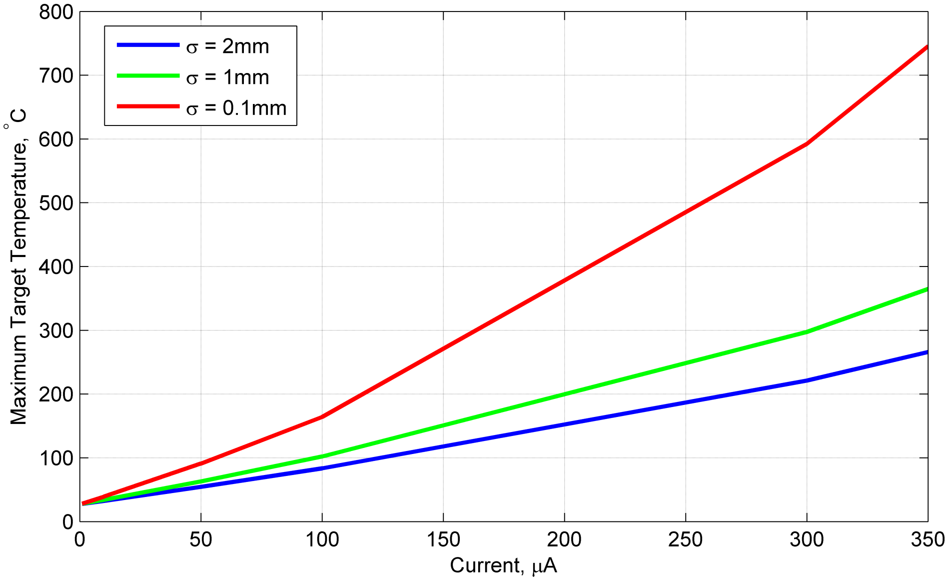

(b) 10 μm Pyrolytic Graphite OTR foil

Figure 5.7: Maximum target temperatures in EMBT and EHBT of the scintillation and OTR beam targets.

operating current of $320\,\mu$A, corresponding to 2 W of total beam losses at 10 MeV. This is well below the melting temperature for Pyrolytic Graphite and is cool enough that the emission of thermal radiation should not interfere with imaging.

Further plots of the peak operating temperatures for LYSO:Ce and Chromox scintillation screens and titanium OTR foils are included in Appendix A.2.

The ELBT View Screen may be operated with nominal beam sizes without requiring the application of a thermal correction factor. For a 3 mm beam at $6\,\mu$A of beam current, the beam would appear only $\sim 3\,\mu$m larger due to the temperature dependant loss in light output. However, since the scintillation screens in the EMBT and EHBT reach much higher temperatures, a correction factor is required in order to properly characterize the beam properties.

5.3 Simulation of the Imaging Optics

An optical simulation was designed to determine the optimal selection and configuration of the optics elements within the imaging optics system. This allowed for the evaluation of a great number of lens configurations to determine which ones would produce the clearest and brightest images of the beam profiles.

The simulation is based on a ray tracing routine, tracking individual rays of light emitted from the target, through the surfaces of the optical components, and striking a pixel on the CCD sensor. Since the routine is based on determining the path of individual rays through the optics system, the phenomenon of diffraction and interference are not modeled in this simulation.

The co-ordinate system for the model is located with the origin at the center of the beam target with the optics axis aligned with the z-axis and the incoming electron beam aligned with the x-axis, as shown in Figure 5.8. The lenses are spherical, achromatic lenses, constructed of two materials cut with spherical surfaces to focus the light. The lenses are defined within the model by a function, $z = f(x, y)$, to describe the coordinates of each of the three surfaces, and the index of refraction of both materials. The CCD sensor is defined as a planar surface, divided into individual pixel elements. The locations of the optics elements are defined using the parameters introduced earlier, d_1, the distance from target center to the front face of the first lens, d_2, the distance between the front faces of the two lenses, and d_3, the distance from the front face of the second lens to the center of the CCD sensor.

In the simulation, a series of rays are generated, emanating from the beam target,

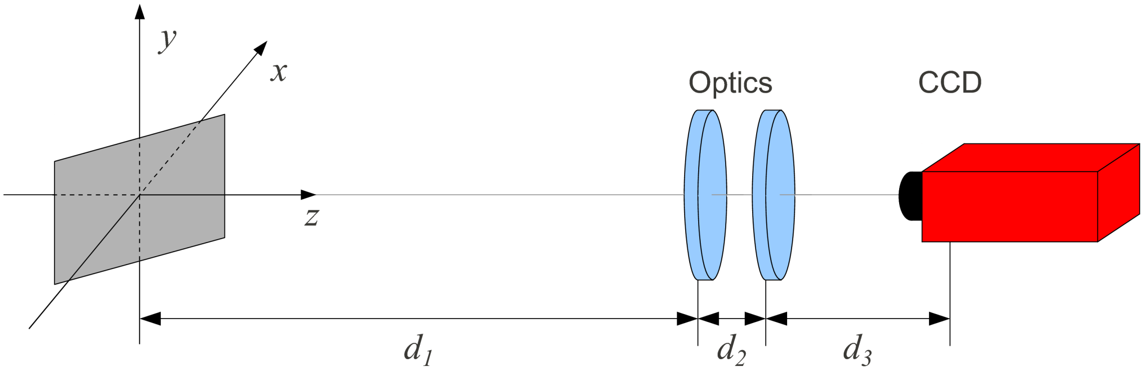

Figure 5.8: The setup of the optics ray-tracing simulation geometry.

each one with a direction specified by a random selection of polar angles within a uniform spherical emission distribution. The ray is assigned a weighting factor based on the emission direction. For scintillation light the weighting factor is equal for every ray as the light is emitted with no angular preference. For OTR light, the weighting factor is determined by the OTR emission distribution, Equations 2.2 and 2.3.

Each light ray is propagated through the optics elements by determining the coordinates of the intersection of the light ray with the surface of the next optical element, described by the functions $z = f(x, y)$. Any light rays that pass outside the aperture of the iris are terminated.

As a light ray crosses the boundary between two materials, it is refracted due to the differing indices of refraction. The change in direction is calculated through the vector form of Snell's Law. For a light ray with a normalized direction vector $\mathbf{V_1}$, crossing the surface with normal vector $\mathbf{\hat{n}_s}$, between two media with indices of refraction n_1 and n_2, the outgoing normalized direction vector would become:

$$\mathbf{V_2} = \mathbf{V_1} - (\mathbf{V_1} \cdot \mathbf{\hat{n}_s})\,\mathbf{\hat{n}_s} + \mathbf{\hat{n}_s}\sqrt{\left(\frac{n_1}{n_2}\right)^2 - 1 + (\mathbf{V_1} \cdot \mathbf{\hat{n}_s})^2} \tag{5.3}$$

When the light ray reaches the plane of the CCD sensor, the point of intersection with the CCD is determined, providing the coordinates of the corresponding pixel. The struck pixel is then incremented by the weighting factor of the ray. This process is repeated to form a simulated CCD image.

The initial positioning of the lenses and CCD was determined through calculations using the thin lens equation to achieve the correct magnification factor. Fine adjustment of the CCD sensor location was then studied using the ray tracing simulation to achieve the optimal focus, as the lenses are not ideal thin lenses. The Point Spread Function (PSF) is used to characterize the focus of the system.

The PSF is the response of the optics system to a point source of light, originating from the object plane. In an ideal imaging system, all of the light rays from a point source would be focused to the same spot on the CCD sensor, illuminating a single pixel. However, due to spherical and chromatic aberrations, non-uniformities in the lenses, and diffraction effects, the focal point of a ray has a small dependency on how far from the center of the lens the light ray passed and on the wavelength of the light. This creates a spreading of the focal point, therefore illuminating a number of CCD pixels. In general, the use of large diameter lenses with short focal lengths lead to increased spherical aberrations.

Focusing the camera in the simulation involves minimizing the width of the PSF. Another parameter used to evaluate the camera focus is the Encircled Energy, or the fraction of light that lands within a given radius on the CCD.

Results

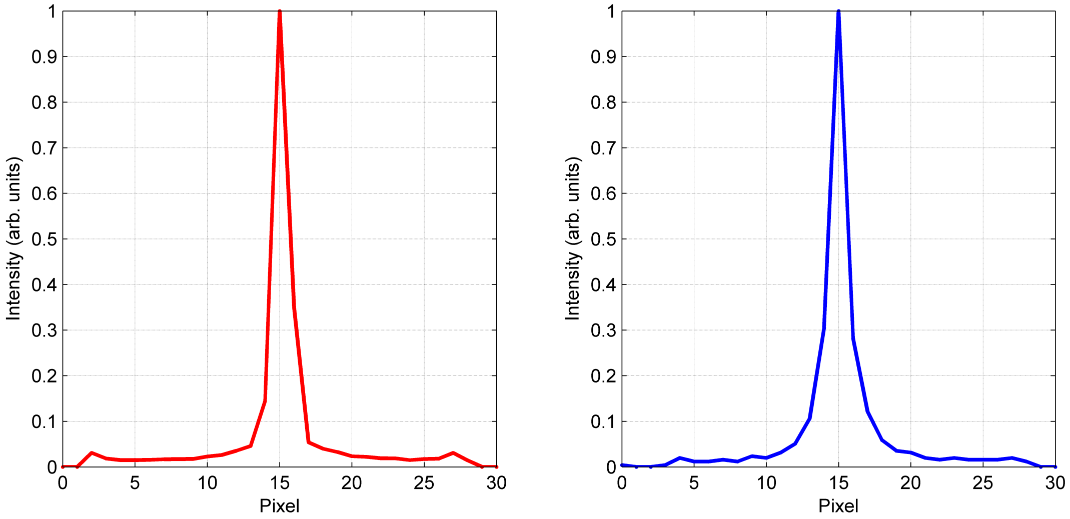

(a) PSF acquired through the optics simulation

(b) PSF acquired through the optics test bench

Figure 5.9: Cross section of the simulated and measured PSFs for the ELBT optics with a 41 mm iris aperture.

Measurement of the true PSF of the imaging optics can be used to check the validity of the ray tracing optics simulation. Figure 5.9 shows a cross section of the pixel intensity across the PSF as calculated by the optics simulation and as measured by the imaging optics in the bench tests described in the following chapter. The agreement of the measured PSF with the simulated result indicates the optics simulation provides an accurate representation of the imaging system.

5.4 Modes of Operation

The range of operation of the Beam Profile Monitor depends on a number of factors. The lower limit is set by the minimum beam current which produces an image on the camera with enough intensity to determine beam properties from. On the other end of the scale, the maximum beam current depends on one of the following: the maximum tolerable beam losses of 2 W per device, the loss of electrons scattered at large scattering angle, or the heating of the beam targets beyond operational limits.

The intensity of the light emitted by the beam targets varies with beam current, size, and energy. The size of the electron beam affects the amount of light that will illuminate a single pixel. In a larger beam, the light will be spread out over a larger number of pixels so that even though the total amount of light may be equal to that of a smaller electron beam, the individual pixels will be dimmer.

For scintillation targets, the light output is dependent on the energy deposited within the beam target by the passing electron beam. The light output is approximately proportional to beam intensity, with the light yield decreasing at higher target temperatures.

For OTR beam targets, the emission distribution depends on the beam energy. Higher energy electrons result in more light output and a larger fraction of light emitted within the angular aperture of the optics. The intensity of OTR emission scales very linearly with beam intensity.

The amount of light collected by the imaging system depends on the optics aperture, which is set by the iris diameter, and the exposure time of the camera. In the ELBT, it is most desirable to acquire images with the iris held at 15 mm and use the camera's exposure time to adjust the image intensity in order to minimize spherical aberrations. The iris may be opened to 41 mm to increase light collection at the expense of losing imaging resolution. In the EMBT and EHBT, where spherical aberrations are much less of an issue, imaging should be performed with the iris wide open as much as possible to maximize the angular acceptance when imaging OTR light.

The camera is sensitive to visible radiation within the range of approximately 300 nm to 1000 nm. The quantum efficiency of the camera's CCD sensor is shown in Figure 5.10 [35]. The emission spectrum of the scintillation light emitted by the YAG:Ce beam target is peaked at ∼ 550 nm, while the OTR light emission is broadband, emitted across the entire visible spectrum.

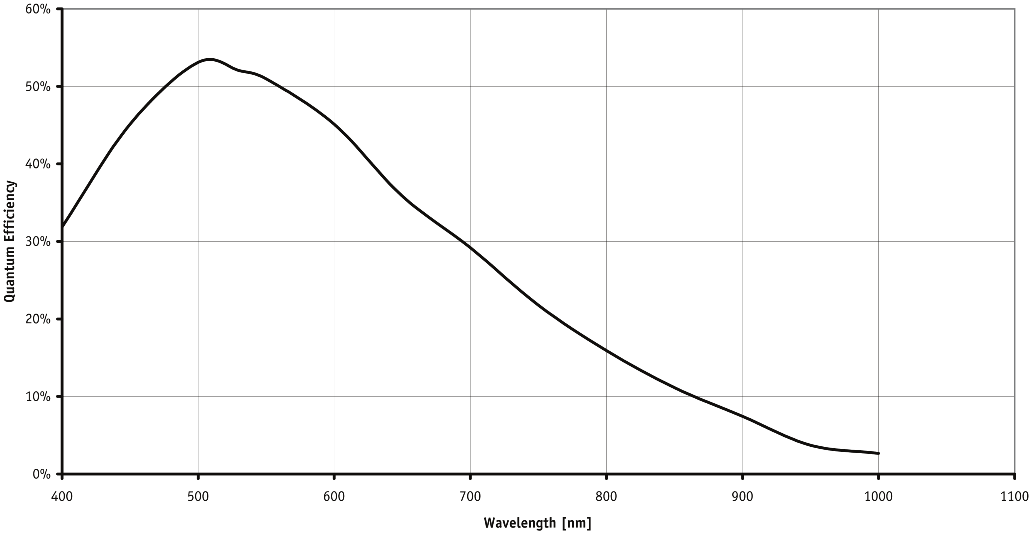

Figure 5.10: Quantum efficiency of the Manta G-046 CCD sensor.

The range of operation of the OTR and scintillation beam targets is shown in Figure 5.11. The minimum current was determined using the theoretical light output of the targets, the iris opened to its maximum diameter, and the camera exposure set to 50 ms. The maximum operating current was determined from either the current that resulted in 2 W of total losses for the OTR beam targets, or from thermal considerations for the scintillation targets. The maximum current may be limited further as a result of beam dynamics calculations determining the acceptance of scattered electrons.

At 300 keV, with a nominal beam size of $\sigma = 3\,\mathrm{mm}$, the minimum operating current is approximately 5 nA. This can be decreased to around 0.5 nA by opening the iris aperture from 15 mm to 41 mm, at the loss of imaging resolution. The upper limit for operating with the YAG:Ce screen is 6.5 μA when the beam losses reach 2 W.

For a 10 MeV beam with a nominal beam size of $\sigma = 2\,\mathrm{mm}$, either the YAG:Ce or OTR targets may be used. At low currents, from ∼1 nA up to several μA the YAG:Ce target may be used, with the target reaching temperatures exceeding 200°C

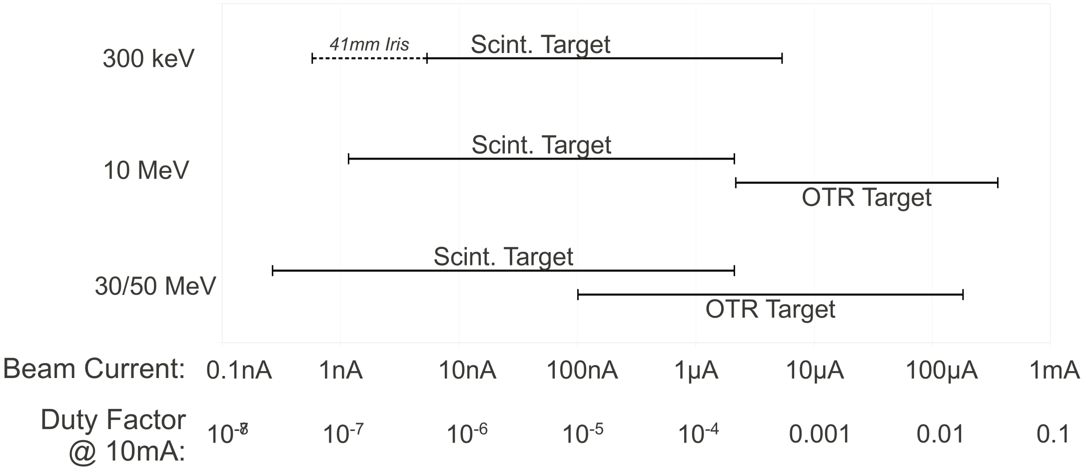

Figure 5.11: Operating ranges of OTR and YAG:Ce beam targets.

at 4 μA. The OTR light should become visible at approximately 2 μA, with the beam losses reaching 2 W at around 320 μA.

At the highest energies, 30 to 50 MeV, the nominal beam size is smaller yet, $\sigma = 1$ mm, and thus the YAG:Ce target becomes visible sooner, at a fraction of a nA and can be used up to several μA. The operable range of the Pyrolytic Graphite target overlaps the range of the YAG:Ce screen significantly and can be used from $\sim$0.1 μA up to 230 μA.

Chapter 6

Optics Bench Tests

6.1 Test Bench Setup

Tests were performed using a prototype version of the optical elements mounted on an optics test bench to characterize the performance of the imaging system and to test image acquisition procedures. The test setup is shown in Figure 6.1. During image acquisition, the overhead lights were shut off and a dark box placed over the setup to eliminate background light.

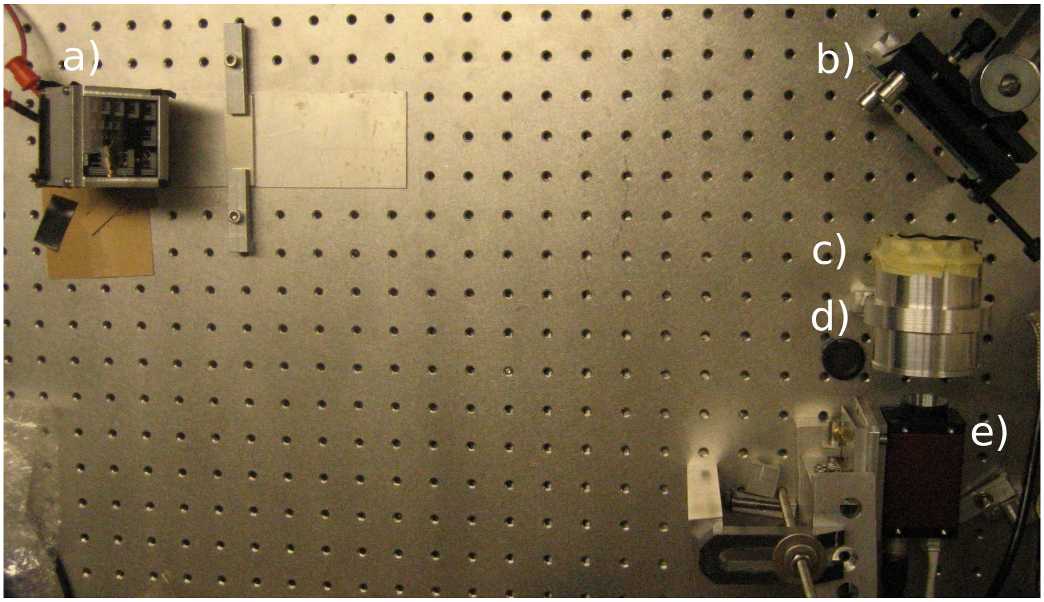

Figure 6.1: The optical bench test setup. a) optical target, b) mirror and mirror mount, c) iris, d) lenses mounted within the lens holder, and e) camera and camera mount.

Several different back-lit optical targets were used to perform the tests. A resolution test target was used to characterize the resolution of the imaging system. This target was a glass slide printed with the National Bureau of Standards 1963A Resolution Pattern in negative as shown in Figure 6.2. The pattern consists of series of dark and light line groupings, each with a different spacing between pairs of lines. The spacing is measured in line pairs per mm (lp/mm), referring to the number of light and dark pairs that fit within 1 mm. The range of line pair spacings on the target is 1 to 18 lp/mm.

A grid target pattern was used to determine the cross field of view imaging characteristics and to test the focusing algorithms. The grid consisted of a series of 0.4 mm diameter holes on a 5 mm grid pattern drilled onto a ~150 μm thick bronze sheet. To measure the PSF of the imaging system, a sheet of tin foil with a small hole poked through was used to imitate a point source of light. The size of the hole was measured under a microscope and determined to be $< 10\,\mu$m in diameter, which is much less than the size of a single pixel on the focal plane.

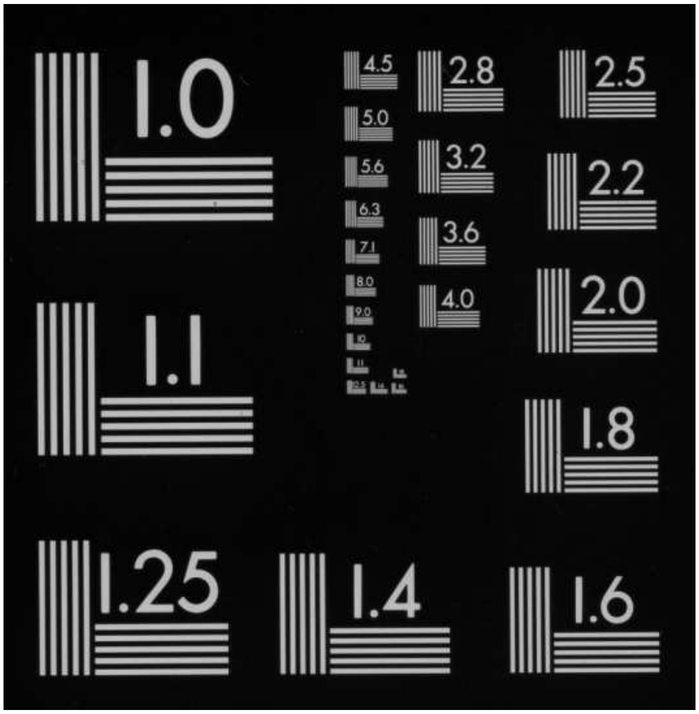

Figure 6.2: National Bureau of Standards 1963A Resolution test target used in the optical bench tests.

The targets were lit from behind with a halogen bulb placed behind a translucent diffuser. The targets were mounted either perpendicular to the optical axis, or at an angle of 45°, the same as the beam targets will be oriented. In Figure 6.1, the electron beam axis in the test setup would be oriented into the page.

The mirror was mounted on the adjustable mirror mount to provide optical alignment. The iris was held on the front face of the lens holder and was controlled manually throughout the bench tests. The camera mount allowed for angular adjustment with the rotation axis aligned with the CCD position within the camera. This allowed the camera mounting angle to be adjusted without changing the distance to the center of the CCD, which would change the focus. The camera mount had an adjustable slide to provide manual focus of the camera, similar to the camera mount that will be used in the final design.

6.2 Optics Resolution

The optics resolution can be characterized by two parameters, the Point Spread Function (PSF) and the Contrast Transfer Function (CTF). As discussed earlier, the PSF refers to the pattern on the CCD in response to a point source of light at the object plane. The CTF is a measure of the contrast between light and dark pixels as a function of the separation between them.

Point Spread Function

Optimization of the imaging optics through the use of the ray tracing optics simulation was verified by comparing of the PSF acquired on the optics bench to the results obtained through the optics simulation. As was shown in Figure 5.9, the measured PSF images show exellent agreement to the simulation results.

The PSF measured with the ELBT optics is shown in Figure 6.3 for iris diameters of 15 mm and 41 mm. The PSF is seen to have a *halo* surrounding it when the iris is opened wide to 41 mm, due to spherical aberrations. By closing the iris to 15 mm, the central portion of the PSF remain unchanged, but the halo is removed, significantly improving image quality, but decreasing the total amount of light collected. If the camera were to be focused with an ideal focus at an iris diameter of 41 mm, then the PSF would actually worsen as the iris was closed, resulting in poorer resolution images.

Figure 6.4 shows the PSF for the EMBT and EHBT imaging optics. Due to the less demanding optics, the PSF covers a significantly smaller number of pixels than for the ELBT optics, resulting in much clearer images. The PSF becomes slightly smaller as the iris is closed from 41 mm to 15 mm. This has a small effect on the resulting image quality as will be discussed in the next section, but the main effect is the reduction in the amount of light collected, which is not apparent in these images.

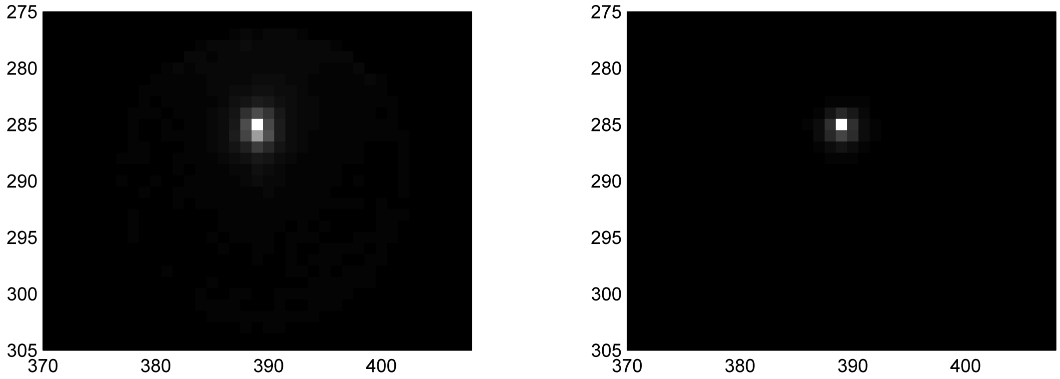

(a) 41 mm iris

(b) 15 mm iris

Figure 6.3: The PSF measured with ELBT optics.

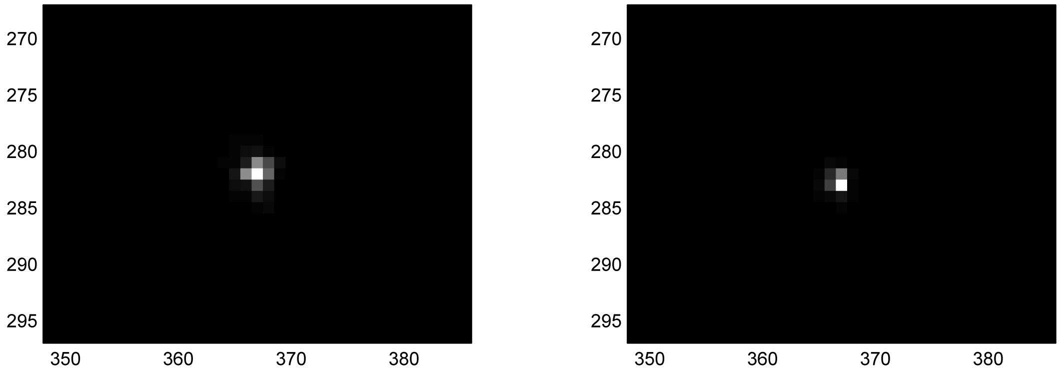

(a) 41 mm iris

(b) 15 mm iris

Figure 6.4: The PSF measured with EMBT/EHBT optics.

Contrast Transfer Function

The contrast and resolution are two very closely related qualities of an optical imaging system. Because the PSF is spread over a range of pixels, when two bright spots on an image are brought closer together, the space in between will become illuminated by the tails of the PSF, decreasing the contrast between the bright spots and the dark in between. The resolution test target is used to quantify this relationship. The CTF is the plot of the contrast as a function of line pair spacing.

In a series of alternating light and dark lines, the contrast refers to the difference in the intensity between a bright line and a dark line in the acquired image. If the intensity of an illuminated pixel within a bright line is I_{max} and of a pixel between bright lines, I_{min}, then the contrast between them is defined as

$$\text{Contrast} = \frac{I_{max} - I_{min}}{I_{max} + I_{min}} \tag{6.1}$$

The minimum separation that can be determined within a pixelated image is fixed by the size of the pixels. This minimum separation occurs when the width of a single line within a line pair is same width as a pixel. If the line pairs are smaller than this, the a single pixel would correspond to both a light and dark line and the lines would be indistinguishable. With a camera with a 580×780 pixel resolution, then the minimum distinguishable line pair spacing would be 7.5 lp/mm in the ELBT where the field of view is 50 mm wide, and 15 lp/mm in the EMBT and EHBT where the field of view is 25 mm wide.

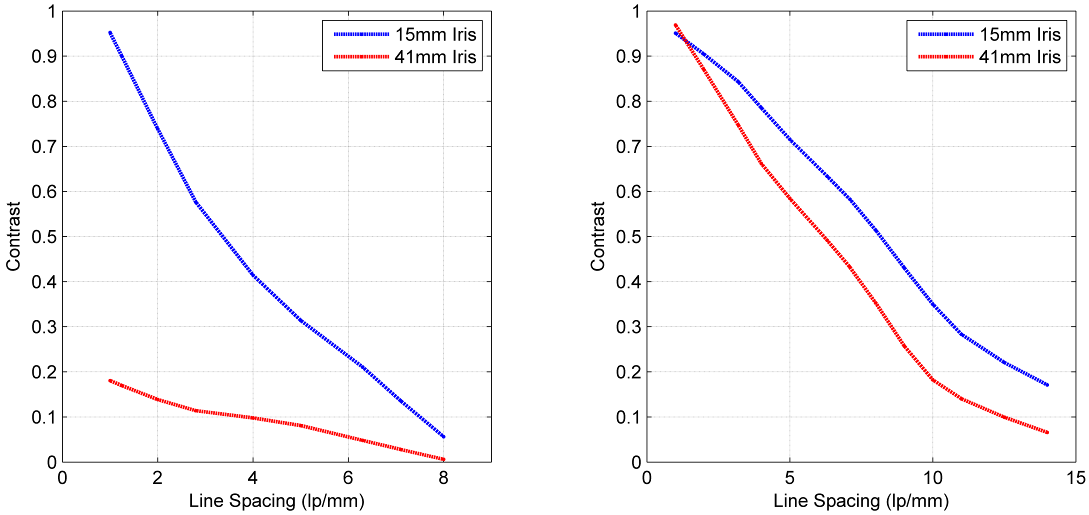

(a) ELBT optics (b) EMBT/EHBT optics

Figure 6.5: The Contrast Transfer Function measured with the resolution test target.

The CTF measured with both the ELBT and the EMBT/EHBT optics is shown in Figure 6.5, acquired with the iris diameter at 15 mm and 41 mm. The contrast improves as the iris aperture is decreased, resulting in clearer images. In the ELBT, this effect is very clear, the contrast for a 2.5 lp/mm line spacing is 65% with the iris at 15 mm, but drops by a factor of 6, to 11% with the iris opened all the up to 41 mm. With the EMBT/EHBT optics, the effect is not quite as dramatic, but at the smallest line spacing, 14 lp/mm, there is still a decrease in contrast from 18% to 8% when opening the iris from 15 mm to 41 mm.

Angled Foil Correction

The camera was mounted on a rotating camera fixture to allow verification of the camera mounting angle to provide optimal focus across the entire field of view. The ideal mounting angle was determined using the optics simulation, but was verified on the test bench. The optimal camera mounting angles are 7.0° for the ELBT camera, and 14.5° in the EMBT and EHBT.

The images acquired with the EMBT/EHBT optics and a 5 mm grid at 45° are shown in Figure 6.6. The first image shows how the edges of the beam target are out of focus on the top and bottom edges when the camera is mounted perpendicular to the optics axis, whereas the second image shows the same view with the camera rotated 14°. With the camera mounted on an angle, the points of light across the entire field of view are in focus.

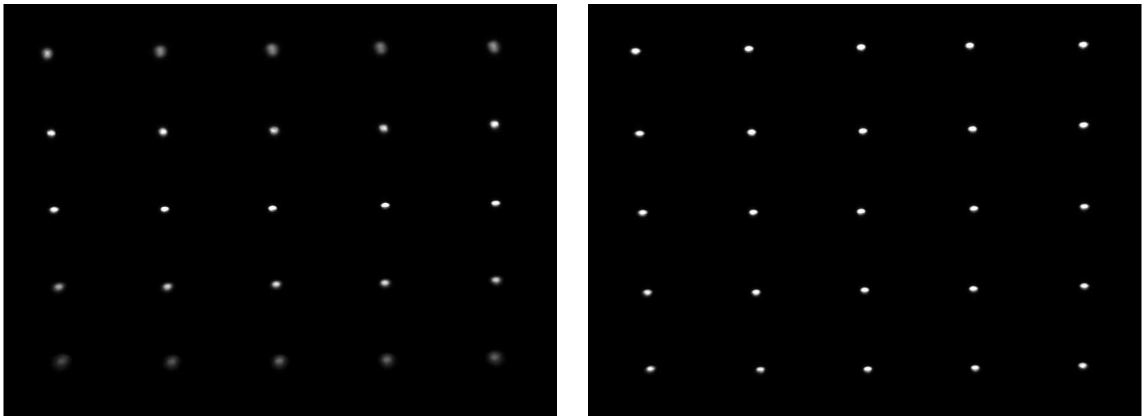

(a) Camera mounted parallel to optics (b) Camera mounted at Scheimflug angle

Figure 6.6: Images acquired on the optics test bench using the EMBT/EHBT optics showing the effect of mounting the camera at an angle to offset the beam target angle.

6.3 Chromox Scintillation Tests

Tests were performed on a Chromox disc, 30 mm in diameter and ~0.9 mm in thickness, provided by B.C.E. Special Ceramics to characterize its scintillation properties through the excitation with an ultraviolet laser. The laser was operated at a wavelength of 266 nm with a maximum energy of 30 mJ per pulse.

The Chromox was mounted at 45° to the laser beam axis, with the camera and optics located at the 90° orientation, similar to the View Screen geometry. The laser light was focused onto the surface of the Chromox by an 18 mm focal length ultraviolet lens to decrease the laser spot size. Imaging was performed with the AVT Manta G-046 camera, synchronized with the laser pulse timing. An adjustable trigger delay was used to adjust the timing of the image acquisition, down to a scale of 1 μs. The EHBT optics was used in these tests, resulting in a 25 mm field of view.

Scintillation Decay Constant

To determine the scintillation decay constant of the Chromox sample, images of the scintillation light were acquired with varying trigger delay times after the incident laser pulse. Assuming a purely exponential decay of the scintillation light with a decay constant τ, the intensity of a pixel acquired with a 20 ms exposure time and trigger delay of t_d would be

$$I = I_0 \int_{t_d}^{20\,ms} e^{-t/\tau} dt \simeq I_0' \, e^{-t_d/\tau} \tag{6.2}$$

By fitting this exponential curve to the pixel intensity of the acquired images, as shown in Figure 6.7, the decay constant of the Chromox scintillation light was determined to be 2.05 ms. As discussed in Section 2.1, this would result in the insensitivity of a Chromox beam target to time varying beam characteristics at the scale of tens of μs.

Chromox Spatial Resolution

Whereas YAG:Ce and LYSO:Ce screens are often composed of single crystals, Chromox is made up of many small grains, bound together into a screen. Typical grain sizes are on the order of 10-15 μm or larger which have the potential to limit the spatial resolution of the emitted scintillation light. Test were performed using the UV laser excitation to determine if this would limit the measurement of the properties of the beam profile.

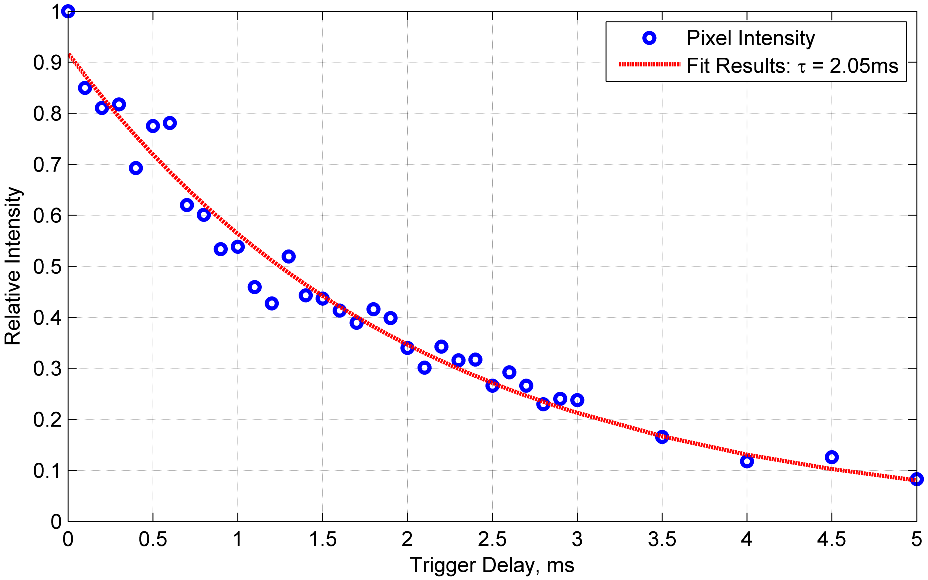

Figure 6.7: The intensity of the scintillation light emitted by the Chromox target with varying trigger delay times, fit with an exponential decay curve.

To determine the smallest laser beam spot sizes that may be imaged on the Chromox screen, the profile was imaged with the UV lens at various distances from the target to change the size of the laser spot. The laser beam profile was imaged down to beam widths of $\sigma \sim 0.1\,\mathrm{mm}$ with no indication of effects caused by the grain structure. Since the Chromox target was oriented at 45° to the beam axis, this is as small as the spot size could be decreased using the short focal length UV lens that was available.

The profile of the laser beam with a width of $\sigma_x = 0.15\,\mathrm{mm}$ and $\sigma_y = 0.26\,\mathrm{mm}$ is shown in Figure 6.8 with the field of view reduced to aproximately 13 mm by 11 mm.

The laser beam profile was imaged with the Chromox target moved to several positions across the plane of the target, over a range of ~1 mm, to determine whether the location of individual grains within the Chromox target would affect the position and width measurements of the beam profiles. In doing so, the measured location of the beam centroid and width of the beam remained stable to less than $2\,\mu\mathrm{m}$ at each screen position.

These tests indicate that beam profiles down to at least 0.1 mm in width may be imaged on a Chromox scintillation target and that the beam properties are not dependent on the location which the beam strikes the target to the levels required of the View Screen devices.

These tests have been performed using the available sample Chromox screen. Similar tests will be performed on the 0.5 mm YAG:Ce screens when they are acquired.

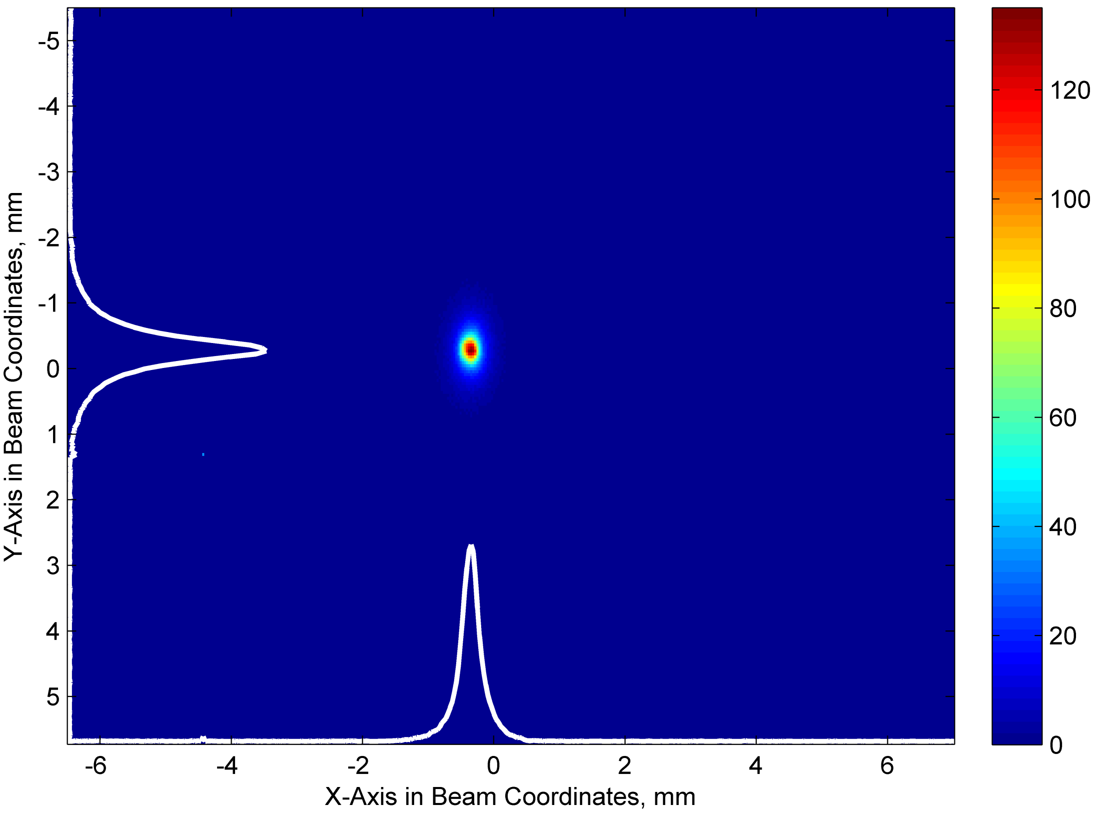

Figure 6.8: The profile of the UV laser beam on the Chromox scintillation target.

Chapter 7

Conclusions

The design of the View Screens for the TRIUMF e-linac has been presented. The design is the result of numerous simulation studies and bench tests undergone throughout the past year.

GEANT simulations have been performed to show the effects on the electron beam upon passing through a number of candidate beam target materials. The corresponding thermal response was also determined through the use of Finite Element Analysis. The result of these studies determined the selection of YAG:Ce scintillation screens, 0.5 mm thick in the ELBT and 0.2 mm think in the EMBT and EHBT areas of the beam-lines. Pyrolytic Graphite foils have been determined the optimal choice for OTR foils due to their high thermal conductivity and relatively low effect on the passing electron beam.

The optics configuration was optimized through the use of a ray tracing simulation making use of commercially available large diameter achromatic lenses. The results of these simulations have been compiled in Figure 5.11 which shows the modes of operation of the scintillation and OTR beam targets in the different areas of the e-linac for nominal beam sizes.

Optics bench tests have been performed to verify operation of the imaging optics and to test the image acquisition. The imaging resolution has been characterized through the use of the Point Spread Functions and the Contrast Transfer Functions shown in Figures 6.3 to 6.5. Verification of mounting the camera at the Scheimpflug angle showed the ability to focus the camera across the entire field of view of the beam targets.

The design provides continuous coverage over a range of beam currents, with total beam losses less than 2W/device, from nA's of beam current up to several hundred

μA's with OTR beam targets. The OTR beam targets contribute much less than 2% energy losses to the beam, whereas the 0.2 mm YAG:Ce scintillation targets will cause up to ∼2.5% energy loss for 10 MeV electrons and less than 2% for 30 and 50 MeV beams.

The imaging resolution is such that the beam structure should be visible to within ∼5% of the nominal beam size. Through the use of correction factors and calibrations discussed in Chapter 4, the requirements on beam center and width are fulfilled.

The View Screen devices have been designed to withstand both high vacuum and radiation environments. Cameras in high radiation environments are expected to last over a year before requiring replacement while cameras in low radiation areas, such as the ELBT line, are expected to last much longer than this. A back-light has been incorporated into the design to allow characterization and correction of the radiation damage of the CCD sensor.

Development of a control system for the View Screens is currently underway by another University of Victoria graduate student, Jason Abernathy. The system will involve control of the camera, iris, and light sources as well as the image processing, including the application of image calibrations and the analysis of the beam profile.

The construction of the mechanical components for the first View Screen device is underway and is on schedule for delivery by August 2011 for installation into the ELBT beam-line for initial tests. The next two devices will be required shortly after, incorporating modifications as required.

Bibliography

[1] M. McLean and T. Meyer, eds., *Five-Year Plan 2010–2015: Building a Vision for the Future.* TRIUMF, 2008.

[2] "TESLA Technical Design Report," 2001.

[3] B. Barish, "The global design effort for an international linear collider," in *Proceedings of EPAC06, Edinburgh, Scotland*, 2006.

[4] R. Garoby and F. Gerigk, "Status of the SPL at CERN," tech. rep., 2007.

[5] W. T. Diamond, "A radioactive ion beam facility using photofission," *Nuclear Instruments and Methods in Physics Research A*, vol. 432, pp. 471–482, 1999.

[6] S. Koscielniak *et al.*, "Electron linac photo-fission driver for rare isotope program at TRIUMF," in *Proceedings of PAC11, New York City, New York*, 2011.

[7] S. Koscielniak *et al.*, "Accelerator design for a 1/2 MW electron linac for rare isotope beam production," in *Proceedings of EPAC08, Genoa, Italy*, pp. 2728–2730, 2008.

[8] S. Koscielniak *et al.*, "An electron linac photo-fission driver for the rare isotope program at TRIUMF," in *Proceedings of SRF2009, Berlin, Germany*, pp. 907–912, 2009.

[9] V. Naik *et al.*, "VECC/TRIUMF injector for the e-linac project," in *Proceedings of LINAC2010, Tsukuba, Japan*, pp. 727–729, 2010.

[10] A. W. Chao and M. Tigner, eds., *Handbook of Accelerator Physics and Engineering.* World Scientific, 1998.

[11] P. W. Allison, J. D. Sherman, and D. B. Holtkamp, "An emittance scanner for intense low-energy ion beams," *IEEE Transactions on Nuclear Science*, vol. NS-30, no. 4, pp. 2204–2206, 1983.

[12] J. Seeman, "Determination of ϵ, β, and α from an arbitrary number of beam size measurements," Tech. Rep. CN-376, SLAC, 1990.

[13] S. Koscielniak *et al.*, "E-linac beam diagnostics requirements," Tech. Rep. Version 5, TRIUMF, 2010.

[14] S. Koscielniak, "University of Victoria Weekly Group Meeting," October 2010.

[15] A. Lumpkin, "Comparisons and applications of scintillator and OTR screens for bright electron beams," in *Workshop on Scintillating Screen Applications in Beam Diagnostics, GSI, Darmstadt, Germany*, 2011.

[16] K. J. McCarthy *et al.*, "Response of chromium-doped alumina screens to soft x rays using synchrotron radiation," *Journal of Applied Physics*, vol. 94, no. 2, pp. 958–962, 2003.

[17] R. Jung, G. Ferioli, and S. Hutchins, "Single pass optical profile monitoring," in *Proceedings of DIPAC 2003, Mainz, Germany*, pp. 10–14, 2003.

[18] Saint Gobain Crystals, "YAG(Ce) Yttrium Aluminum Garnet Scintillation Material Datasheet," tech. rep., 2008.

[19] A. Murokh *et al.*, "Limitations on the resolution of YAG:Ce beam profile monitor for high brightness electron beam," in *Proceedings of the 2nd ICFA Advanced Accelerator Workshop*, 1999.

[20] A. Lumpkin *et al.*, "Spatial resolution limits of YAG:Ce powder beam-profile monitors at the Fermilab A0 Photoinjector," in *Proceedings of FEL2009, Liverpool, UK*, pp. 348–351, 2009.

[21] G. Kube, C. Behrens, and W. Lauth, "Resolution studies of inorganic scintillation screens for high energy and high brilliance electron beams," in *Proceedings of IPAC10, Kyoto, Japan*, pp. 906–908, 2010.

[22] R. Mao, L. Zhang, and R.-Y. Zhu, "Optical and scintillation properties of inorganic scintillators in high energy physics," *IEEE Transactions on Nuclear Science*, vol. 55, no. 4, pp. 2425–2431, 2008.

[23] H. Feng *et al.*, "Temperature dependence of luminescence characteristics of LYSO:Ce^{3+} scintillator grown by the Czochralski method," *Journal of Applied Physics*, vol. 108, p. 033519, 2010.

[24] V. Bachmann, C. Ronda, and A. Meijerink, "Temperature quenching of yellow Ce^{3+} luminescence in YAG:Ce," *Chemistry of Materials*, vol. 21, pp. 2077–2084, 2009.

[25] V. Ginsberg and I. Frank, "Radiation arising from a uniformly moving electron as the electron crosses the boundary between two media," *Journal of Experimental and Theoretical Physics*, vol. 16, pp. 15–30, 1946.

[26] P. Goldsmith and J. V. Jelley, "Optical transition radiation from protons entering metal surfaces," *Philosophical Magazine*, vol. 4, no. 43, pp. 836–844, 1959.

[27] L. Wartski *et al.*, "Interference phenomenon in optical transition radiation and its application to particle beam diagnostics and multiplescattering measurements," *Journal of Applied Physics*, vol. 46, no. 8, pp. 3644–3653.

[28] J. Jackson, *Classical Electrodynamics.* Wiley - India, 3rd ed., 1999.

[29] M. Ter-Mikaelian, *High-Energy Electromagnetic Processes in Condensed Media*, vol. 29 of *Interscience Tracts on Physics and Astronomy.* Wiley - Interscience, 1972.

[30] R. Ritchie and H. B. Eldridge, "Optical emission from irradiated foils I," *Physical Review*, vol. 126, no. 6, pp. 1935–1947, 1962.

[31] D. Giove, C. D. Martinis, M. Pullia, and P. Mangili, "Low energy regime for optical transition radiation emission," in *Proceedings of PAC95, Dallas, Texas*, 1995.

[32] W. M. Haynes and D. R. Lide, eds., *CRC Handbook of Chemistry & Physics Online, 91st Edition.* CRC Press, 2011.

[33] Minteq Pyrogenics Group, "PYROID Long Lived Pyrolytic Graphite Stripper Foils," 2011.

[34] A. D. Rakic *et al.*, "Optical properties of metallic films for vertical-cavity optoelectronic devices," *Applied Optics*, vol. 37, no. 22, pp. 5271–5283, 1998.

[35] "AVT Manta Technical Manual," Tech. Rep. V4.0.1, Allied Vision Technologies, 2010.

[36] "AVT Manta G-046B EMVA 1288 data," tech. rep., Allied Vision Technologies, 2010.

[37] S. Hutchins, M. Facchini, and E. Tsoulou, "Radiation tests on solid state cameras for instrumentation," in *Proceedings of DIPAC 2005, Lyon, France*, p. 315, 2005.

[38] R. Jung, "Image sensor technology for beam instrumentation," in *Proceedings of BIW98, Stanford, California*, 1998.

[39] E. L. Hall, *Computer Image Processing and Recognition.* Academic Press, 1979.

[40] A. Lumpkin, V. E. Scarpine, and G. R. Tassotto, "Initial far-field OTR images generated by 120-GeV protons at FNAL," in *Proceedings of PAC07, Albuquerque, New Mexico*, pp. 4378–4380, 2007.

[41] L. D. Landau, "On the energy loss of fast particles by ionization," *Journal of Physics (USSR)*, vol. 8, p. 201, 1944.

[42] H. Cong *et al.*, "Structural and thermal properties of the monoclinic Lu2SiO5 single crystal," *Journal of Applied Crystallography*, vol. 42, pp. 284–294, 2009.

Appendix A

Additional Information

Simulations were performed using a number of candidate beam target materials to characterize their thermal and energy loss performance. For scintillation targets, YAG:Ce, LYSO:Ce, and Chromox beam targets where investigated and for OTR targets, simulations where performed on Pyrolytic Graphite and Titanium targets.

The selection of YAG:Ce scintillation targets and Pyrolytic Graphite OTR foils was dependent on maximizing the operating regime of the View Screen under varying conditions. The results of the GEANT and thermal simulations of the remaining candidate beam target materials are provided in the following pages.

A.1 GEANT Simulations of Additional Candidate Materials

Since the electron energy is quite low in the ELBT, nearly all of the 300 keV beam electrons are stopped within the first 100-200 μm of the ELBT scintillation targets. For LYSO:Ce targets, an average of 191 keV of energy is deposited within the target per beam electron. The remaining energy is carried away by scattered electrons and bremsstrahlung photons. For Chromox targets, the average energy deposited is 262 keV per beam electron.

The total energy loss and scattering distributions for the 200 μm LYSO:Ce and 500 μm Chromox scintillation screens and 5 μm Titanium OTR foils for the EMBT and EHBT View Screens are shown in Figures A.1 and A.2.

Because of it's higher density, the LYSO:Ce beam targets cause higher energy losses and beam scattering than YAG:Ce targets of similar thickness. Similarly, the

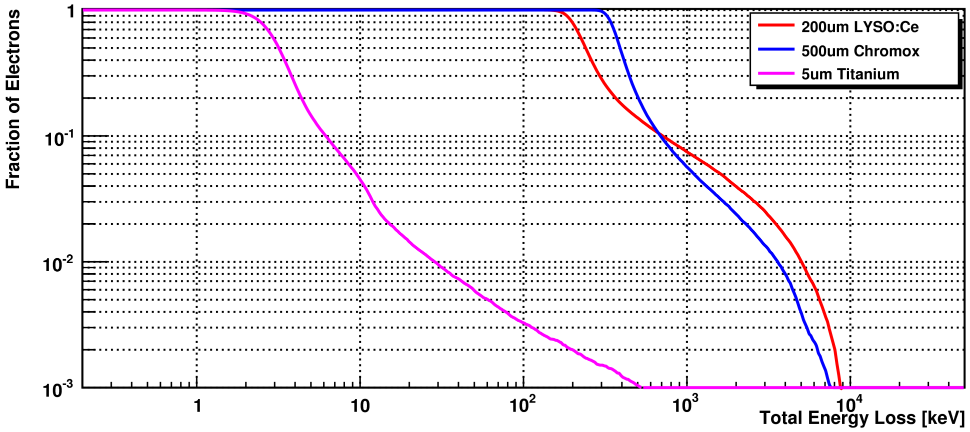

(a) 10 MeV electron beam energy

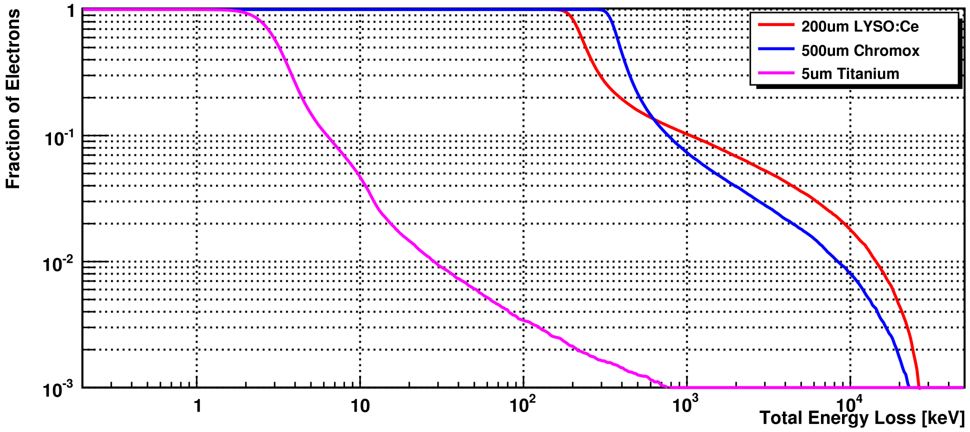

(b) 30 MeV electron beam energy

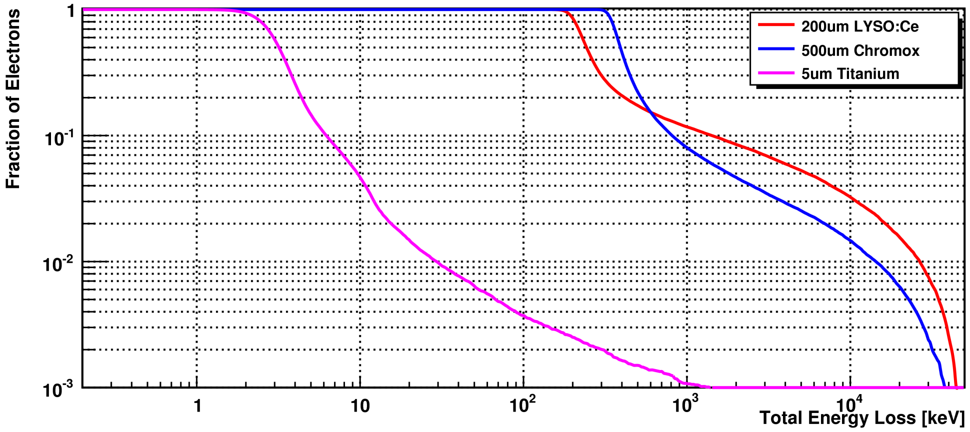

(c) 50 MeV electron beam energy

Figure A.1: The fraction of electrons with average total energy loss per electron greater than a given energy for 200 μm LYSO:Ce and 500 μm Chromox scintillation screens and 5 μm Titanium OTR foils.

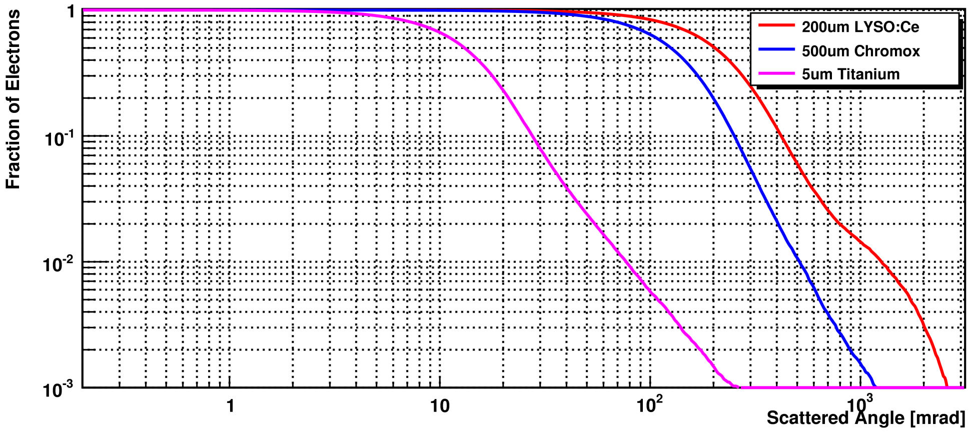

(a) 10 MeV electron beam energy

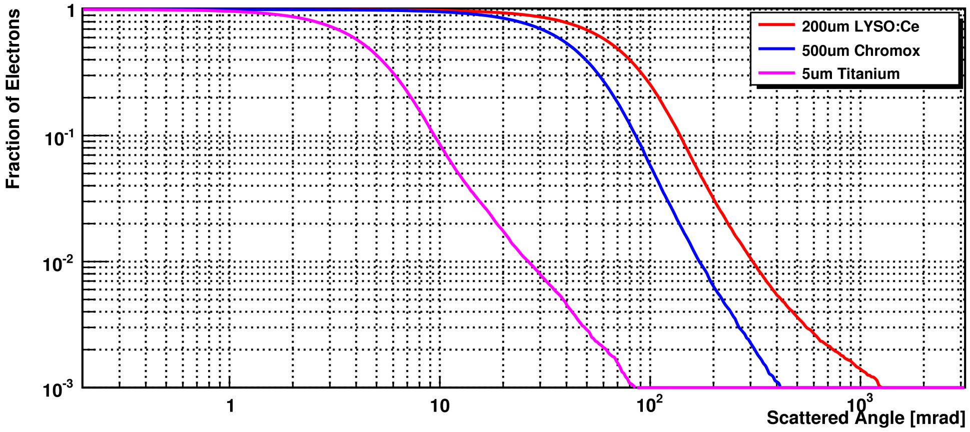

(b) 30 MeV electron beam energy

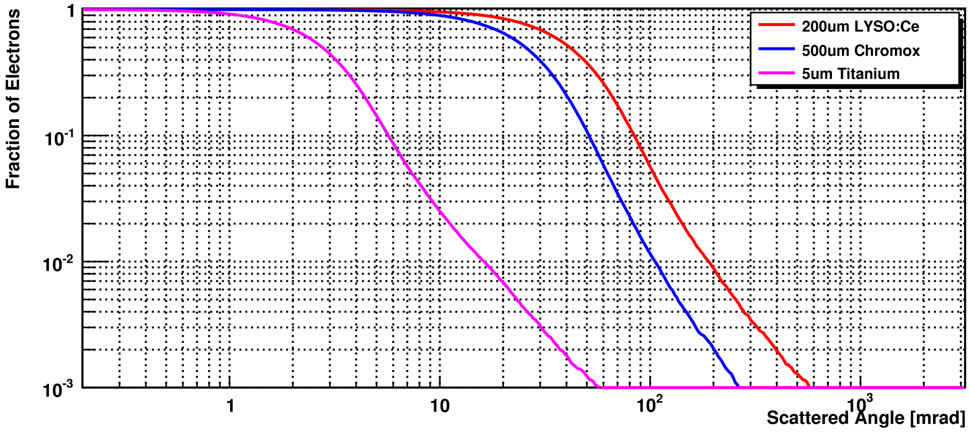

(c) 50 MeV electron beam energy

Figure A.2: The fraction of electrons scattered outside a given scattering angle for 200 μm LYSO:Ce and 500 μm Chromox scintillation screens and 5 μm Titanium OTR foils.

thicker Chromox beam targets contribute to higher amounts of energy loss and beam scattering. For OTR targets, the thickness of a Titanium foil must be approximately half that of a Pyrolytic Graphite foil to achieve similar intercepting characteristics due to its high atomic number.

A.2 Thermal Simulations of Additional Candidate Materials

To keep the peak temperatures of the ELBT scintillation beam targets low, 0.5 mm YAG:Ce screens will be used. The extra thickness adds more material to reduce the peak target temperatures, and since the energy deposition occurs in the first 100 μm or so, resolution should not be degraded by the emission of scintillation light throughout the thickness. However, if beam tests indicate the need to reduce the thickness of the ELBT beam targets, then the 0.5 mm YAG:Ce screens may be replaced by 0.2 mm screens. Figure A.3 shows the thermal response for the thinner scintillation screens. The temperatures increase much quicker than in the 0.5 mm screen, reaching temperatures in excess of 100°C for currents over 2 μA.

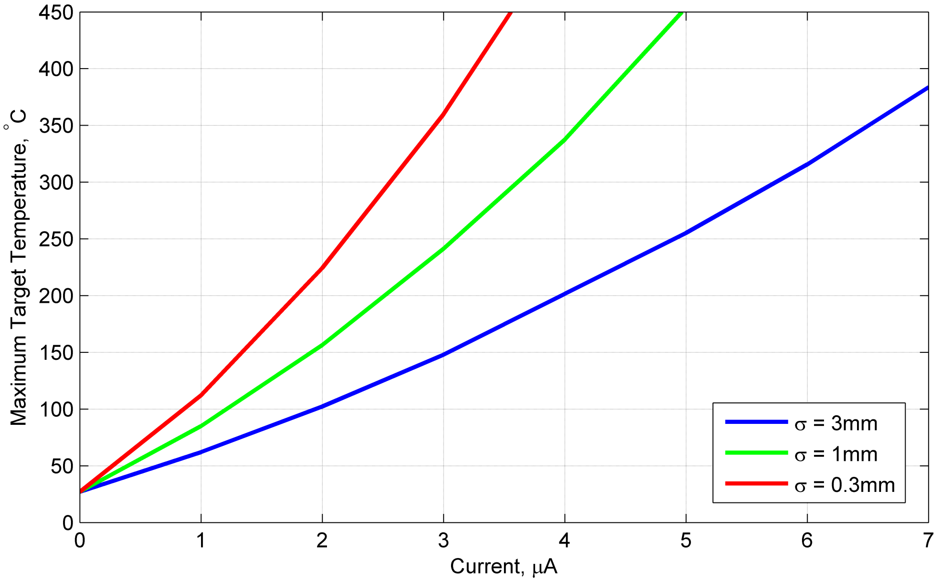

Figure A.3: Maximum target temperatures in ELBT of a 200 μm YAG:Ce scintillation beam target.

Thermal simulations of the ELBT LYSO:Ce and Chromox scintillation screens are shown in Figure A.4. LYSO:Ce, with it's very low thermal conductivity, reaches very high temperatures at relatively low beam currents making it an unsuitable beam target for View Screens operating over several μAs. Chromox however has the highest thermal conductivity of the three scintillation screens studied, 10 times higher than LYSO:Ce and double that of YAG:Ce. This results in very reasonable beam target temperatures for Chromox screens; less than ~100°C for up to almost 7 μA beam current for even the smallest beam sizes.

The LYSO:Ce and Chromox targets have similar thermal responses in the EMBT and EHBT as in the ELBT View Screens, Figure A.5. LYSO:Ce reaches thermal quenching temperatures after only 1 to 2 μA and Chromox temperatures stay below ~200°C up to around 7 μA. Under thermal considerations, Chromox is an excellent candidate for scintillation screens due to it low operating temperatures. However, because of it's long scintillation decay time and resolution qualities discussed in Section 2.1, YAG:Ce is the better choice overall.

A Titanium OTR foil would reach its melting temperature of 1670°C at around 80 to 100 μA of beam current for nominal beam sizes, Figure A.6. A pulsed beam would reach higher temperatures than shown here immediately after a beam bunch passes, limiting the beam current even further. Therefore, the OTR beam targets will be constructed from Pyrolytic Graphite as they may be safely operated up to beam currents greater than 300 μA without reaching damaging temperatures.

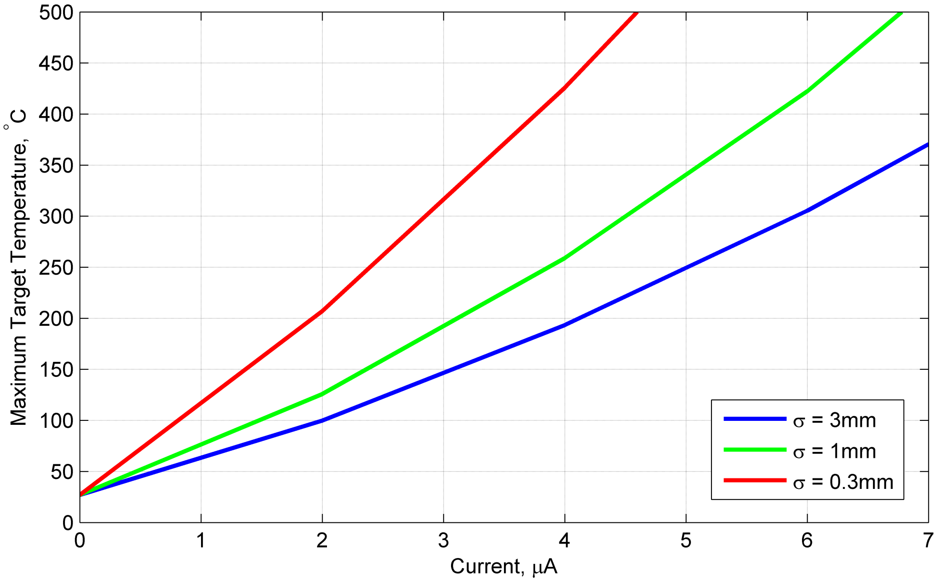

(a) 0.5 mm LYSO:Ce scintillation target

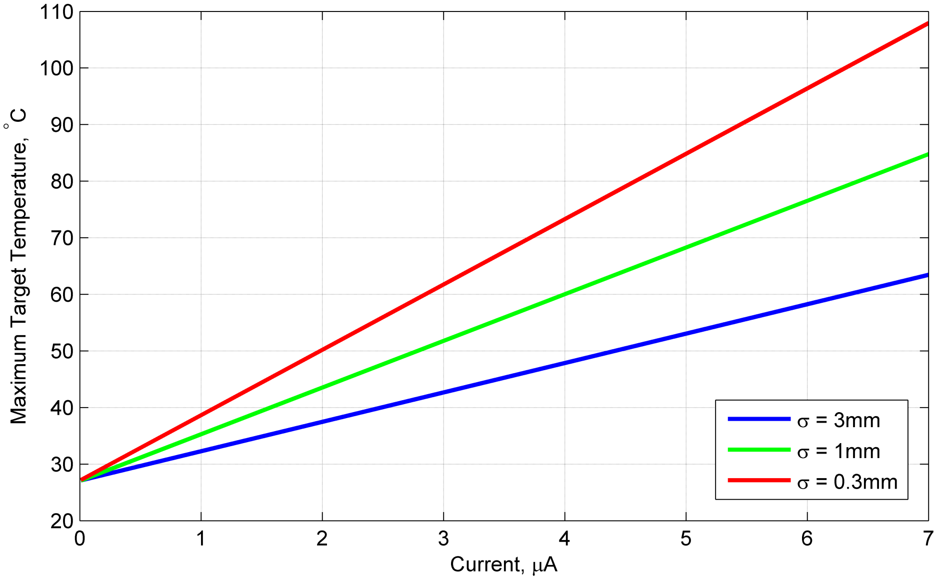

(b) 0.5 mm Chromox scintillation target

Figure A.4: Maximum target temperatures in ELBT of the scintillation beam targets.

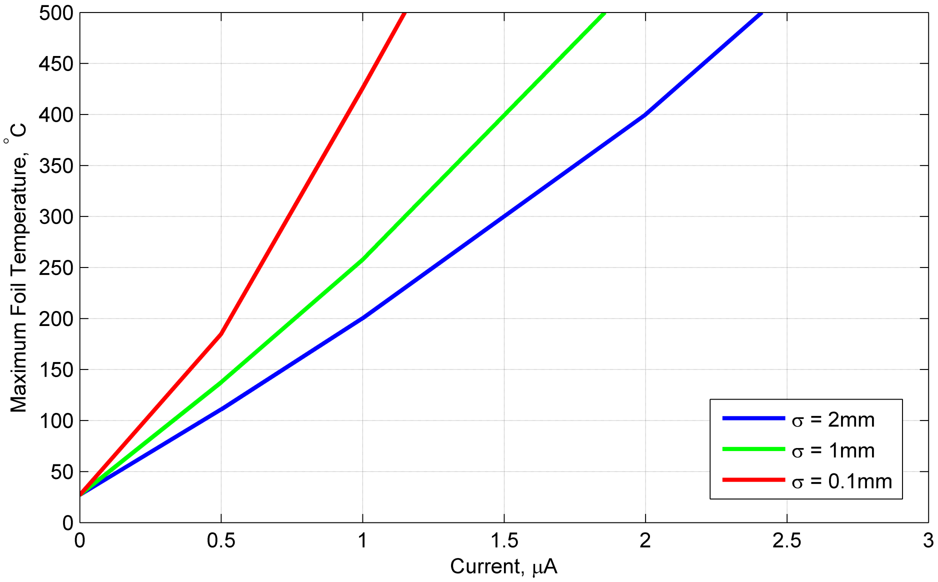

(a) 0.2 mm LYSO:Ce scintillation target

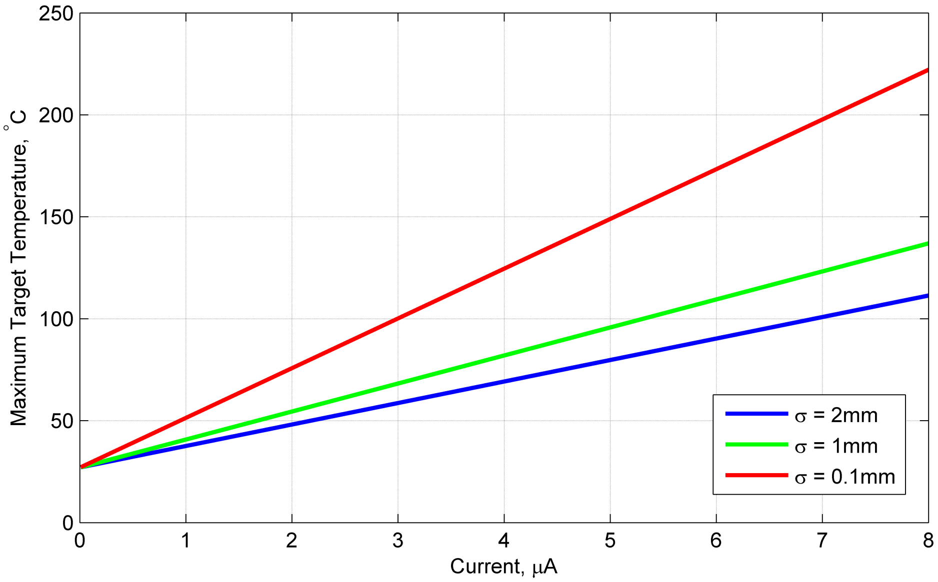

(b) 0.5 mm Chromox scintillation target

Figure A.5: Maximum target temperatures in EMBT and EHBT of the scintillation beam targets.

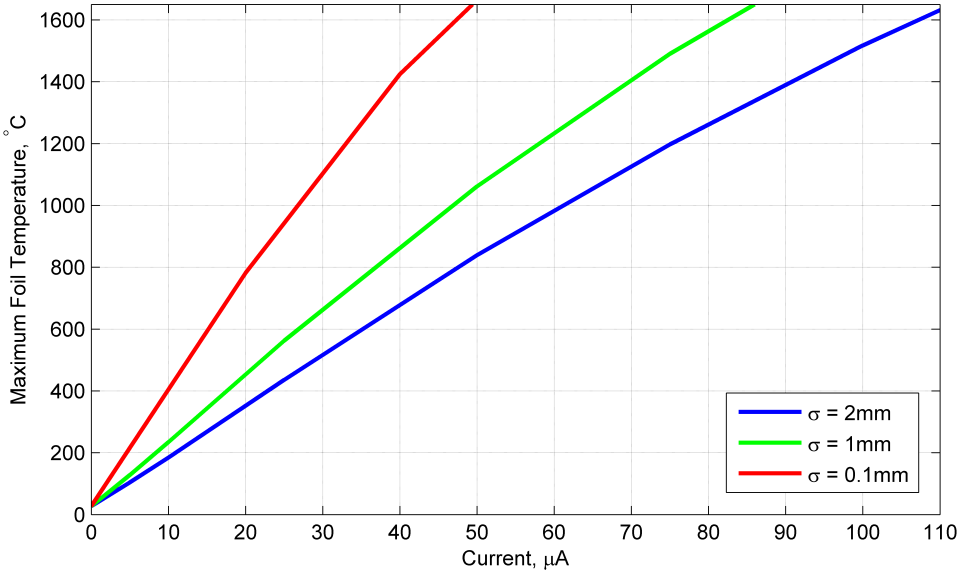

Figure A.6: Maximum target temperatures in EMBT and EHBT of the 5 μm Titanium OTR beam targets.